Convergence
A Journal for Young Researchers

ORIGINAL RESEARCH

Received: 8-28-25; Accepted: 2-4-26;
Managing Editor: Jonas Katona;
Action Editor: Jonas Katona

Exoplanetary Ring Systems: Identification and Parameter Estimation from Transit Photometry Data

Daniil E. Veliev

Letovo School, Moscow, Russia

Abstract

Imagine detecting exoplanetary Saturn-like rings, invisible to telescopes, and discovering their properties indirectly by observing transits over time. With the abundance of observational data in various catalogs, we can access high-precision transit light curves to analyze exoplanetary rings, which is valuable for getting a better understanding of the principles of ring formation, stability and dynamics. This paper focuses on modeling the light curves of transits by exoplanets with rings to identify the presence of ring systems around them, their physical properties and configurations. We hypothesize that it is possible to extract geometrical and positional ring properties from a light curve by fitting modeled light curves to observations. For modeling, a masking algorithm is used, which involves creating pixel-based representations of the covered star, the transiting exoplanet and its translucent elliptical ring and moving the mask of the ringed exoplanet along the pixel grid of the star. We test our hypothesis by running sample simulations of an exoplanet and its rings, and we use the model to detect a ring system around a planet, the inferred radius of which is too big for its inferred mass, HIP 41378f (a "super-puff" candidate), that has been viewed as a potentially ring-bearing exoplanet. The results support our hypothesis, demonstrating that the presence of rings around an exoplanet and their properties can strongly contribute to the resulting light curve. Furthermore, the results of data-fitting point to the direction of the presence of HIP 41378f's ring system; we also attempt to estimate its parameters.

Keywords: exoplanets, transit light curves, planetary systems, rings, transit photometry, ring system detection, Markov Chain Monte Carlo (MCMC) parameter estimation

1. Introduction

Transit photometry is an increasingly popular method of detecting and studying **exoplanets** (planets outside the Solar System). When an exoplanet passes in front of its **host star**, it blocks the light from it, producing a dip in brightness over time. This dip is called a **transit light curve** (see Figure 1).

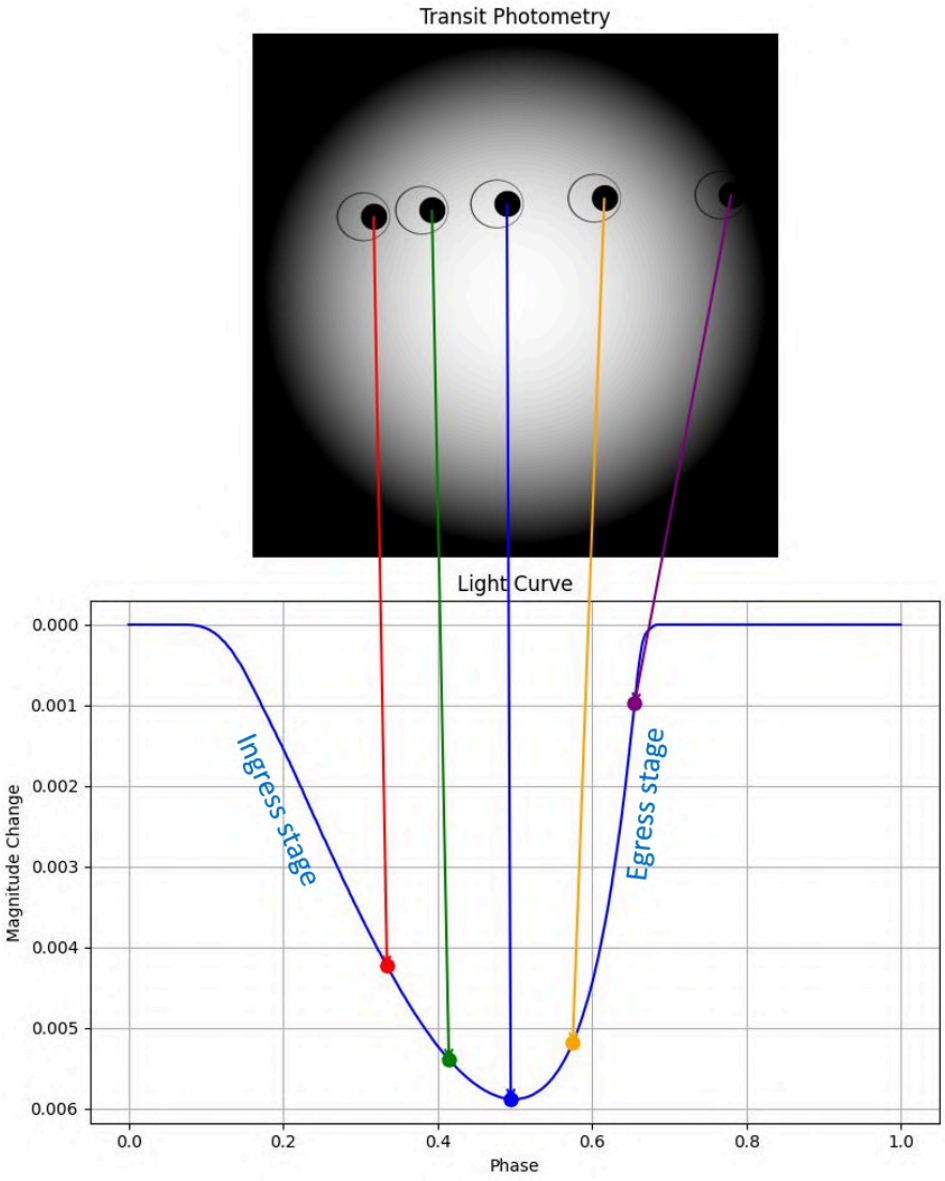

Figure 1: The figure demonstrates how the transit photometry method works for ringed exoplanets. Five positions of an exoplanet are marked throughout its trajectory in front of the host star. For each marked position, a colored line links to a respective point in the transit light curve below. For each of these points, the dip in brightness is caused by the blocking of the star's light by the exoplanet in the selected position. The ingress (entering the transit) and egress (finishing the transit) stages are labeled in the graph. The magnitude change in the graph represents the logarithmic change in the star's brightness, and the phases represent normalized time values. The figure illustrates that the spatial configuration of the

ringed exoplanet has a direct impact on specific features in the photometric light curve, which is more complex and yields different results compared to a simple spherical planet transit.

The discovery of **exoplanetary rings** using transit photometry has long been an intriguing challenge in astrophysics. Even though the ring systems in our Solar System have been thoroughly studied, it is highly challenging to detect exoplanetary ring systems due to their marginal angular sizes and small photometric signatures. This makes **direct imaging** (capturing directly resolved images) difficult. Nevertheless, transit photometry is a powerful and promising technique for identifying such ring systems indirectly. Recent studies (Heising et al., 2015; Lu et al., 2025; Piro & Vissapragada, 2020) are focused on detecting rings through mathematical modeling or peculiar light curve features (e.g., asymmetrical transit dips). Despite these efforts, no exoplanetary rings have been confirmed with high certainty after J1407b (Kenworthy & Mamajek, 2015), only hypothesized, due to limitations of observational noise and uncertainty about false positives (Aizawa (逢澤正嵩) et al., 2017; Barnes & Fortney, 2004).

Previous studies (Ohta et al., 2009; Piro & Vissapragada, 2020) suggest that rings may explain detected anomalous planetary properties, such as the inflated radii of **super-puffs** (exoplanets with extremely low inferred densities or low masses for their inferred radii). HIP 41378f (Santerne et al., 2019), the ring system of which we investigate in this paper, is an example of this type of planet. Also, detecting rings could help in identifying **shepherd moons** (moons that gravitationally influence the ring particles and maintain the ring's structure), the study of which is highly valuable for understanding moon formation (Tiscareno, 2013). However, current models of ringed exoplanets often do not include some kinds of factors, such as ring **transparency** or **eccentricity** (how elongated a ring is), which leads to potential false negatives. So, improving these models could lead to discoveries of exoplanetary ring systems in archival data from missions like Kepler and TESS (Transiting Exoplanet Survey Satellite).

Our study investigates whether high-precision transit photometry, combined with an advanced parameter-rich pixel-based masking algorithm, can reliably identify and characterize exoplanetary ring systems by modeling their light curve signatures. We propose that by creating a pixelated transit model that accounts for ring transparency, eccentricity, ring and exoplanet orbit orientation and **limb-darkening** (darkening of the host star to its edges) effects, it is possible to accurately recover ring parameters from high-precision light curves. Our approach is different from analytical models (Heising et al., 2015) by using a numerical, pixel-based masking framework. We describe our model as 'pixel-based' because it represents the host star, exoplanet and ring as **discrete 2D pixel grids** (images), where each individual cell (pixel) corresponds to a localized intensity or opacity value.

Unlike analytical methods that rely on geometric equations to calculate the covered area of the stellar disk, which often necessitate simplifying assumptions like circular rings or uniform stellar brightness, our pixel-based approach performs a **direct numerical integration** (summation of pixel-by-pixel operations). By moving the planetary and ring 'masks' across the stellar pixel grid and applying a pixel-by-pixel opacity transformation, we can precisely model highly complex configurations. This includes features such as eccentric, inclined and rotated rings, and oblate planetary shapes that are mathematically difficult to describe with traditional analytical geometry. This numerical flexibility enables a more **parameter-rich** analysis, allowing us to account for more subtle ring properties and orientation angles that are frequently neglected in existing literature.

In Section 2 (Methods), we describe our pixel-based masking algorithm with emphasis on how the star matrix, exoplanet and ring masks are modeled, how the ring position is calculated, how the orbital parameters of the exoplanet affect the light curve and how limb-darkening is incorporated. In Section 3 (Parameter Estimation), we describe how the best-fit ring properties should be estimated based on the light curve (density, semi-major axis, width, eccentricity, obliquity, azimuthal angle and argument of periapsis), using the super-puff candidate HIP 41378f as an example. In Section 4 (Validation), we test our model by generating **synthetic light curves** (artificial light curves generated by the model to represent various sets of parameter values) to assess the impact of input parameters on them and analyze the observed light curve of HIP 41378f, attempting to detect its ring system. In Section 5 (Conclusions), we summarize our results and talk about future prospects of implementing our tool. This work aims to contribute to the growing field of exoplanetary ring studies by helping develop a new model for comparative analysis of archival and future observational data.

2. Methods

The transit light curve is modeled using the innovative pixelized modeling algorithm. First, all the required properties of the planet, its rings, orbit and host star are calculated from input parameters and converted to be used by the functions (e.g., for matrix representations, all length units should be in pixels) for computing the grid representations of these objects. The representation of a star divides it into small pixels and calculates their **normalized intensities** (quotients of any pixel's brightness to the one of the brightest pixel), taking the limb-darkening coefficients from theoretical tables (either Díaz-Cordovés & Giménez, 1992, or Claret & Giménez, 1992, depending on the physical properties of the star and limb-darkening coefficients availability). The representations of a planet and its rings also separate objects into pixels, creating a **masking matrix**. However, they yield the **optical depth** (an exponential measurement of an object's transparency) of every pixel based on intrinsic calculations.

The algorithm also involves applying some ring properties that were disregarded by some of the previous models (specifically, ring eccentricity, optical depth and argument of periapsis). Running the simulation confirmed that some of them can be neglected, but suggested that previous models (Aizawa et al., 2023; Barnes & Fortney, 2004; Ohta et al., 2009) undermine the importance of some of them (for these findings, see Section 4.1).

2.1. Main model parameters

Model parameters are the values that are required to run the model or are computed during its runtime. They can be classified as input, intrinsic, output, fixed, floating and calculated. **Input parameters** are passed to the model by the user. **Fixed input parameters** are kept constant when working with the same observational data. They are passed to the model but are not estimated during the data fitting process (Sections 3, 4.2 and 4.3). Instead, they are unchanged in the data-fitting stage. Finally, **floating input parameters** are the values that can vary within a range set by the user. Also, the floating parameters are those parameters, the values of which are estimated during the data-fitting (Sections 3, 4.2 and 4.3). Therefore, the floating parameters carry the most crucial information about the model. The boundaries of these parameters and their justifications may be viewed in Table 3 (the main model), Table 6 (ringless model), Table 7 (oblate planet model), Table 9 (observational noise) and Table 10 (starspots/faculae model).

2.2. Floating parameters and their limits

Floating parameters are the values that are used for building the model, the values of which are previously not identified and can vary in a specific range. If their thresholds can be set manually from general knowledge, they become floating independent parameters, whose minimum and maximum values are fixed and do not depend on any other model parameters. The majority of floating parameters in our model are independent, including both exoplanet parameters (orbital eccentricity, inclination, longitude of ascending node, argument of periapsis and radius) and ring parameters (ring eccentricity, obliquity, azimuthal angle and argument of periapsis).

2.2.1. Ring proportions

The only two dependent parameters of our model are the ring's **semi-major axis** (half of the longer diameter of an ellipse) and its **width**. With high accuracy, the ring is two-dimensional, with negligible depth. There are several key values for setting the thresholds of the semi-major axis. The first of them is the exoplanet radius. It is evident that the ring's **periapsis** (closest point to the exoplanet) must be located outside the planet's radius. From the ellipse geometry, the ring's periapsis distance r_p can be expressed as $r_p = a(1-e)$. Thus, the minimum possible value of the ring's semi-major axis is:

$$a_{\min} = \frac{R}{1-e} \tag{2.2.1}$$

Regarding the maximum possible value of the semi-major axis, typical planetary rings usually exist inside the **Roche radius** of a body (Tiscareno et al., 2013), a distance beyond which a moon held only by its own gravitation would be torn apart due to **tidal forces** (differential gravitational pulls exerted on different parts of this moon by the host body). This is how most ring systems are formed. The Roche radius is given by:

$$d_{\text{Roche}} = R\left(\frac{4\pi D}{\gamma\rho}\right)^{1/3} \approx 2.44R\sqrt[3]{\frac{D}{\rho}} \tag{2.2.2}$$

using the value of the dimensionless parameter $\gamma = 0.85$ (Chandrasekhar, 1969; Murray & Dermott, 2012) to yield the greatest possible Roche limit (because 0.85 is the smallest possible value of γ). Since we suppose that the ring is fully inside the Roche radius, its **apoapsis** (a point of the ring, which is the furthest from the exoplanet) distance $r_a = a(1+e)$ must be less than or equal to the Roche radius:

$$a_{\max} = \frac{d_{\text{Roche}}}{1+e} \tag{2.2.3}$$

Although it is well-known that even in our Solar System, some objects, for example, Quaoar (Morgado et al., 2023) and Jupiter (Tajeddine et al., 2017), have their rings spanning outside the Roche radius, in this work, we aim to detect more common types of rings. Thus, for simplicity and faster calculations, we only search for exoplanetary rings inside the Roche limit.

Regarding the ring width, we do not limit its minimum value and set it to $w_{\min} = 0$. As for the maximum value, we still expect the farthest ring particles to have a semi-major axis less than or equal to the maximum possible value. Thus, the maximum ring width along the major axis must be equal to:

$$w_{\max} = a_{\max} - a \tag{2.2.4}$$

2.2.2. Ring orientation and eccentricity

Apart from setting the ring's semi-major axis and width, it is necessary to set its orientation parameters. These include its obliquity, azimuthal angle and argument of periapsis. The **obliquity (θ)** is the angle between the stellar equatorial plane and the plane of the ring. The **azimuthal angle (ϕ)** is the angle between the line of sight and the ascending node of the ring in a plane, parallel to the stellar equator. The **argument of periapsis (ψ)** is the rotation of the ring in its own plane, the angle between its ascending node and the ring's periapsis. The **ascending node** is the orbital point where an object crosses the stellar equatorial plane from south to north. Another ring parameter is its **eccentricity (e),** a quantity determining how elongated it is, measured from 0 (circular) to 1 (elongated). See the visualization of these parameters with 2D grid representations of the rings in Figure 2.

The two limiting cases for the orientation of the exoplanetary rings are called **edge-on** and **face-on** ring positions. The rings are considered to be **edge-on** when their normal axis (the direction perpendicular to the plane of the rings) is perpendicular to the observer's line of sight (a straight line of the observer's vision). It makes rings appear as they are viewed from the side, rather than from above or below, which makes them almost invisible. This condition is set by obliquity $\theta = 0^\circ$ or azimuthal angle $\phi = 90^\circ$. The **face-on** rings, on the contrary, occur when their own plane is perpendicular to the line of sight ($\theta = 90^\circ$ or $\phi = 0^\circ$).

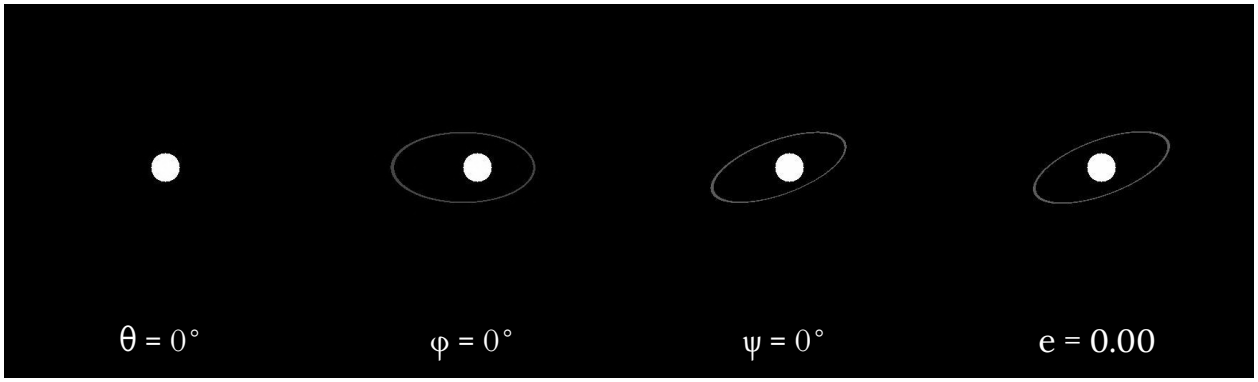

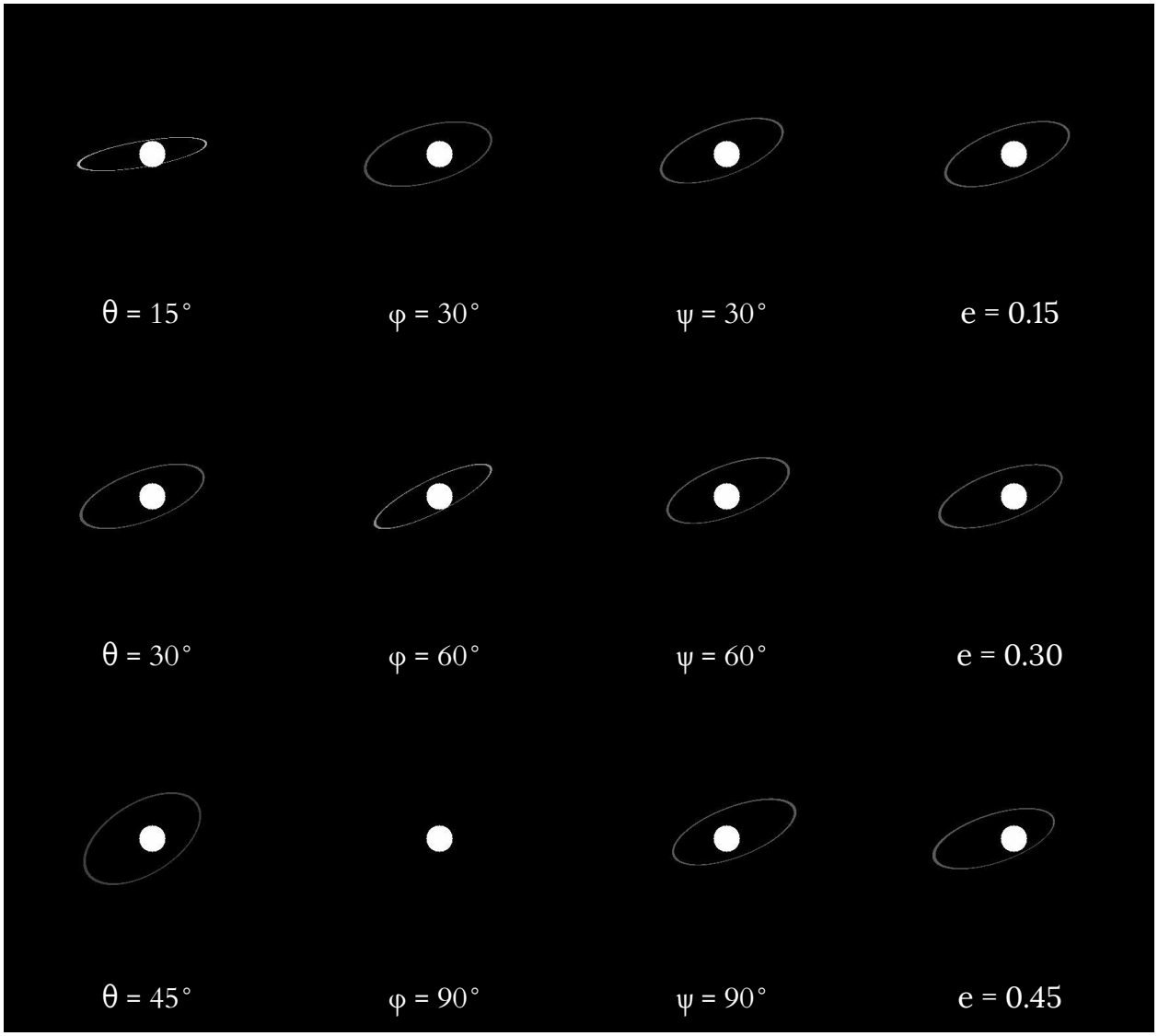
θ = 15°
φ = 30°
ψ = 30°
e = 0.15
θ = 30°
φ = 60°
ψ = 60°
e = 0.30
θ = 45°
φ = 90°
ψ = 90°
e = 0.45

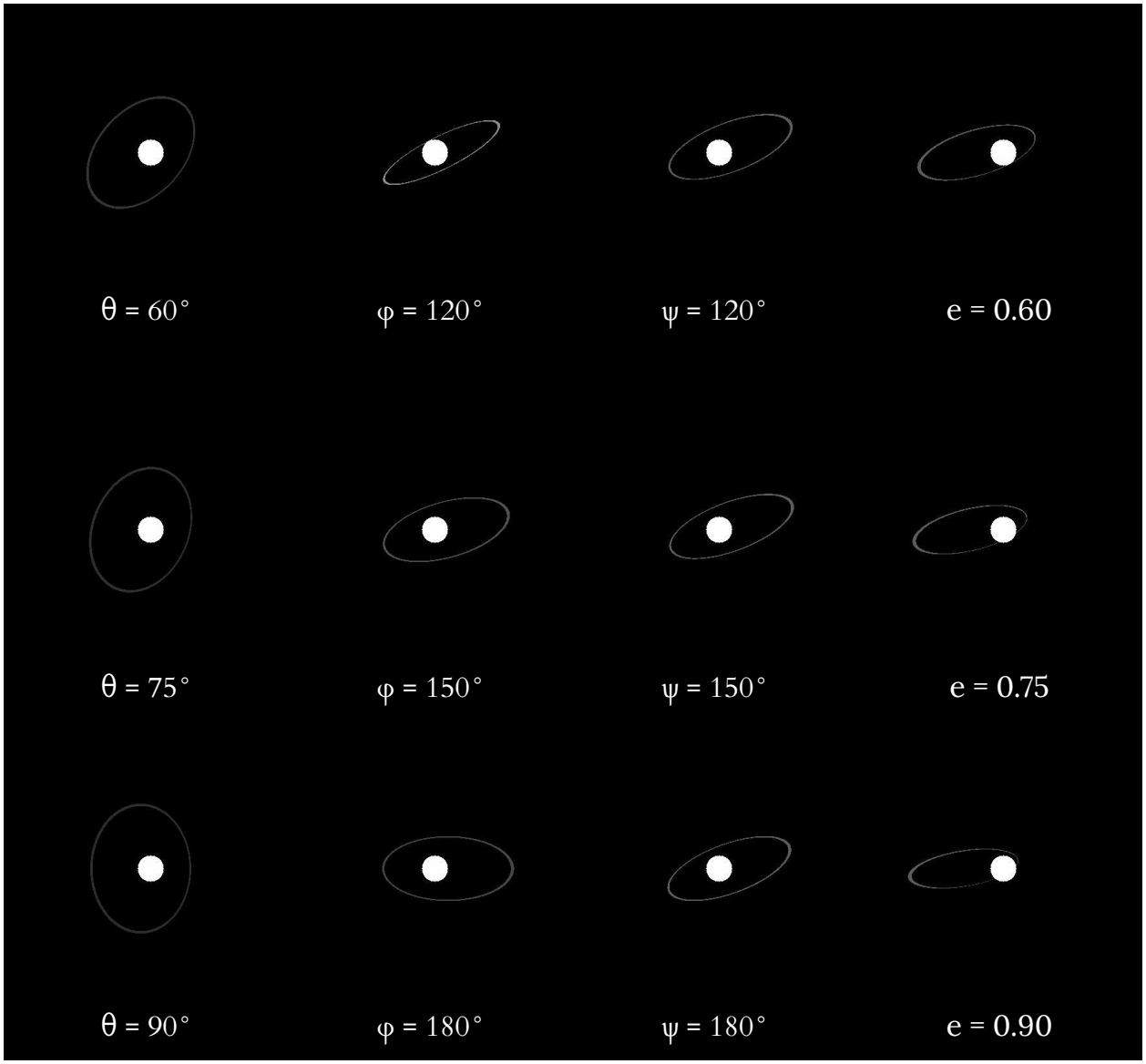

Figure 2: Ring parameters and how they affect the 2D ring matrix projection of a ring with optical depth $\tau = 1.4$. The first column shows the 2D projection for different obliquity values, the second column - for values of azimuthal angle, the third column - for values of argument of periapsis, and the last column - for various eccentricity values. Ring transparency is not depicted to scale; however, it represents the effect of $\sec \eta$ on the optical depth (see Section 2.4). Note that the ring is not visible when it is edge-on ($\theta = 0°$ or $\phi = 90°$). Unless mentioned otherwise above, the ring is depicted for parameter values of $\theta = 30°$, $\phi = 40°$, $\psi = 0°$ and $e = 0.2$; exoplanetary radius of 20 pixels and ring semi-major

axis of 100 pixels. This figure serves as a visual definition of the rotational properties of the exoplanetary ring and its eccentricity, showing how the four parameters alter the ring's projected area and shape on the pixel grid. The pixel-based model successfully translates the 3D ring geometry to a 2D Cartesian plane, allowing for numerical integration of any ring configuration.

2.2.3. Exoplanetary radius

One more parameter that must be set floating is the **radius** of the exoplanet. Technically, it can be obtained from **transit least squares** (TLS) fitting (Hippke & Heller, 2019). However, the transit depth would be highly affected by the existence of a ring and the TLS algorithm might return invalid exoplanet radii. Therefore, some studies attribute the phenomenon of exoplanetary **super-puffs** to incorrect radius measurements because of the presence of ring systems (Piro & Vissapragada, 2020). The only way to deal with this issue is to set the exoplanet radius floating.

2.2.4. Exoplanetary orbit

The exoplanet's orbit is unambiguously set by five parameters: semi-major axis, eccentricity, inclination, longitude of ascending node and argument of periapsis. The semi-major axis is derived directly from the **orbital period** and the **host star's mass** (for this, see Section 2.3). The **eccentricity (**e_p**)** is also set to vary. In our model, we do not require circular orbits as other studies do (Aizawa (逢澤正嵩) et al., 2017; Heising et al., 2015), allowing it to be set to high values, which might make the model applicable to many more exoplanets (for instance, HD 20782, see Jones et al., 2006). The orbital **inclination (**i**)** is the angle between the stellar equator plane and the orbital plane. In our case, we assume that the star is located directly at the point of the autumnal equinox for simplicity, so **the longitude of the ascending node (**Ω**)** is the angle between the line of sight and the ascending node of the orbit in the plane of the stellar equator. Finally, the **argument of periapsis (**ω**)** represents the rotation of the orbit in its own plane, the angle between its ascending node and the orbit's periapsis. These three parameters are also not limited and can take all possible values. See the visualization of these parameters with 2D matrix representations of the orbits in Figure 3.

Similarly to the two limiting cases for the orientation of the exoplanetary rings, the limiting orbit orientations are called **edge-on** and **face-on** orbits. The orbit is called **edge-on** when it is lying in the plane of the observer's line of sight. This condition is set by inclination $i = 0^\circ$ or longitude of ascending node $\Omega = 90^\circ$. A **face-on** orbit occurs when its own plane is perpendicular to the line of sight ($i = 90^\circ$ or $\Omega = 0^\circ$).

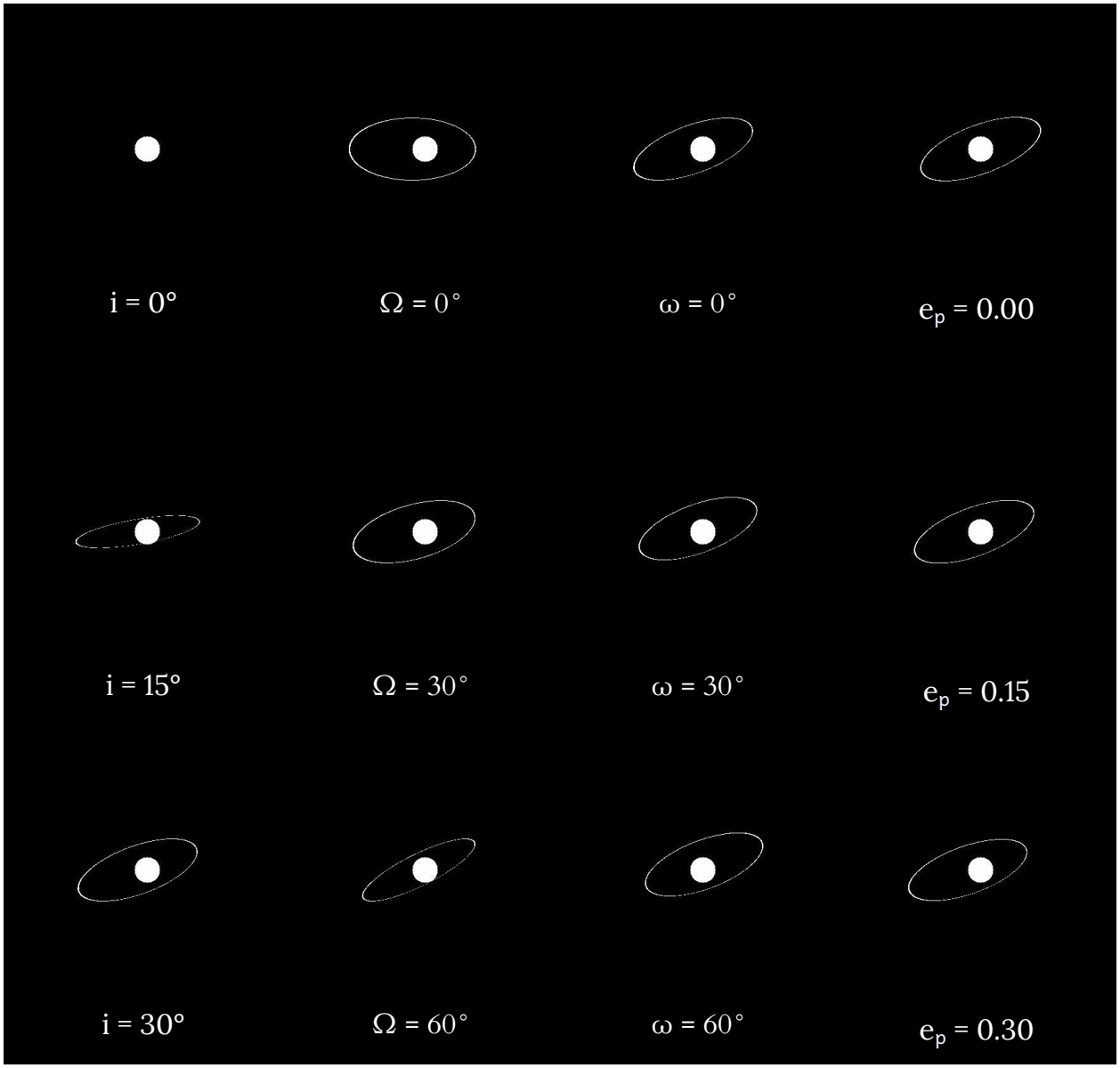
i = 0°
Ω = 0°
ω = 0°
e_p = 0.00
i = 15°
Ω = 30°
ω = 30°
e_p = 0.15
i = 30°
Ω = 60°
ω = 60°
e_p = 0.30

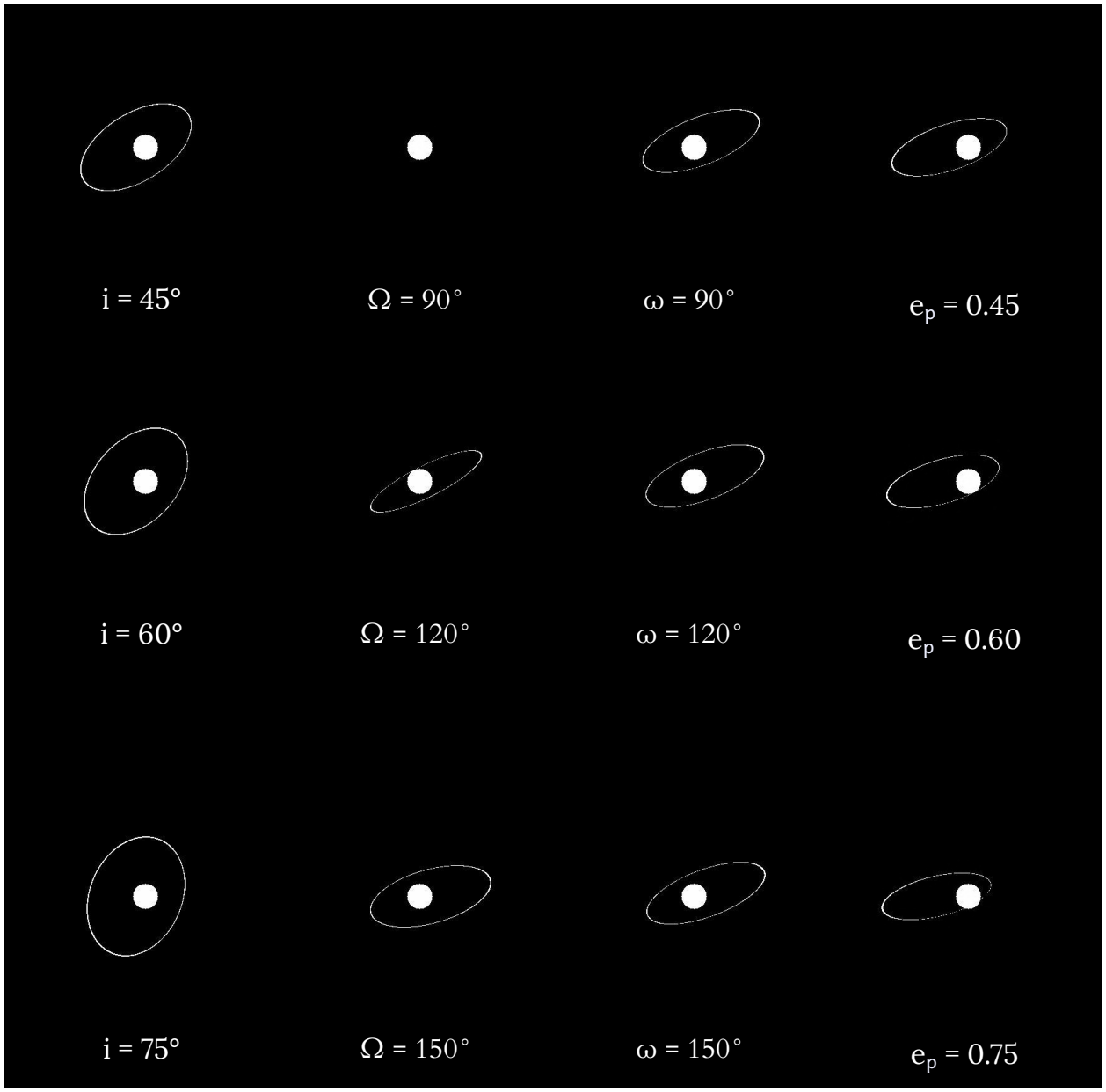
i = 45°
Ω = 90°
ω = 90°
e_p = 0.45
i = 60°
Ω = 120°
ω = 120°
e_p = 0.60
i = 75°
Ω = 150°
ω = 150°
e_p = 0.75

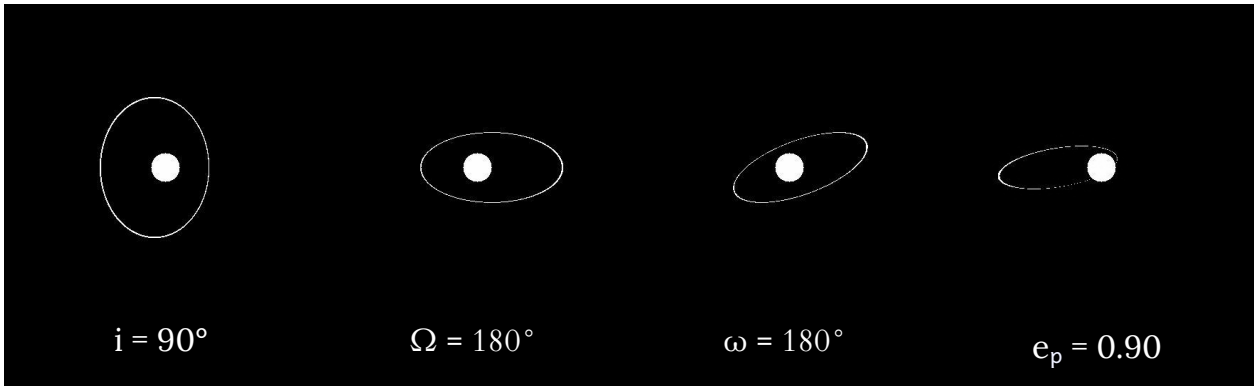

Figure 3: Exoplanet parameters and how they affect the 2D orbit matrix projection. The first column shows the 2D projection for different inclination values, the second column - for values of longitude of ascending node, the third column - for values of argument of periapsis, and the last column - for various eccentricity values. When no orbit is displayed, it symbolizes that the orbit lies edge-on. Unless mentioned otherwise above, the orbit is drawn for parameter values of $i = 30°$, $\Omega = 40°$, $\omega = 0°$ and $e_p = 0.2$; stellar radius of 20 pixels and exoplanetary semi-major axis of 100 pixels. This figure illustrates how the orbital parameters affect the exoplanetary transit trajectory across the stellar disk, which defines the transit duration and light curve features. Transit length and occurrence are heavily reliant on the rotational orientation of the ring and its eccentricity.

2.3. Fixed input parameters

In this work, we implement the nested sampling algorithm (see Sections 3 and 4.2-4.4) to obtain the posterior distribution (Gilks et al., 1995). Thus, it is necessary to minimize the number of floating parameters to decrease the calculation time. Based on this rationale, we selected the following parameters to be fixed in our model: **stellar radius (**R_S**)**, **temperature (**T**)** and **logarithm of acceleration due to gravity (**$\log(g)$**)**; exoplanet **orbital period (**P**)** and **mass (**M**)**; ring **specific absorption coefficient** (κ, light absorption by ring particles by a unit of density); **wavelength (**λ**) / band** and **matrix pixel size (**px**)**. See their default values in Table 1 and the values for parameter estimation in Section 3.

Since the data about stars is much more abundant, the host star's radius, temperature and logarithm of gravitational acceleration are taken as fixed values. These parameters play a vital role in the algorithm as they define the limb-darkening coefficients (for both Díaz-Cordovés & Giménez, 1992 and Claret & Giménez, 1992). Thus, by getting the limb-darkening coefficients from the physical properties of a star, we aim to have fewer floating parameters than other models that select the limb-darkening coefficients as model parameters instead of stellar physical properties (Aizawa (逢澤正嵩) et al., 2017; Heising et al., 2015). The radius is essential for building a star matrix of a relevant size. The semi-major axis of the exoplanet (critical for correct orbital mechanics implementation) is calculated as a function of its period and stellar mass by the 3rd Kepler's Law of planetary motion:

$$A = \sqrt[3]{\frac{P^2 G M_S}{4\pi^2}} = \sqrt[3]{\frac{P^2 g R_S^2}{4\pi^2}} \tag{2.3.1}$$

Unlike an exoplanet's radius and most of its orbital parameters, its orbital period and mass are considered known as they are based on the **peak period** (the amount of time between two consecutive main minima in the light curve) and spectroscopic features (Mayor et al., 2014), respectively. They are not noticeably influenced by the presence of rings in the case of radius measurement errors (Libby-Roberts et al., 2020). Thus, they can be set as fixed parameters and obtained through TLS fitting and spectroscopic measurements.

The optical depth of the ring is defined by its density and specific absorption coefficient:

$$\tau = \kappa\rho \tag{2.3.2}$$

Although the ring density is unknown, we want it to be fixed during data analysis. As density only affects the Roche radius and the optical depth of the ring, its effect on the light curve is not too critical. Thus, for convenience, we assume that it is equal to Roche critical density (maximum possible density of a body that is derived from its Roche radius, see Tiscareno et al., 2013) for a Roche lobe with uniform density ($\gamma = 1.6$, Porco et al., 2007):

$$\rho_{\text{Roche}} = \frac{3M}{\gamma a^3 (1+e)^3} \tag{2.3.3}$$

This approach is justifiable from two rationales. First of all, selecting the nearly maximum possible density value (we apply $\gamma = 1.6$ instead of $\gamma = 0.85$ to get a more realistic density value closer to its average) maximizes the optical depth, which enhances ring detectability, relating to the best-case scenario. Secondly, it decreases the Roche radius (see formula 2.2.2). This simplification results in decreasing the number of iteration steps for the semi-major axis parameter, which is highly favorable for faster calculations.

As for the specific absorption coefficient, it must be selected to match the chemical composition of the ring. While the optical depth of the ring was neglected by some studies (e.g., Heising et al., 2015), others suggest that its impact on the optical depth is underrated, and it is important to deal with **absorption**, **particle sizes** and **forward scattering effects** (the deflection of rays by a small angle due to particle size and other factors, see Barnes & Fortney, 2004b). Running the simulation can help us come to a realistic conclusion about whether the parameter should be included or not (for our findings, see Section 4.1.2).

Wavelength or band of the observations is also important to consider. It affects both the limb-darkening coefficients and the specific absorption coefficient of the ring dust particles. For obtaining the coefficients u_1, u_2 for the **quadratic model** (Claret & Giménez, 1992), the band in either the **UBV system** (Johnson & Morgan, 1953) or **Strömgren photometric system** (Strömgren, 1956) must be selected: U, B, V u, b or v. For applying the **square root limb-darkening model** (Díaz-Cordovés & Giménez, 1992), the wavelength is used to select the most appropriate coefficients u_3, u_4 - there are five available values for the wavelength: $3{,}437\mathring{A}; 4{,}212\mathring{A}; 4{,}687\mathring{A}; 5{,}475\mathring{A}; 6{,}975\mathring{A}$. Regarding the effect of wavelength on the specific

absorption coefficient, it is noticeable enough. For instance, for rings made of silicate grains, the absorption is highly wavenumber-dependent (Boudet et al., 2005; Utry et al., 2014).

Another unique parameter of our model is the matrix pixel size. It is a "scale factor" that helps us convert linear sizes of objects into measurements on a matrix grid, a physical length represented by a single pixel in the model:

$$\mathrm{px} = \frac{l}{\chi} \tag{2.3.4}$$

where l is the physical length of any object in the observed system and χ is its size in pixels in the matrix grid.

It is a constant used to scale real-world measurements, converting them to lengths in pixels for the computer model. See the values fixed parameters were set to during data-fitting in Table 2.

2.4. Creating the masking array and the star model

The parameters set in Subsections 2.1-2.3 must then be used to create the pixelated models of the star and the masking matrix of an exoplanet with its rings. In this section, this process will be described in detail, including the projection of the model of a ringed exoplanet with 3D rotation to a 2D matrix space with distances in pixels and filling each pixel with its specific value.

The masking matrix, represented by a NumPy array (Harris et al., 2020), consists of two key components: the circular model of the exoplanet and the 2D projection of its ring. These matrices are created independently, yielding the optical depth of every pixel $\tau(x, y)$, and then summed (putting the exoplanet at the focus of the ring) in order to calculate the optical depth of every pixel in the masking matrix. To sum two matrices, they are required to have the same size. It is highly important to select a relevant **matrix size** (the width or the length of a square matrix) since a smaller size allows for faster transit light curve calculations later (see Section 2.5) and avoids the ring matrix being cropped. For this reason, we introduce the variable of matrix size n (i.e., a square matrix of size $n \times n$). As it is measured in pixels and the coordinates of the matrix center should be integers for relevant exoplanet and ring depiction, this variable is constrained to odd integers.

The farthest distance from the ring's focus to any point in the 2D projection must not exceed its apoapsis (as when the ring is rotated, this distance decreases). As the ring may be parallel to the star's equator and we need to handle its width and eccentricity, the minimum possible universal matrix size should be equal to:

$$n = 2\left[\frac{(a+w)(1+e)}{2\mathrm{px}}\right] + 1 \tag{2.4.1}$$

Next, the model identifies the matrix center coordinate c:

$$c = \frac{n-1}{2} \tag{2.4.2}$$

After setting the size of the matrix, the model creates a simple circular model of the exoplanet. First, it fills the matrix with optical depth $\tau(x, y) = 0$. Then, using the equation of a circle, it fills all the points inside the exoplanetary radius in pixels $\chi_R = \frac{R}{\text{px}}$ with optical depth $\tau(x, y) \to \infty$. We assume that the planet fully covers the light from the star in this area and does not reflect any light, as we observe the transit stage only, where its phase is really close to 0.

After constructing the exoplanet model, the next step is to project the ring orientation into two dimensions, so that the combined 2D matrix of the planet and its rings can be stacked onto the pixel-grid representation of the host star.

At first, the semi-major axes of ring borders α_{inner} and α_{outer} (in pixels) are calculated:

$$\alpha_{\text{inner}} = \alpha + \frac{\chi_w}{2}, \alpha_{\text{outer}} = \alpha - \frac{\chi_w}{2},$$

where

$$\alpha = \frac{a}{\text{px}} \text{ and } \chi_w = \frac{w}{\text{px}}. \tag{2.4.3}$$

The physical orientation of the exoplanetary ring in 3D space is defined by three **Euler angles** (three specific angles used to describe the orientation of a body in 3D space by a sequence of three rotations around different axes): θ (ring obliquity), ϕ (ring azimuthal angle), and ψ (ring argument of periapsis).

Each angle represents the rotation about one specific axis in the Cartesian space (x, y, or z). These rotations can be described using **rotation matrices** (Weisstein, 2002), linear transformations that sustain the length of vectors and the coordinate system's handedness.

To obtain the final, combined 3D orientation, we apply **Euler's Rotation Theorem** (Euler, 1776), which states that any rotation in 3D space can be represented by a single rotation about a fixed axis. In matrix algebra, the composition of successive rotations is achieved by multiplying the individual rotation matrices (Donchev et al., 2015) to get a **combined rotation matrix** (R):

$$R = R_\phi \times R_\theta \times R_\psi, \tag{2.4.4}$$

where R_θ, R_ϕ, and R_ψ are 3D rotation matrices of angles θ (ring obliquity), ϕ (ring azimuthal angle), and ψ (ring argument of periapsis) around the x, y, and z axes, respectively. The rotation matrix R is a 3×3 matrix describing how the ring is oriented in 3D space. Since the ring is flat, its projection mostly depends on how its plane is tilted in x and y, we only need the top-left 2×2 part, which we call N.

The calculation of the matrix determinant is necessary at this stage to establish a mathematical guardrail against a singular projection. The determinant ($\det N$) is in the denominator of the inverse transformation formula (equation 2.4.6), meaning

the matrix N must be invertible ($\det N \neq 0$). If the ring is viewed almost edge-on ($\det N \to 0$), the transformation becomes unstable, and the ring is skipped, that is, $\tau(x, y) = 0$. This check prevents division by zero and handles the physically singular case where the ring collapses toward a line.

To map the observed coordinates (x and y) in the ring's plane (coordinates x_r and y_r), we apply the **inverse transformation** which is equivalent to applying Euler's (Euler, 1776) rotation theorem in reverse, using the inverse matrix (Weisstein, 2002).

Then, all the possible coordinate pairs are created. For this, a 1D array L with all possible $x - c$ and $y - c$ values (where $x - c = y - c$) is created. It is linearly spaced from $-\frac{n}{2}$ to $\frac{n}{2}$ with a total of n values.

For yielding every possible coordinate pair, X and Y matrices are created for x and y coordinates, respectively:

$$X_{i,j} = L_i, Y_{i,j} = L_j \tag{2.4.5}$$

The coordinates (x_r, y_r) in the ring's plane are obtained by multiplying the observed coordinates (x, y) by the inverse matrix N^{-1}. The component form of this inverse transformation, derived directly from the general formula for the inverse of a 2×2 matrix N^{-1} (Weisstein, 2002), is:

$$x_r = \frac{m_{22}x - m_{12}y}{\det N}; y_r = \frac{-m_{21}x + m_{11}y}{\det N}, \tag{2.4.6}$$

where m_{ij} are the components of the matrix N. From this, we can extract the orbital distance χ for each point (using the Pythagorean theorem) and the true anomaly ν_r

$$\chi = \sqrt{x_r^2 + y_r^2} \tag{2.4.7}$$

$$\nu_r = \arctan 2(y_r, x_r) \tag{2.4.8}$$

Using the ellipse equation in polar coordinates, the model constructs the inner and outer borders r_{inner} and r_{outer} of the ring:

$$r_{\text{inner}} = \frac{\alpha_{\text{inner}}(1-e^2)}{1+e\cos\nu_r} \tag{2.4.9}$$

$$r_{\text{outer}} = \frac{\alpha_{\text{outer}}(1-e^2)}{1+e\cos\nu_r} \tag{2.4.10}$$

We fill the ring by its optical depth, enhanced by a factor $\sec\eta$(because the ring is 2D), for all pixels outside the inner border and inside the outer border, where η is the angle between the line of sight and the normal axis of the ring in the plane in which the two lines lie within:

$$\cos\eta = \hat{A}_N \cdot \hat{A}_{\mathrm{LOS}}, \tag{2.4.11}$$

where $\hat{A}_{N_i} = R_{i,2}$ is the **unit normal axis vector** (the direction, perpendicular to the plane of the rings) and $\hat{A}_{\mathrm{LOS}} = \hat{z}$ is the **unit line of sight vector** (a straight line of the observer's vision). This is derived directly from the definition of a dot product of two vectors: $\|\hat{A}_N\|\|\hat{A}_{\mathrm{LOS}}\|\cos\eta = \hat{A}_N \cdot \hat{A}_{\mathrm{LOS}}$, where $\|\hat{A}_N\|\|\hat{A}_{\mathrm{LOS}}\| = 1$ as $\hat{A}_N$ and $\hat{A}_{\mathrm{LOS}}$ are both unit vectors. For getting the matrix array, the program sums the matrices of the exoplanet and its ring.

The final preparation step before modeling the transit stages is creating the model of the star. This is done simply by filling the matrix of a different size $n_S = 4\left[\frac{R_S}{2\mathrm{px}}\right] + 1$ by normalized intensities that are yielded by one of two limb-darkening models. The choice of a particular limb-darkening model depends on several factors:

- Data availability. Our models take coefficients u_1, u_2 from Claret & Giménez, 1992 that have parameter combinations from Table 1, and coefficients u_3, u_4 from Díaz-Cordovés & Giménez, the parameter combination availability is shown in Table 1.
- The physical properties of a star. Generally, it is advised to use the quadratic model for colder stars with lower $\log(g)$ and the square root model for hot stars with higher $\log(g)$ values (Espinoza & Jordán, 2016).
- Custom models. The users can download their own limb darkening models with coefficients or even NumPy array representations (Harris et al., 2020) for specific stars or needs.

In the analysis of HIP 41378f, the quadratic limb-darkening is used due to the high $\log(g)$ value for the host star HIP 41378 ($\log(g) = 4.3$, detected by TICv8). As prior analysis of the HIP 41378's planetary system was made and the values of limb-darkening coefficients were verified across several planets in the system, we assume that the limb-darkening coefficients of the star do not need further fitting and are fixed to 0.0678 and 0.188 (Grant & Wakeford, 2024).

For the model, the parameter μ, the cosine of the angle between the emergent radiation and the perpendicular to the stellar surface, is calculated for each pixel by:

$$\mu = \cos\left(\frac{\pi}{n}\sqrt{(x-c)^2 + (y-c)^2}\right) \tag{2.4.12}$$

Then, it is converted to the normalized intensity map $I(\mu)$ using the coefficients and the main formula of a selected model.

Table 1: All available parameter combinations for the quadratic model (Claret & Giménez, 1992) compared to available combinations for the square root model (Diaz-Cordoves & Giménez, 1992). In the first column, all possible values for

temperatures are displayed, with the second and third columns demonstrating all corresponding band (quadratic model) / wavelength (square root) values.

Quadratic model			**Square root model**		
174 available combinations			60 available possible combinations		
T, K	$\log(g)$	Band	T, K	$\log(g)$	λ, $\mathring{A}$
4,000	2.00 2.50 3.00 3.50 4.00	u b v U B V	5,500	3.00 4.00	3,437 4,212 4,687 5,475 6,975
4,500	2.00 2.50 3.00 3.50 4.00 4.50	u b v U B V	6,000	4.00	3,437 4,212 4,687 5,475 6,975
4,600	3.00	u	7,000	4.00	3,437

		b v U B V			4,212 4,687 5,475 6,975
4,700	3.44	u b v U B V	8,000	3.00 4.00	3,437 4,212 4,687 5,475 6,975
5,000	2.00 2.50 3.00 3.50 4.00 4.50	u b v U B V	10,000	3.00 4.00	3,437 4,212 4,687 5,475 6,975
5,300	2.50 3.44	u b v	15,000	3.00 4.00	3,437 4,212 4,687

		U B V			5,475 6,975
5,460	3.44	u b v U B V	20,000	3.00 4.00	3,437 4,212 4,687 5,475 6,975
5,500	3.00 3.50	u b v U B V			
5,780	4.44	u b v U B			

		V			
6,000	4.50	u b v U B V			
6,020	3.44	u b v U B V			
6,300	3.44	u b v U B V			

6,730	4.50	u b v U B V			

2.5. Transit model

In this section, the final and most important step of modeling is described. Now that all the parameters are set and the matrices of the star, exoplanet and its rings are computed, it is time to calculate the light curve, paying attention to the orbital parameters of the exoplanet.

The first step to achieving this goal is to project the orbit of the planet in 3D to 2D coordinates in the viewed plane. Similar to the projection of the rings, the rotation matrices (Weisstein, 2002) are obtained and multiplied to get a combined rotation matrix:

$$R_o = R_\Omega \times R_i \times R_\omega, \tag{2.5.1}$$

where R_i, R_Ω, and R_ω are 3D rotation matrices of angles i (inclination), Ω (longitude of ascending node), and ω (argument of periapsis) around the x, y, and z axes, respectively.

The next step is to calculate the initial star brightness I_0 in units of the brightest star pixel by summing the normalized intensity values of all pixels.

Then, the program calculates the coordinate c_S of the central point of the star matrix:

$$c_S = \frac{n_S - 1}{2} \tag{2.5.2}$$

The maximum distance between the star matrix center and the masking matrix center, where a transit is still possible, Γ is expressed as:

$$\Gamma = c_S + c\sqrt{2} \tag{2.5.3}$$

Here, we assume that the masks align diagonally, so c_S is the radius of the star in pixels and $c\sqrt{2}$ is the half-diagonal of the masking matrix.

In order to detect the transit, we have to narrow down the search window. For this, at first, we identify the **true anomaly** ν_c (the angle between the orbit's periapsis and the current planet position) of the orbital point when the exoplanet is right in front of the host star from spherical trigonometry:

$$\nu_c = \arctan 2(1, \cos i \tan \Omega) - \omega \tag{2.5.4}$$

There are two possible solutions for ν_c, so if the planet does not pass in front of the star, we add $180°$ to ν_c.

The true anomaly is then converted to the **eccentric anomaly** E_C - the angle between the orbit's periapsis and the position of the exoplanet projected to the auxiliary circle of the elliptical orbit. The relationship between true anomaly and eccentric anomaly can be seen in Figure 4.

The eccentric anomaly is then converted to **mean anomaly** m_c - the angle between the orbit's periapsis and the current planet position, calculated as if the planet is moving at a constant speed on a circular orbit with the same focus location as the ellipse. The mean anomaly is consequently converted to the **orbital time** t_c - the time between the periapsis of the planet and its current position - using **Kepler's equation**:

$$E_c = \arctan 2(\sqrt{1 - e^2} \sin \nu_c, e_p + \cos \nu_c) \tag{2.5.5}$$

$$m_c = E_c - e_p \sin E_c \tag{2.5.6}$$

$$t_c = \frac{m_c P}{2\pi} \tag{2.5.7}$$

The search window's half duration is defined as double the estimated transit duration for safety and simplicity, where 2Γ (twice the sum of star radius and mask diagonal) is the distance the planet has to cover, and $\frac{2\pi\alpha_p}{P}$ the **average orbital speed** (in pixels per second), where α_p is the planet's semi-major axis in pixels.

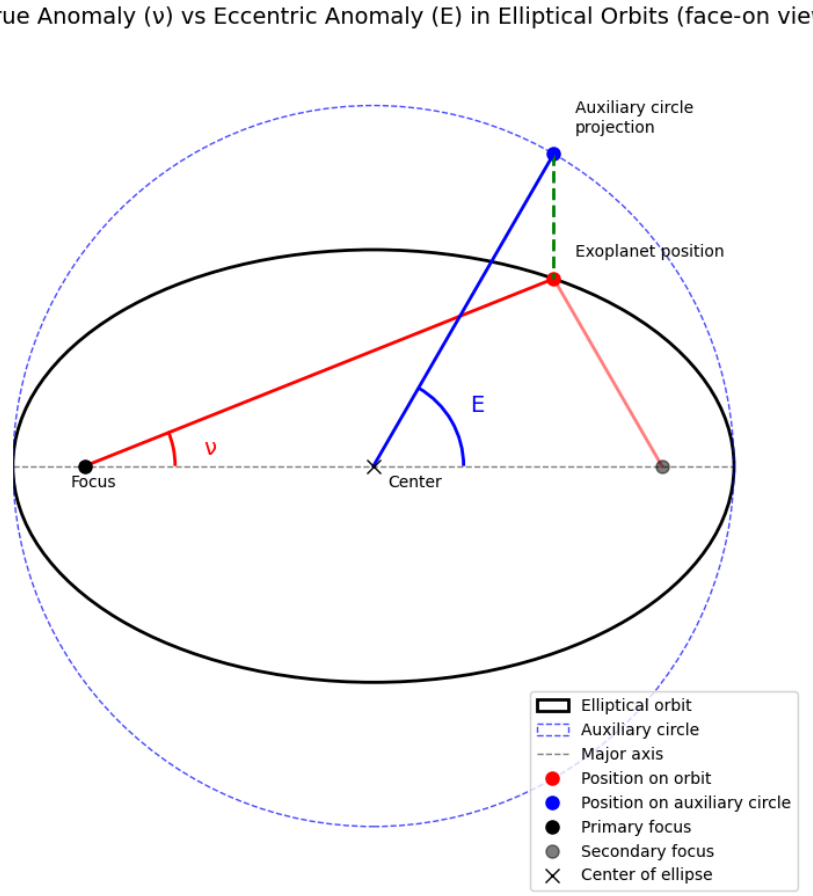

Figure 4: Geometric relationship between true anomaly () and eccentric anomaly () in elliptical orbits. The vertical projection of the exoplanet's position on the auxiliary circle (green dashed line) relates the eccentric anomaly to the true orbital position. The major axis (black dashed line) spans the entire length of the ellipse through both foci. The figure was created for an eccentric orbit with the eccentricity of 0.8 in the face-on orientation. The figure confirms the mathematical relationship used by the model to calculate planet positions and velocity at any given time step.

Thus, the half duration of the search window t_s is then defined as:

$$t_s = \frac{2P\Gamma}{\pi\alpha_p}, \tag{2.5.8}$$

We set the number of orbital time steps to $s_o = 400$. This is the number of times the orbital time is changed when finding the **transit window** (a period of time when the transit is observable). This value is not set as an input parameter for the model for simplicity and is automatically set to this value to allow detecting a transit quickly and accurately. We define the search window for the transit as an array of orbital times, linearly spaced from $t_c - t_s$ to $t_c + t_s$, containing a total of s_o elements: $[t_c - t_s, \ldots, t_c + t_s]$.

The next vital step is to calculate the orbital position of the exoplanet at every time step. For this, our program numerically solves Kepler's equation for an ellipse by:

- Calculating the mean anomaly

$$m = \frac{2\pi t}{P} \tag{2.5.9}$$

- Using the **Newton-Raphson method** (Vera et al., 2019) to numerically get the value of the eccentric anomaly:

$$m = E - e_p \sin E \tag{2.5.10}$$

- Finding the true anomaly:

$$\tan \frac{\nu}{2} = \sqrt{\frac{1+e_p}{1-e_p}} \times \tan \frac{E}{2} \tag{2.5.11}$$

$$\nu = 2 \arctan 2(\sqrt{1+e_p} \tan \frac{E}{2}, \sqrt{1-e_p}) \tag{2.5.12}$$

After getting the true anomaly for an orbital point, the program calculates its **position** r (the distance between the star and the exoplanet) by applying the **ellipse equation in polar coordinates**:

$$r = \frac{A(1-e_p^2)}{1-e_p \cos \nu} \tag{2.5.13}$$

Since the orbit is 2D, the position vector is equal to:

$$\vec{r} = \begin{pmatrix} r \cos \nu \\ r \sin \nu \\ 0 \end{pmatrix} \tag{2.5.14}$$

By applying the rotation matrix, the position vector gets transformed to the position in 3D (Weisstein, 2002):

$$\vec{p} = R_o \times \vec{r} \tag{2.5.15}$$

Then, the program validates whether the transit is occurring in the selected time step by checking the following conditions:

- $p_z \geq 0$ – the planet is not behind the star as its depth is positive.
- $\sqrt{p_x^2 + p_y^2} < \Gamma$ – the masking matrix covers the matrix of the star in the 2D projection.

If the current point is the first in the array to fulfill the clauses above, the transit start time t_{start} is set to t. For the last point to fulfill these requirements, the transit end time t_{end} is set to t.

Therefore, transit duration is:

$$t_d = t_{\text{end}} - t_{\text{start}} \tag{2.5.16}$$

Next, another preset parameter $\epsilon = 0.1$ comes into play. This value defines the quotient of the margin of transit duration to its recommended margin, as not to miss any points before the transit start. So, the full transit time for the light curve t_t is defined as:

$$t_t = t_d(1 + 2\epsilon) \tag{2.5.17}$$

Then, the light curve in the transit time span is calculated with more steps to return a much better resolved light curve with more data points, defined by variable $s = 500$.

For this, an array of time points, consisting of s elements, is created from $t_{\text{start}}(1 - \epsilon)$ to $t_{\text{end}}(1 + \epsilon)$.

For each of these time steps, the exoplanet's position is recalculated with formulas 2.5.9-2.5.15.

Then, the program masks one array by another by calculating the coordinates of the top-left corner of the masking array x_t, y_t, the horizontal and vertical coordinate ranges for the masked star slice $[x_{S_0}, x'_S]$ and $[y_{S_0}, y'_S]$ (ensuring that they do not cross the border of the star matrix by cutting the masking matrix) and the horizontal and vertical coordinate ranges for the covering matrix $[x_0, x']$ and $[y_0, y']$ (handling cases when the matrix extends outside the star matrix). These variables are defined as:

$$x_t = \left[c + p_x - \tfrac{n}{2}\right]; \; y_t = \left[c + p_y - \tfrac{n}{2}\right] \tag{2.5.18}$$

$$x_{S_0} = \max(0, x_t); \; y_{S_0} = \max(0, y_t) \tag{2.5.19}$$

$$x'_S = \min(n_S, x_t + n); \; y'_S = \min(n_S, y_t + n) \tag{2.5.20}$$

$$x_0 = \max(0, -x_t); \; y_0 = \max(0, -y_t) \tag{2.5.21}$$

$$x' = n - \max(0, x_t + n - n_S); \; y' = n - \max(0, y_t + n - n_S) \tag{2.5.22}$$

Then, the new blocked light by the covered star slice is calculated by:

$$\Delta I(x,y) = I(\mu)(1 - e^{-\tau(x,y)}) \tag{2.5.23}$$

The total blocked brightness $\Delta I(t)$ is given by the summation over all pixels of $\Delta I(x,y)$. Finally, the normalized intensity curve $I(t)$ is converted to the light curve $\Delta m(\Phi)$ by:

- Computing the normalized intensity curve:

$$I(t) = I_0 - \Delta I(t) \tag{2.5.24}$$

- Converting the brightness to **magnitude change** (the change in the star's visible brightness in logarithmic units):

$$\Delta m(t) = 2.5 \log \frac{I_0}{I(t)} \tag{2.5.25}$$

- Then, the light curve minimum point is found, and the light curve phase (a normalized time value, measured from 0 to 1, where the transit minimum is 0.5) is centered on it, extending the part with less time before/after the minimum.

- Normalizing the time scale to get the phase:

$$\Phi = \frac{t - t_{\text{start}} + t\epsilon}{t_t} \tag{2.5.26}$$

The model must be thoroughly constructed as it serves as the primary tool for analyzing data. The steps and the methods listed ensure that the model accurately reflects the physical properties of the investigated systems. The following section will demonstrate the practical application of this framework and the process of parameter estimation through nested sampling.

3. Parameter Estimation

This section focuses on describing the algorithm of parameter estimation using Bayesian techniques (methods that are based on Bayes' theorem). It works through processing observational data by running the model described in Section 2 with different values of floating input parameters (see Section 2.2) within their ranges and comparing the yielded $\Delta m(\Phi)$ with the observed data.

For this, the **dynamic nested sampling** (Skilling, 2004; Skilling, 2006; Higson et al., 2019; Feroz et al., 2009) algorithm, which is a computer-driven sampling method used to estimate the properties of complex systems, is then applied. It works by taking a "random walk" through all possible outcomes, where each new step depends randomly, but logically, on the previous one. By collecting thousands of these samples, it can eventually build an accurate picture of the entire system and find the best fit. The nested sampling module uses **log-likelihood** (a logarithmic function that measures how well the model fits the

observations) and **log-prior** (a function representing the initial assumption of parameter distribution density) functions to find the parameters of the best-fit curve.

3.1. Exoplanetary transit of HIP 41378f

In this paper, we apply the proposed algorithm by searching for rings of a super-puff candidate HIP 41378f (Pira & Vissapragada, 2020). A successful fit for this exoplanet would support our hypothesis that exoplanetary ring systems can be detected and characterized using our method.

Before focusing on the method of parameter estimation, it is essential to provide the context about the investigated system and emphasize its relevance to our study. The host star of the exoplanet, HIP 41378, is an F8 main-sequence dwarf (Santerne et al., 2019) in the constellation of Cancer. It has an apparent magnitude of 8.9^m and is located approximately $106\ \mathrm{pc}$ away from the Sun (Berardo et al., 2019). It hosts a system of five known exoplanets. The planet HIP 41378f was discovered using transit photometry (Vanderburg et al., 2016). It drew the attention of scientists due to having an extremely low predicted density value of $90\ \mathrm{kg\ m^{-3}}$ (Santerne et al., 2019). Some hypothesize (e.g., Pira & Vissapragada, 2020) that the anomalously inflated inferred radius could be a result of a ring system, which would significantly affect its inferred radius during a transit without adding significant mass. Thus, HIP 41378f is a perfect example to test the model proposed in this paper.

For the data-fitting, we used combined and processed data from Berardo et al., 2019, who presented the transit light curve in terms of **hours from mid-transit** vs. **relative flux** (ratio of the star's visible brightness to the brightness of the star when no transit occurs). The data was originally taken from C5 (Campaign 5) and C18 (Campaign 18) of K2 (Kepler space telescope). We used the duration of observations presented in Berardo et al., 2019 to convert this to a phase-folded light curve in terms of magnitude change (see Figure 5). It is important to note that by using data that is combined from different observations, we risk encountering the effect of ring and exoplanet **precession** (the slow movement of the axis of a rotating body around another axis), meaning that its configuration might be misinterpreted because of stacking the light curves with the ring in different configurations into one graph. However, we assume that the precession periods of the ring's **nodes** (two points of the ring where the ring's plane intersects with the equatorial plane of the exoplanet), the exoplanet's axis and the exoplanet's orbit are minor compared to the time span when the three combined curves were produced. This is reasonable according to the equations and estimates on this issue from Heising et al., 2015.

3.2. Model parameter values and boundaries

First, for the model to perform calculations on real data, it is necessary to set fixed model parameters to real values of the observed objects. For HIP 41378f, its host star HIP 41378, ring material and the masking matrix these parameters are listed in Table 2.

Generally, using coefficients u_1, u_2 from theoretical tables for modeling limb-darkening is a highly relevant approach for general cases. However, for the particular case of HIP 41378f, we use limb-darkening coefficients estimated in another paper through MCMC (another sampling method, Foreman-Mackey et al., 2013) analysis (Grant & Wakeford, 2024) as it provides more precise coefficient values, and there is no data for these specific values of T and $\log(g)$ in the theoretical tables our model uses (Díaz-Cordovés & Giménez, 1992; Claret & Giménez, 1992). Thus, we replace the fixed values of T and band with

the parameters u_1 and u_2. It is not possible to get rid of accounting for $\log(g)$ as it is essential for calculating the mass of the star as $M = \frac{gR^2}{G}$. Moreover, it is necessary to derive the exoplanet's semi-major axis from $\log(g)$ using Equation 2.3.1, which gives us $A = 1.377\ \mathrm{AU}$.

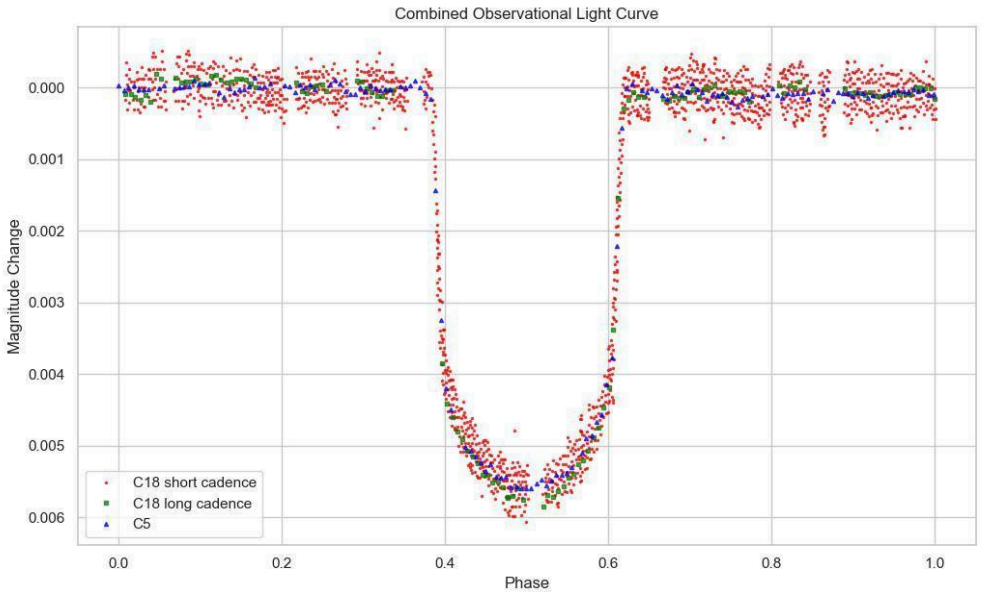

Figure 5. The combined phase-folded transit light curve of HIP 41378f. The red points and the green squares represent the short and the long cadence observed data from K2 Campaign 18, respectively, and the blue triangles represent data from K2 Campaign 5 (Vanderburg et al., 2016). All graphs in the paper are plotted using Matplotlib (Hunter, 2007). This graph shows the data that is to be fit with the model presented in this paper and distinguishes it between three sources of observed data.

Another essential step for an effective nested sampling simulation is setting **prior distributions** (probability distributions that represent the initial belief about the system) for floating parameters (those to be fit) that should be carefully constrained to avoid degeneracies. In our nested sampling, we used **uniform** (a probability distribution where all possible outcomes within given boundaries are equally likely to occur) prior distributions that are **broad** (expressing a high degree of initial uncertainty in the parameter values). This approach was chosen to ensure that the posterior estimates were driven primarily by the experimental data rather than by initial constraints. Despite the use of uniform priors, the majority of resulting posterior distributions exhibited Gaussian characteristics with high shrinkage values (see Section 4.2).

Furthermore, the boundaries for two parameters (ring semi-major axis and ring width) were selected to be **dynamic**, i.e., recalculated every time the model is called based on values of other parameters, using formulas 2.2.1-2.2.4. See all prior distribution boundaries in Table 3.

Table 2. Fixed parameter values for the observations of HIP 41378f. The values of these parameters are not affected by the presence or absence of a ring system around the exoplanet.

Parameter	Value	Source/Rationale
Pixel size, px	$10{,}000$ km	Selected manually to keep both the exoplanet and its ring well-resolved on the pixel map (taking into consideration that its radius should be less than the estimate from Santerne et al. but still of the same order because of the ring hypothesis, and its rings should be wide enough to be reliably distinguished from the planet itself) to avoid spoiling the high precision of the transit light curve while sustaining minor matrix sizes for fast light curve calculations.
Star radius, R_S	$1.28 R_\odot$	Grouffal et al., 2022
Logarithm of stellar surface gravity, $\log(g)$	4.3	detected by TICv8
Exoplanet mass, M	$12 M_\oplus$	Berardo et al., 2019
Exoplanet orbital period, P	542 days	Santerne et al., 2019

Quadratic limb-darkening coefficients, u_1, u_2	$0.0678, 0.188$	Grant & Wakeford, 2024
Ring specific absorption coefficient, κ	$2.3 \times 10^{-3} \frac{\mathrm{m}^2}{\mathrm{g}}$	Utry et al., 2014 (for quartz particles as they are dominant in silicate dust, which is applicable for planets that are not too distant from the host star, like HIP 41378f)

Table 3. Prior distribution boundaries and their classification as static or dynamic for the parameters that are to be fit using the nested sampling algorithm. All prior distributions are uniform.

Prior	Boundaries	Type	Rationale
Exoplanet orbit eccentricity (e_p)	0.0 to 0.9	static	Must not be too close to $e_p = 1$ to avoid huge matrix sizes that can slow down calculations
Exoplanet orbit inclination (i)	0 to 90°	static	Other values of i and ω would result in configurations that are symmetrical to those already existing and, thus, return similar light curve results. The selected range for Ω ensures geometric transit for a large semi-major axis ($A = 1.377$ AU)
Exoplanet longitude of ascending node (Ω)	$90 - 5 \times 10^{-8}$ to $90 + 5 \times 10^{-8}$	static	
Exoplanet argument of periapsis (ω)	0 to 180°	static	

Exoplanet radius (R)	$2{,}000$ km to $9.2R_{\oplus}$	static	Must be lower than in Santerne et al., 2019 as we include the ring, which increases transit depth
Ring eccentricity (e)	0.0 to 0.9	static	Must not be too close to $e_p = 1$ to avoid huge matrix sizes that can slow down calculations
Ring semi-major axis (a)	$R/(1-e)$ to $d_{\text{Roche}}/(1+e)$	dynamic	See Section 2.2.1 and formulas 2.2.1-2.2.3
Ring width (w)	0 to $a_{\max} - a$	dynamic	See Section 2.2.1 and formula 2.2.4
Ring obliquity (θ)	0 to $90°$	static	Other values of these parameters would result in configurations that are symmetrical to those already existing and, thus, return similar light curve results
Ring azimuthal angle (φ)	0 to $180°$	static	
Ring argument of periapsis (ψ)	0 to $180°$	static	

3.3. Nested sampling run

The next step is defining the log-likelihood function ℓ for the nested sampling simulation. If one of the dynamic parameters used in the simulation is outside the boundaries set in Section 2.1, the log-likelihood immediately returns $\ell \to -\infty$. Otherwise, the phases of the points in observational data Φ_{o_j} are converted to phase values for the model Φ_j by:

$$\Phi_j = (\Phi_{o_j} - 0.5)\tfrac{t_o}{t_t} + 0.5, \tag{3.1}$$

where t_o is the time range of the source observational data (in the case of HIP 41378f, $t_o = 80$ hrs) and t_t is the transit duration given by the model.

Then, the log-likelihood function is calculated for a normal distribution:

$$\ell = -\frac{1}{2}\sum_j \left(\frac{(\Delta m_o(\Phi_j) - \Delta m(\Phi_j))^2}{\sigma^2} + \log(2\pi\sigma^2) \right), \tag{3.2}$$

where $\Delta m_o(\Phi)$ is the observed light curve, $\Delta m(\Phi)$ is the predicted light curve and σ^2 is the variance in observational data points that are out of the transit.

Finally, the nested sampling simulation is run with $N_{\text{dim}} = 11$ dimensions (one for each model parameter), $N_{\text{live}} = 500$ live points (pointers in the parameter space), using the Python dynesty module (Speagle, 2020; Koposov et al., 2024) with no changes to its default settings (including the stopping function). See the results in Section 4.2.

4. Validation

This section focuses on the validation of our model. In Section 4.1, we confirm the adequacy of parameter selection for the model by creating synthetic light curves for different values of all parameters, elaborating on their impact on the light curve and, thus, proving that these parameters are essential for the model and are addressed correctly. In Section 4.2, we intend to detect a ring system around HIP 41378f and identify its parameters through data-fitting to see how the model works in practice. In Section 4.3, the model is compared against alternative hypotheses explaining the transit light curve asymmetries. In Section 4.4, we acknowledge the limitations of our model, which need to be considered when reproducing the data analysis or applying our model to other data.

4.1. Effect of the input parameters on the light curve

The parameters used to model the transit light curve of an exoplanet with rings in our algorithm are different from those used in other models (e.g., Heising et al., 2015; Lu et al., 2025; Piro & Vissapragada, 2020). In this subsection, we run the model with different values of each parameter and generate synthetic transit light curves in order to assess the validity of the chosen parameters and their effect on the light curve.

To demonstrate the impact of every parameter, the output light curve is modeled by varying the values of any specific parameter, the effect of which we are demonstrating, with other parameters (except for the varied one) set to the sample values in Table 4.

The values of orbit eccentricity, exoplanet radius and ring eccentricity were selected as the mean values of their ranges proposed in Table 1 to be more representative for an average case. The value of the semi-major axis was set from its minimum proposed in Table 1, because the effects of orbit rotation are much more evident for less distant orbits. The values of rotation parameters of an orbit and the exoring, the star temperature, $\log(g)$ and the band of the observations were selected pseudo-randomly, representing a typical, non-specific case, ensuring that the transit still occurs and is not central. For

simplicity, the ring semi-major axis and its width were set as a factor of the exoplanet radius. Finally, the ring's specific absorption coefficient and the host star radius were set to their default values from Section 2, with exoplanet mass being roughly equal to the mass of Jupiter.

Table 4. Default parameter values for building synthetic light curves.

Parameter	Value
Exoplanet semi-major axis (A)	0.1 AU
Exoplanet orbit eccentricity (e_p)	0.45
Exoplanet orbit inclination (i)	2°
Exoplanet longitude of ascending node (Ω)	30°
Exoplanet argument of periapsis (ω)	0°
Exoplanet radius (R)	$176{,}000$ km
Exoplanet mass (M)	1.9×10^{27} kg
Ring eccentricity (e)	0.2

Ring semi-major axis (a)	$5R$
Ring width (w)	$\frac{R}{2}$
Ring obliquity (θ)	30°
Ring azimuthal angle (ϕ)	20°
Ring argument of periapsis (ψ)	0°
Ring optical depth (τ)	1.4
Host star radius (R_S)	$700{,}000$ km
Host star temperature (T)	$5{,}500$ K
Host star logarithm of surface gravity ($\log(g)$)	3.0
Observation band	u
Pixel size (px)	$10{,}000$ km

4.1.1. Exoplanet parameters

The semi-major axis of an exoplanet's orbit is critical in the geometry of a transit. Apart from affecting the period of the exoplanet, it determines the **impact parameter** (the projected distance between the center of the star and the center of the planet's path). For an edge-on orbit ($i = 0^\circ$ or $\Omega = 90^\circ$), the semi-major axis does not affect the shape or the depth of the transit. For any other positions, the semi-major axis seriously affects the impact parameter. A larger semi-major axis indicates that the planet's orbit is more distant from the host star, increasing the probability of its path being projected far from the center of the star, often resulting in no transit occurring.

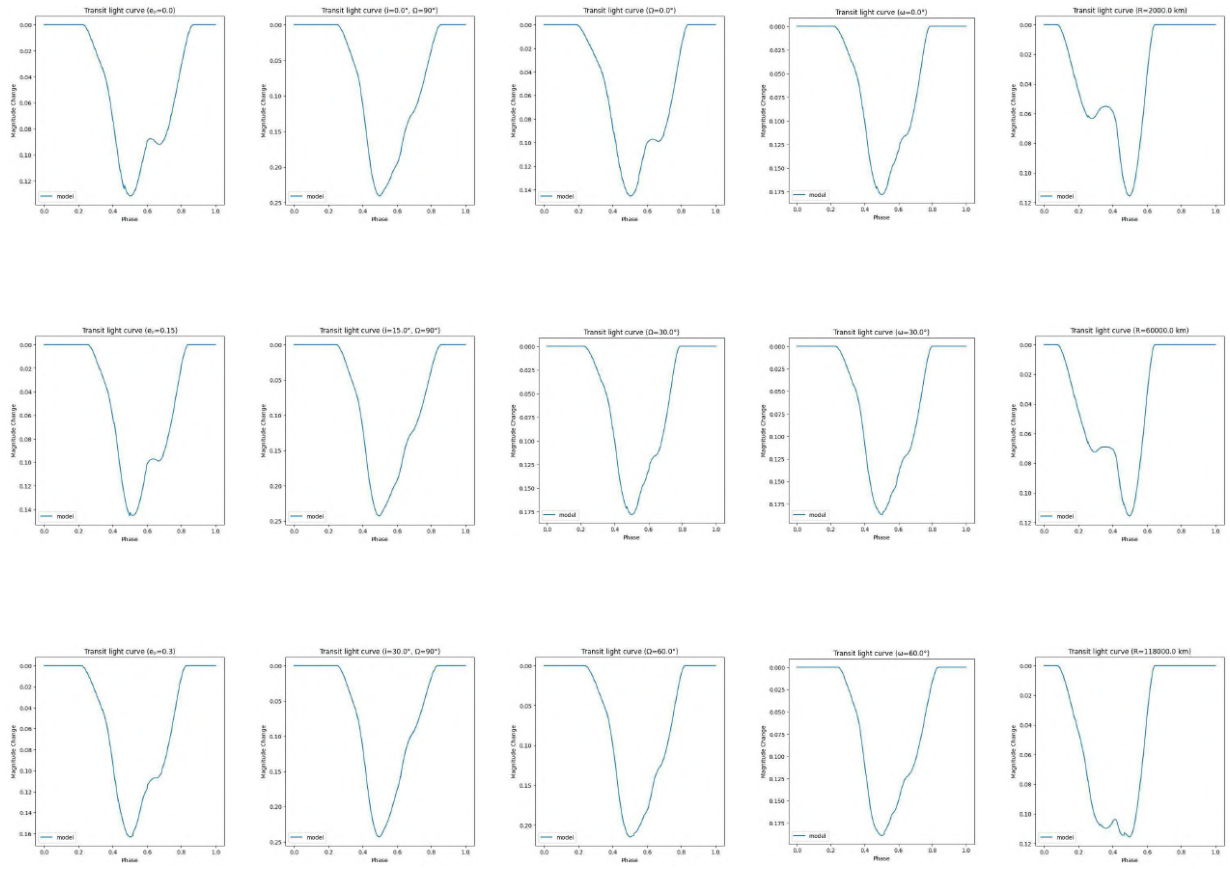

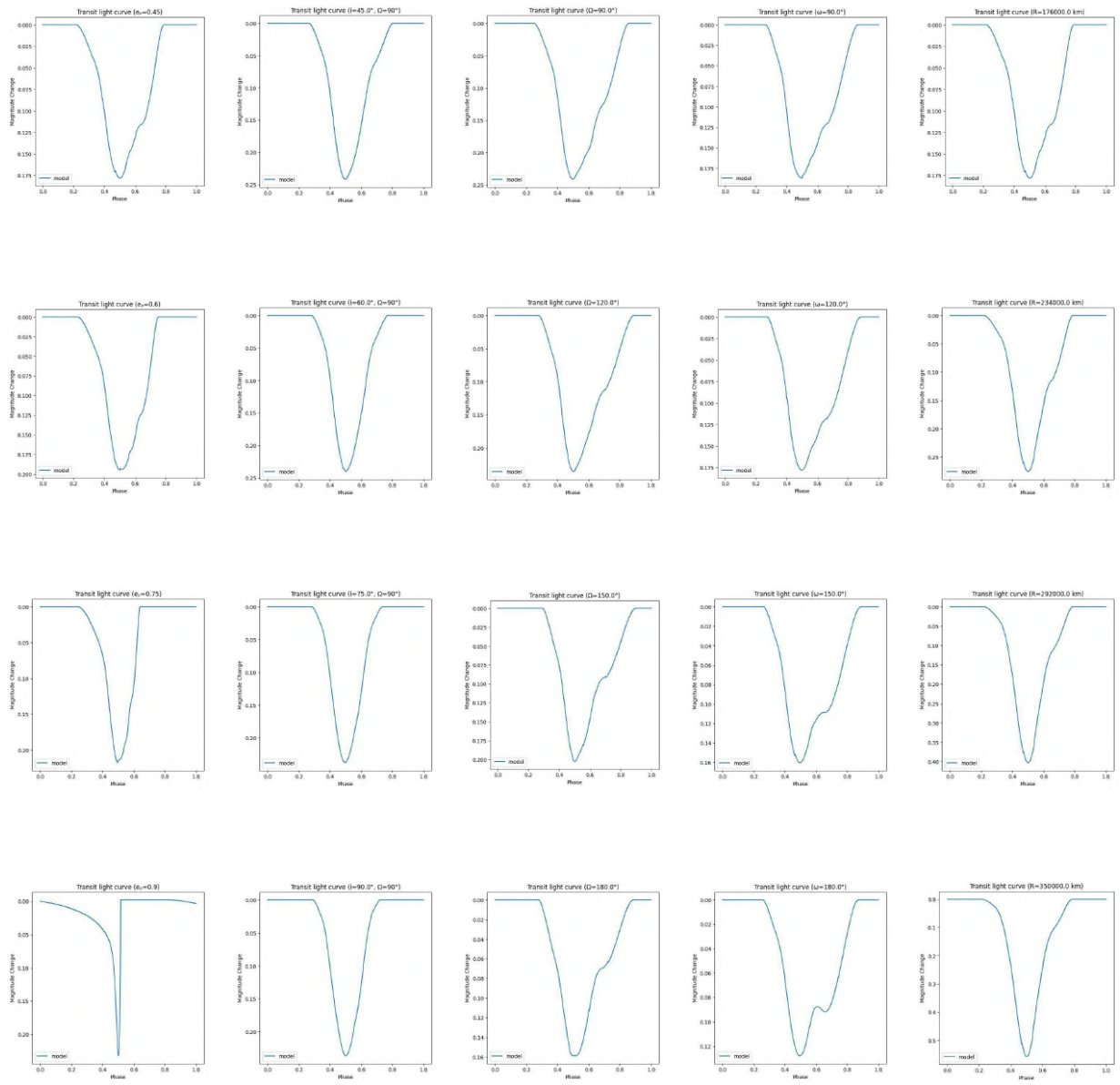

Figure 6. Output transit light curves of the model for different values of exoplanet parameters. For every table column, the varied parameter is specified in the graph title along with its unique value for the specific row. *When the orbit inclination is varied, its longitude of the ascending node is set to* 90°. The other - non-varied or non-specified parameters for the column - are set to their default values from Table 4. The series of transit light curves shows that each of the orbital parameters,

excluding orbital inclination in the case of an edge-on orbit, has a significant impact on both the asymmetries and the depth of the ringed exoplanet transits. Therefore, it is as important to account for the exoplanetary orbital properties as it is for the ring parameters, as dismissing orbital parameters of the exoplanet may lead to false ring positives.

Another crucial determinant of the transit light curve is the planet's radius (see the fifth column in Figure 6). The **transit depth** (fractional decrease in the star's visible brightness at the minimum point of the light curve) caused by the planet alone is proportional to $(R/R_S)^2$. For instance, a larger planet will block a greater fraction of the star's light, leading to a deeper dip in the light curve. Another important consideration is the relation of the projected areas covered by the planet and by its rings. A planet with a smaller radius and bigger rings would provide a differently-shaped light curve and its features would then be mainly determined by the rings, resulting in two distinctive minima from two different sides of the rings passing in front of the star. Transits for ringed exoplanets with bigger radii look much more like regular transit curves, where features from the rings are less distinctive. It is again highly important to note that the radii inferred through fitting without rings may be misleading, as the effect on the transit depth from the ring is attributed to the planet instead, resulting in higher radius estimates. Moreover, without finding distinguishable ring features in the light curve, it is not possible to deduce whether the ring exists or not. This issue leads many researchers to the hypothesis of attributing the low inferred densities of super-puff exoplanets to the effects of a ring system (e.g., Piro & Vissapragada, 2020; Lu et al., 2025).

The orbital eccentricity of an exoplanet has a major impact on both the shape of the light curve and the transit depth. An elongated orbit can cause the planet's speed to vary significantly throughout the orbit, being fastest at periapsis and slowest at apoapsis. This alternation in speed affects the duration of the transit and the shape of the light curve, especially the ingress and egress phases (the start and end of the transit). Thus, on highly eccentric orbits, the planet may move faster or more slowly during the transit stage, affecting the observed transit duration. The orbit eccentricity also affects the impact parameter, which also plays a role in determining the transit depth. See these effects in the first column of Figure 6.

Rotation parameters of the exoplanet orbit play a vital role for orbits with smaller semi-major axes and define the projected trajectory of the planet as a whole. It can take many different shapes from the viewer's perspective, not only straight lines. For that reason, these parameters must be essentially included when modeling transits for closer orbits. They also define how well the ring features, atypical to regular transits, are noticeable (see columns 2, 3 and 4 of Figure 6). Even the argument of periapsis has a significant impact on both the transit depth and the shape of the graph. Our results for it (see column 4 of Figure 6) suggest that it must be addressed in future research on the detection of ringed exoplanets, although it is disregarded in the majority of papers (e.g., Heising et al., 2015; Lu et al., 2025; Piro & Vissapragada, 2020; Aizawa et al., 2017; Barnes & Fortney, 2004). However, for larger orbits, they can vary in very small boundaries, as, in this case, the impact parameter changes drastically with minor fluctuations of orbit inclination and longitude of ascending node. For big semi-major axes, the trajectory of the planet essentially becomes a line as its curvature becomes not visible in smaller parts of the orbit, so the orbit must be almost edge-on: $i \approx 0^\circ$ or $\Omega \approx 90^\circ$. For that reason, for larger orbits, it is recommended to replace orbit rotation parameters with the impact parameter, which would both allow more precision and faster calculations.

4.1.2. Ring parameters

As the optical depth of the ring is enhanced by the factor of $\sec \eta$, where η is the angle between the ring's normal axis and the line of sight, in the cases for rings that are close to being edge-on, the ring gets significantly optically thicker, so it is possible to assume that it is fully opaque, as other papers suggest (e.g., Heising et al., 2015). However, for other cases, it is necessary to account for ring transparency, especially when the ring is close to face-on. In our demonstration (see column 1 of Figure 7), we compare the light curves with optically thin rings, letting through more than 50% of the star's light (first to third pictures in the column), with optically thick rings that let through less than 50% of the star's light (the remaining pictures) for the face-on case. It is evident how significant the effect is: it strongly affects the shape of the curve and makes a major difference in the magnitude change (about 0.055^m). However, if the ring is rotated away (e. g., 80° from the observer), the viewing angle would make a difference. The ring that previously let through 74% of light (the second image in the column) would now let through only about 18% of light.

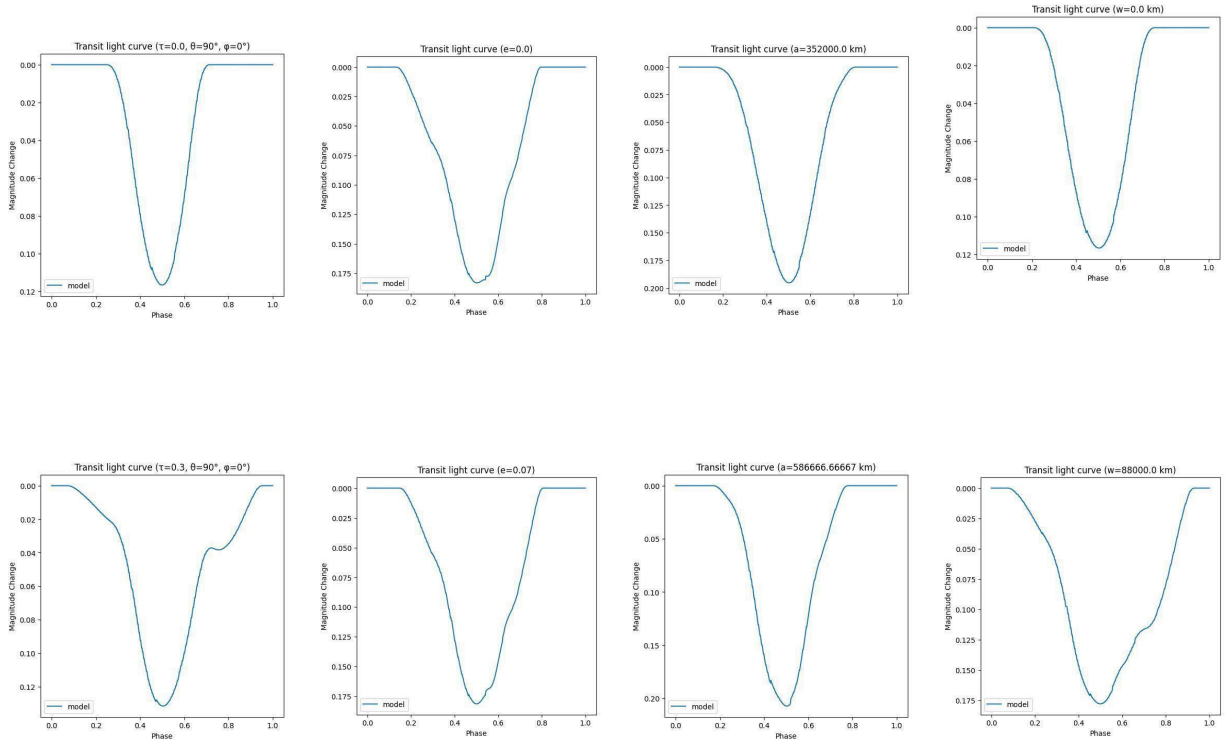

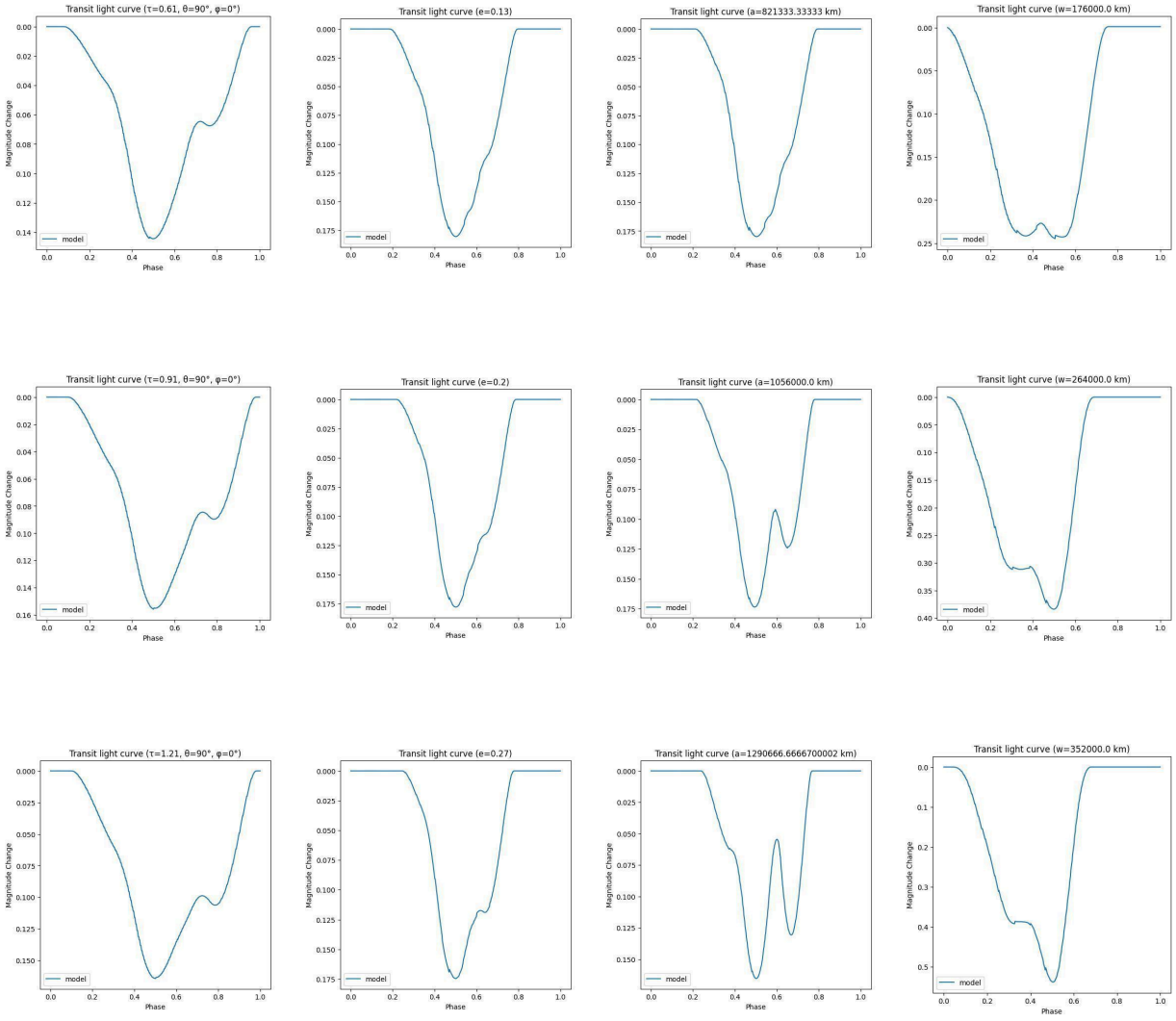
Transit light curve (τ=0.61, θ=90°, φ=0°)
Transit light curve (e=0.13)
Transit light curve (a=821333.33333 km)
Transit light curve (w=176000.0 km)
Transit light curve (τ=0.91, θ=90°, φ=0°)
Transit light curve (e=0.2)
Transit light curve (a=1056000.0 km)
Transit light curve (w=264000.0 km)
Transit light curve (τ=1.21, θ=90°, φ=0°)
Transit light curve (e=0.27)
Transit light curve (a=1290666.6666700002 km)
Transit light curve (w=352000.0 km)
Magnitude Change
Phase
model

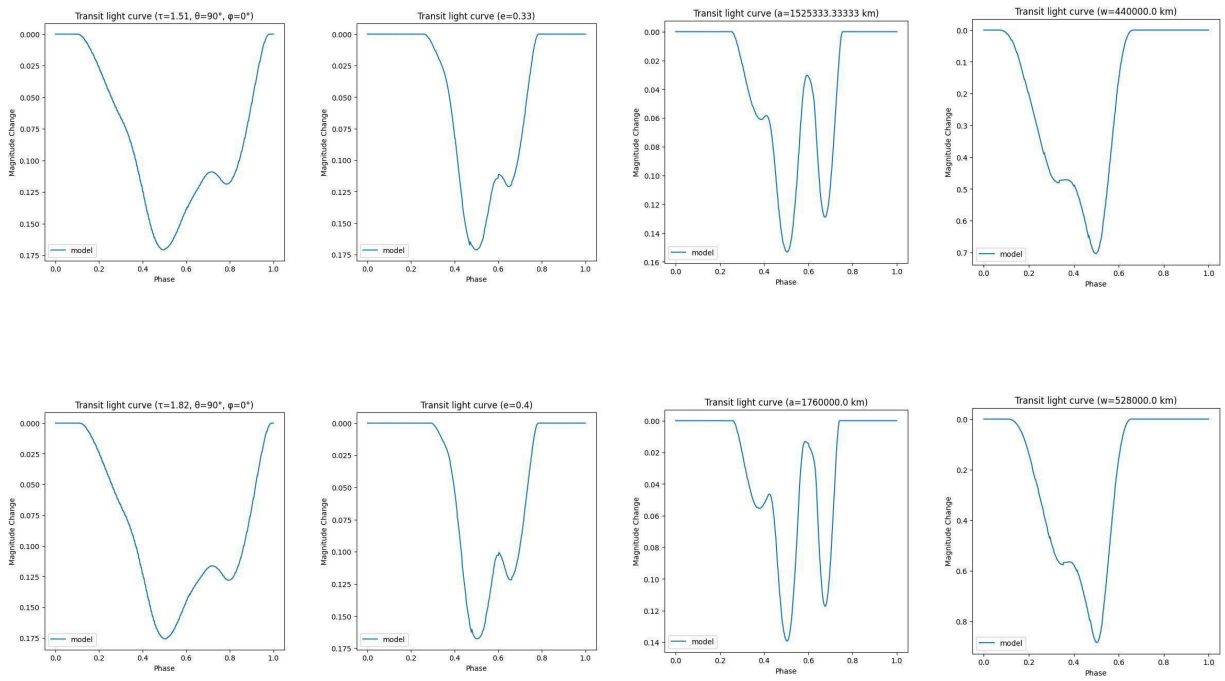

Figure 7. Output transit light curves of the model for different values of ring parameters. For every table column, the varied parameter is specified in the graph title along with its unique value for the specific row. *When the ring optical depth is varied, its obliquity is set to* 90° and azimuthal angle is set to 0°. The other - non-varied or non-specified parameters for the column - are set to their default values from Table 4. The series of synthetic graphs shows that larger and more opaque rings leave stronger signatures on the transit light curves.

To support the analysis of the impact of latter parameters on the transit depth, here we derive the projected area covered by wings:

$S_0 = \pi a_0 b_0 = \pi a_0^2 \sqrt{1 - e_0^2}$ - area of an ellipse with semi-major axis a_0, semi-minor axis b_0 and eccentricity e_0.

The area of the rings is defined as the difference between the areas of its outer and inner ellipses (see Section 2.4):

$$S = \pi \left(a + \frac{w}{2}\right)^2 \sqrt{1 - e^2} - \pi \left(a - \frac{w}{2}\right)^2 \sqrt{1 - e^2} = 2\pi a w \sqrt{1 - e^2}$$

From that, the **projected area** (the effective area that affects the transit depth) is:

$$S_{\text{proj}} = 2\pi a w \cos(\eta)\sqrt{1-e^2} \tag{4.1}$$

The ring eccentricity affects the light curve slightly compared to the previous parameters. Nevertheless, its effect on the shape of the light curve is still evident. When the eccentricity increases, the features of the ring become more noticeable: due to the ring's eccentricity, its shape gets less symmetrical from the focus point, where the exoplanet lies, leading to asymmetries during ingress and egress stages (see column 2 of Figure 7). The effect of the ring's eccentricity is by a factor of $\sqrt{1-e^2}$ (see Equation 4.1), so its effect on the transit depth is almost negligible (especially, knowing that the model looks for eccentricities $e < 0.4$). That is why the magnitude change slightly climbs as the eccentricity rises (see column 2 of Figure 7). For that reason, it is highly possible that the nested sampling simulation might not be able to predict the best eccentricity value with good sampling results for fitting the real data, as the current instrumentation precision is very limited, and noticing such minor effects requires higher-precision data.

From Equation 4.1, it is evident that the ring's semi-major axis and width play almost the same role in defining the transit depth (see the third and fourth columns of Figure 7). In terms of their impact on the shape of the transit light curve, both of them define how well visible the ring features are, with rings leaving a deeper trace when these parameters have higher values (see the third and fourth columns of Figure 7). Sometimes, the transit depth caused by the ring might get dominant, leading to a wider, longer transit duration. This often leads to two distinct minima in the curve, each for a different ring half - they may be asymmetrical if the ring is eccentric (see the fourth column of Figure 7). The semi-major axis can also define if the ring of the exoplanet is more distant from it than the radius of the star (e.g., the radius of Saturn's E ring (Juhász & Horányi, 2002) can be quite close to the Solar radius). If this happens, the light curve would have three extremes: two from the ring on each side of the planet and one from the planet itself (see the third column of Figure 7).

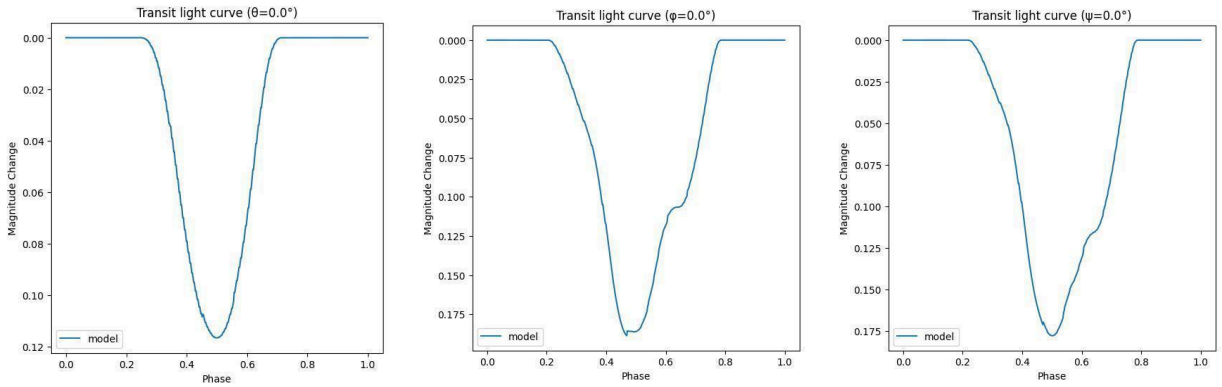

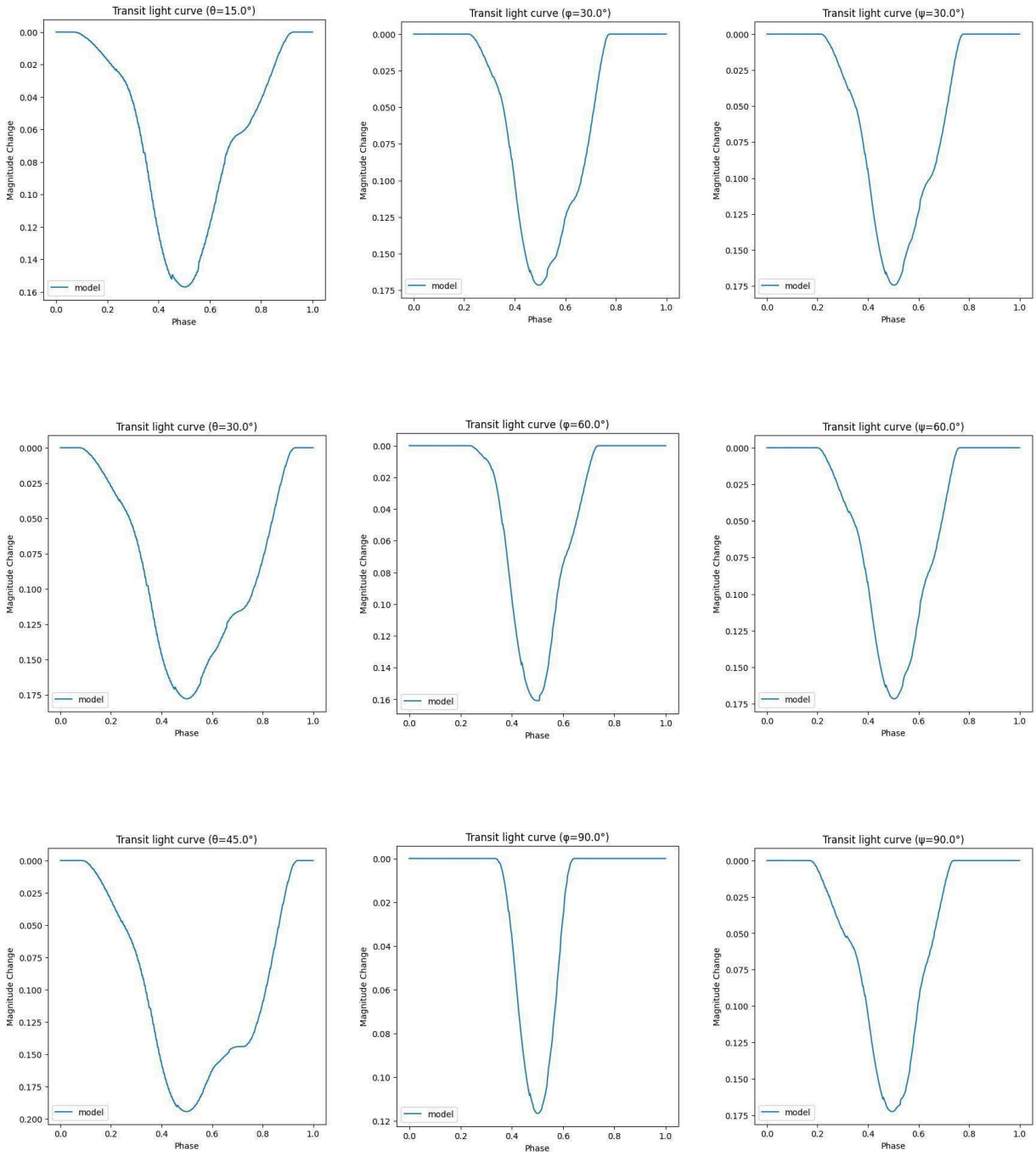
Transit light curve (θ=15.0°)
Transit light curve (φ=30.0°)
Transit light curve (ψ=30.0°)
Transit light curve (θ=30.0°)
Transit light curve (φ=60.0°)
Transit light curve (ψ=60.0°)
Transit light curve (θ=45.0°)
Transit light curve (φ=90.0°)
Transit light curve (ψ=90.0°)
Magnitude Change
Phase
model

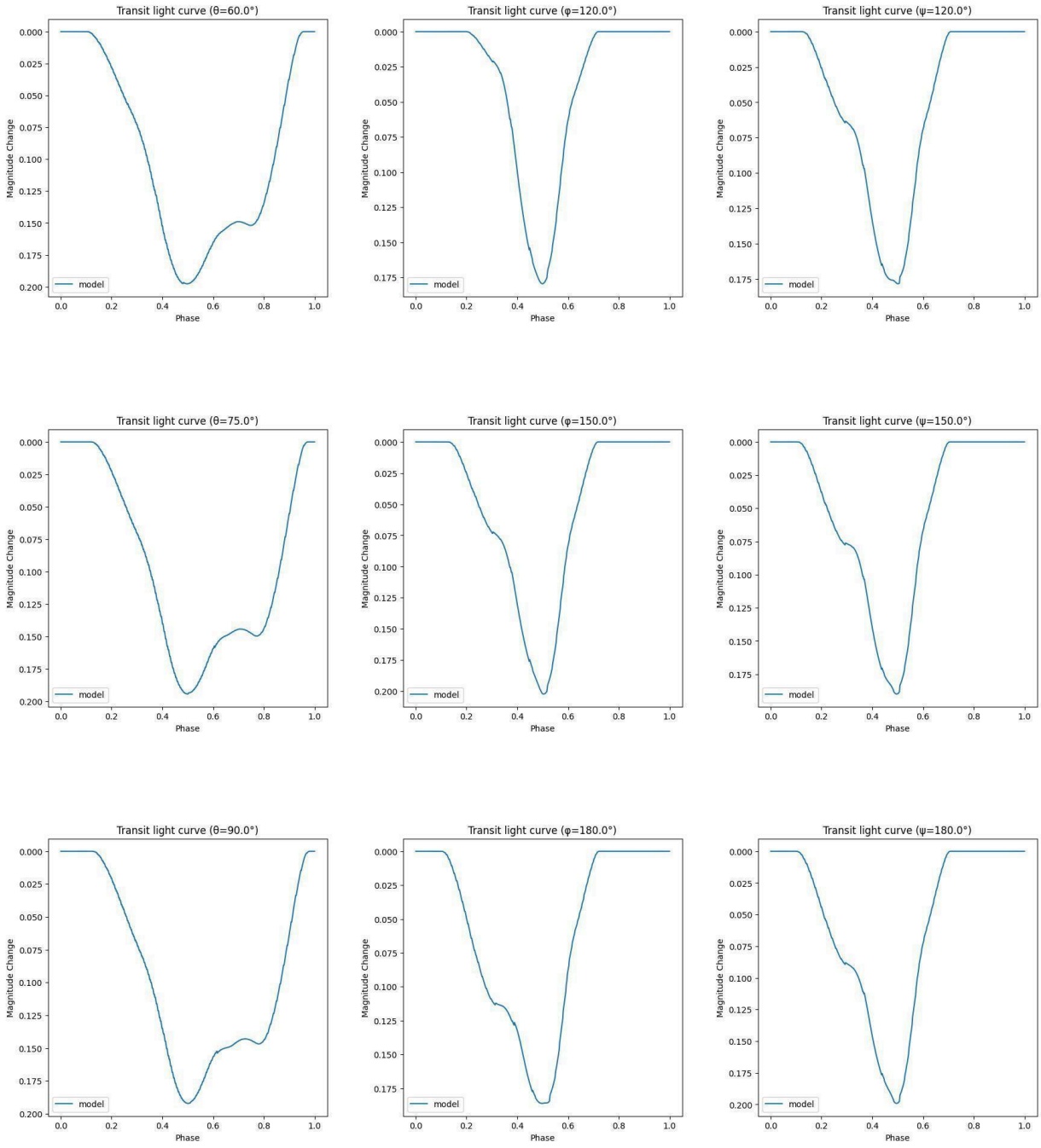
Transit light curve (θ=60.0°)
Transit light curve (φ=120.0°)
Transit light curve (ψ=120.0°)
Transit light curve (θ=75.0°)
Transit light curve (φ=150.0°)
Transit light curve (ψ=150.0°)
Transit light curve (θ=90.0°)
Transit light curve (φ=180.0°)
Transit light curve (ψ=180.0°)
Magnitude Change
Phase
model

Figure 8. Output transit light curves of the model for different values of ring rotation parameters. For every table column, the varied parameter is specified in the graph title along with its unique value for the specific row. The other (non-varied) parameters for the column are set to their default values from Table 4. The series of graphs proves that the ring's orientational properties leave unique asymmetries on the transit light curve.

Apart from defining the angle η and, thus, influencing the optical depth of the ring and the transit depth (see Equation 4.1), the obliquity and the azimuthal angle of the ring strongly influence the light curves (see Figure 8). These parameters make graphs even more asymmetric by improving the effect of ring eccentricity on the ingress and egress stages, which is key for distinguishing a transit of a regular planet from the transit of a ringed planet. The argument of periapsis does not influence the angle η, so it does not affect the ring transparency or the transit depth. However, by rotating the ring in its own plane and moving its apoapsis and periapsis points, this parameter determines at which moment of the transit the effect of the ring's ellipticity would be the most evident.

4.1.3. Star parameters

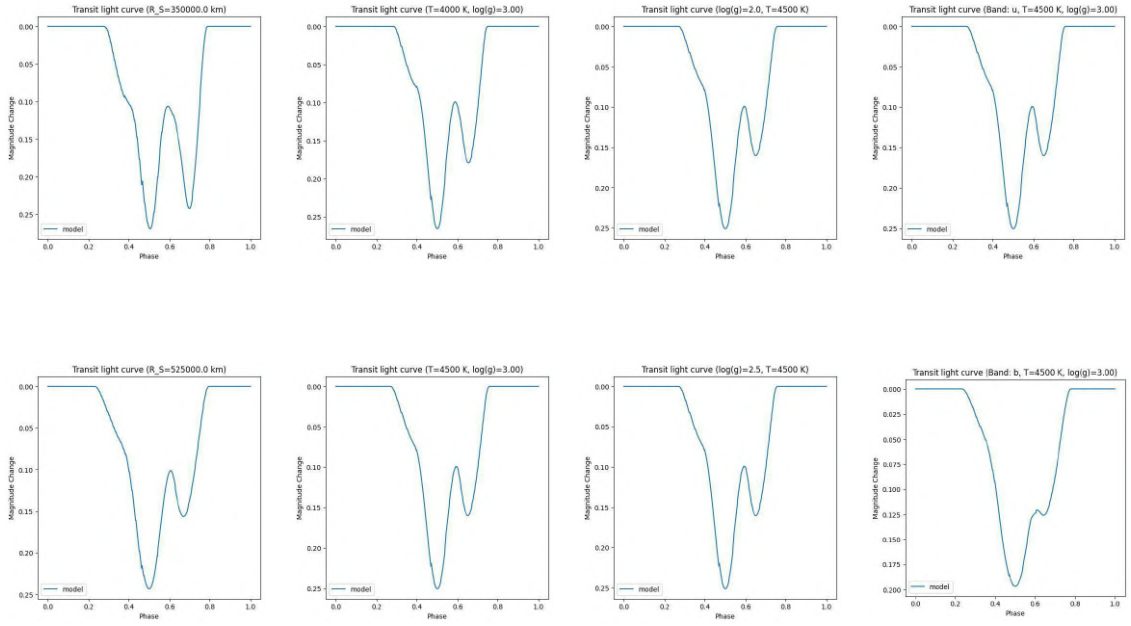

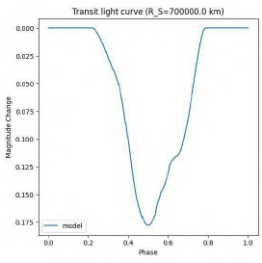
Transit light curve (R_S=700000.0 km)
Magnitude Change
Phase
model

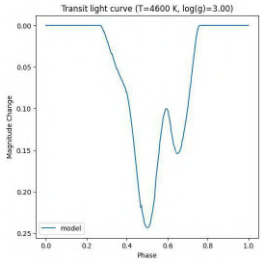
Transit light curve (T=4600 K, log(g)=3.00)
Magnitude Change
Phase
model

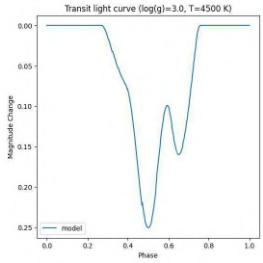
Transit light curve (log(g)=3.0, T=4500 K)
Magnitude Change
Phase
model

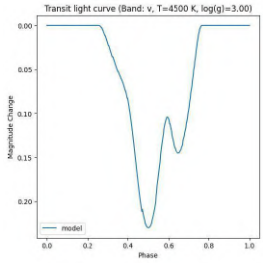
Transit light curve (Band: v, T=4500 K, log(g)=3.00)
Magnitude Change
Phase
model

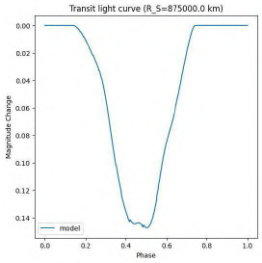
Transit light curve (R_S=875000.0 km)
Magnitude Change
Phase
model

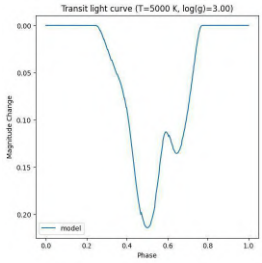
Transit light curve (T=5000 K, log(g)=3.00)
Magnitude Change
Phase
model

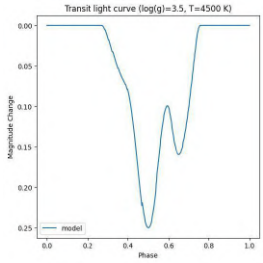
Transit light curve (log(g)=3.5, T=4500 K)
Magnitude Change
Phase
model

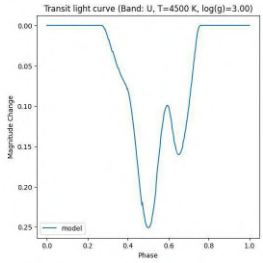
Transit light curve (Band: U, T=4500 K, log(g)=3.00)
Magnitude Change
Phase
model

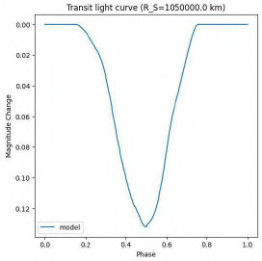
Transit light curve (R_S=1050000.0 km)
Magnitude Change
Phase
model

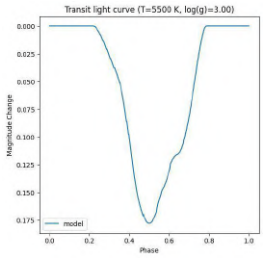
Transit light curve (T=5500 K, log(g)=3.00)
Magnitude Change
Phase
model

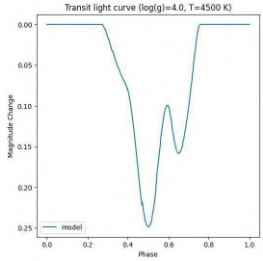
Transit light curve (log(g)=4.0, T=4500 K)
Magnitude Change
Phase
model

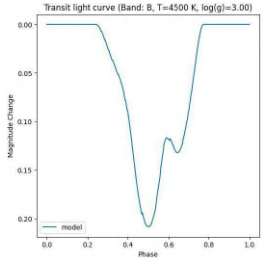
Transit light curve (Band: B, T=4500 K, log(g)=3.00)
Magnitude Change
Phase
model

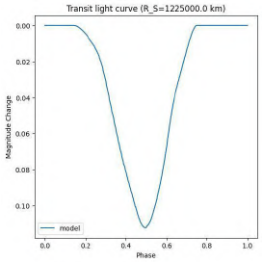
Transit light curve (R_S=1225000.0 km)
Magnitude Change
Phase
model

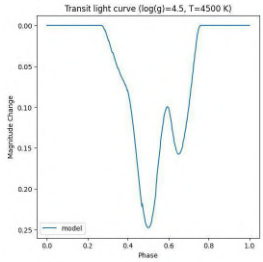
Transit light curve (log(g)=4.5, T=4500 K)
Magnitude Change
Phase
model

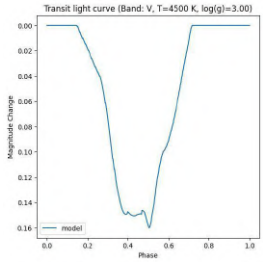
Transit light curve (Band: V, T=4500 K, log(g)=3.00)
Magnitude Change
Phase
model

Figure 9. Output transit light curves of the model for different values of star parameters. For every table column, the varied parameter is specified in the graph title along with its unique value for the specific row. *When the star* $\log(g)$ *or the observation band is varied, the stellar surface temperature is set to* $4{,}500\ \mathrm{K}$. The other - non-varied or non-specified parameters for the column - are set to their default values from Table 4. The graph series shows that the stellar radius determines the transit depth, and with increasing stellar radius, the ring signature becomes less evident until it ultimately becomes undetectable.

The stellar radius is a parameter that is truly determinant for the transit light curve. Its effect on the light curve looks like the reversed impact of exoplanet radius, ring semi-major axis or width. Increasing the host star radius decreases the transit depth, making the ring system more challenging to detect. When the radius gets lower than the value of the ring's semi-major axis, the shape of the transit drastically changes as two or three minima occur, caused by the two sides of the ring and the planet itself moving in front of the star. Stellar surface temperature $\log(g)$ and the observational band also contribute to the transit light curve shape and transit depth, which is attributed to their effect on the stellar limb-darkening.

Star temperature, logarithm of gravitational acceleration and observation band (or wavelength) define the limb-darkening model of the star, providing the quadratic (or square root) limb-darkening coefficients from theoretical tables. The effect of star temperature on the light curve is almost negligible, as it nearly maintains its shape and transit depth for temperature values of 3,500 K; 4,500 K and 4,600 K (see the second column of Figure 9). Nevertheless, for hotter stars (5,000 K and 5,500 K), the transit depth starts decreasing with temperature growing, and the effect of the rings becomes less noticeable (see the second column of Figure 9). The effect of $\log(g)$ on the light curve itself (because of limb-darkening) is negligible, as this parameter has a weak impact on both the shape of the curve and transit depth (see the second column of Figure 9). However, it is still very important to select more physically plausible values of $\log(g)$, as it is later used to calculate the mass of the star, the semi-major axis of the planet and the planet's speed throughout its orbit. The most important thing to consider for modeling the limb-darkening is the band of the observations. Depending on it, the light curve shape and the magnitude change can significantly vary (see the fourth column of Figure 9). Note that these results for limb-darkening effects were provided by the quadratic model (Díaz-Cordovés & Giménez, 1992).

4.2. Model application on real observational data for HIP 41378f

The results of the nested sampling analysis for the super-puff planet HIP 41378f suggest that the planet indeed has a ring system that is almost edge-on, immense, eccentric and partially transparent.

According to its default stopping function, the nested sampling has converged fully after $N_{\mathrm{call}} = 39{,}597$ calls of the main model, providing the maximum log-likelihood of $\ell = 12{,}866.89$ (most favorable scenario, see Section 3.3) and

log-evidence of $\ln Z = 12{,}801.47 \pm 0.25$ (a global measure of a fit model that accounts for both the quality of the light curve fit and the complexity of the parameter space generated by this model).

The best fit curve suggests that it has the following parameter values (see Table 5 and Figure 10). See Figure 11 to view the 2D making matrix of the exoplanet and its ring (see Section 2 for more details on that).

The **shrinkage** values (defined from 0 to 1) in Table 5 represent the degree to which the experimental data have constrained the model parameters relative to our initial assumptions (Section 3.2). High shrinkage values (closer to 1) indicate that the posterior distribution is driven more by the observational data than by the priors, effectively measuring the 'information gain' provided by the transit light curve. As non-informative priors were initially selected, low shrinkage values can indicate major issues in parameter space exploration, suggesting that the number of nested sampling iterations or the number of live points is insufficient.

In this work, shrinkage $\mathcal{S}$ (Savic & Karlsson, 2009) was calculated as:

$$\mathcal{S} = 1 - \frac{\sigma_{\text{post}}}{\sigma_{\text{prior}}}, \tag{4.2}$$

where σ_{post} is the standard deviation of the posterior distribution and σ_{prior} is the standard deviation of the prior distribution.

Table 5. Values of ring and exoplanet properties from the nested sampling simulation. The values themselves represent the median points of the posterior distributions for each parameter, and the upper and lower error limits of the parameter values represent 1σ confidence intervals.

Parameter name	Estimated value	Shrinkage
Exoplanet orbit eccentricity (e_p)	0.003	0.9983
Exoplanet orbit inclination (i)	$84.6^{+0.1^\circ}_{-0.3}$	0.9865
Exoplanet longitude of ascending node (Ω)	90°	0.4303

Exoplanet argument of periapsis (ω)	$0.78^{+0.03^\circ}_{-0.03}$	0.9991
Exoplanet radius (R)	$46{,}200^{+1{,}300}_{-900}$ km	0.8999
Ring eccentricity (e)	$0.418^{+0.002}_{-0.002}$	0.9884
Ring semi-major axis (a)	$2{,}698{,}000^{+4{,}000}_{-4{,}000}$ km	0.9946
Ring width (w)	$374{,}000^{+3{,}000}_{-3{,}000}$ km	0.9964
Ring obliquity (θ)	$0.969^{+0.003^\circ}_{-0.006}$	0.9997
Ring azimuthal angle (ϕ)	$56.45^{+0.21^\circ}_{-0.27}$	0.9931
Ring argument of periapsis (ψ)	$42.7^{+1.3^\circ}_{-1.4}$	0.9614

The optical depth of the ring is derived from output parameters using Equations 2.3.2 and 2.3.3, and enhanced by $\sec\eta = 107 \pm 1$ (Section 2.4), suggesting that the ring absorbs about 45% the light from the star going through it:

$$\tau = \frac{3\kappa M \sec\eta}{1.6a^3(1+e)^3} = 0.593^{+0.012}_{-0.011} \tag{4.3}$$

This result was calculated for the maximum possible ring density ρ_{Roche}, which means that for lower density values, the ring would have let through even more light, even though it lies in an almost edge-on configuration. This finding highlights the role of the $\sec\eta$ factor and the importance of accounting for ring transparency in general in future research, as it has been neglected in several recent papers (e.g., Heising et al., 2015; Piro & Vissapragada, 2020; Lu et al., 2025).

The inferred optical depth values of $\tau = 0.006$ (face-on) and $\tau = 0.593$ (edge-on) are physically reasonable, falling into the category of tenuous, dusty rings similar to those around ice giants. The face-on optical depth of $\tau = 0.006$ is very similar to that of Neptune's Le Verrier ring ($\tau \approx 0.006$, Tiscareno & Murray, 2018) and is significantly more substantial than that of Saturn's diffuse rings G and E ($\tau \approx 10^{-6}$, Cuzzi et al., 2018). The dramatic increase in the edge-on optical depth occurs as the line of sight passes through more ring particles when the ring is edge-on. The rings that are so faint can be detected only thanks to this effect. This combination of parameters is consistent with a ring composed primarily of micron-sized dust that could form thanks to the debris from the collisions of tiny space rocks and nearby moons (e.g., this applies to Saturn's E ring, Hedman et al., 2011).

The **corner plot** provided by the nested sampling analysis (see Figure 10) demonstrates that most parameters are well-constrained. While some parameters like orbital and ring eccentricities and arguments of periapsis, ring semi-major axis, and ring width are distributed almost normally, other parameters exhibit more complex structures. The orbit inclination and the argument of periapsis, for example, display a bimodal distribution, with a secondary peak at a lower value than the best fit. This feature is related to the degeneracy between these two parameters and highlights that there are two distinct scenarios that result in the same impact parameter value (see more on that in Section 4.4.4). The exoplanet radius is notably left-skewed, suggesting that while the data strongly favors a specific size, there is a probability tail toward smaller radii that are compensated for by adjustments in ring parameters that affect the transit depth. Conversely, ring obliquity and azimuthal angle are right-skewed. This asymmetry indicates that the model is more certain about the maximum inclination required to produce the observed dip but allows for a broader range of edge-on configurations that still fit the light curve's shape, which is also supported by our findings in Section 4.4.4.

Despite possible degeneracies (Section 4.4.4), the estimated values lead to a highly accurate best-fit light curve (see Figure 13). The best-fit model, which accounts for rings, provides a good representation of the data. This is supported by a high log-likelihood value (calculated using Equation 3.2) of the best-fit model: $\ell = 12{,}866.89$.

Furthermore, a **posterior predictive check** (PPC) was implemented in order to confirm that the nested sampling has converged and found a local log-likelihood maximum (see Figure 12). The posterior predictive check involved plotting the model light curves for 100 random samples for parameters sets within the uncertainty limit of the best-fit parameters (model lightcurves for the points in the parameter space near the local maximum). The tight grouping of the models and the comparison of the best-fit light curve to the average of near-maximum simulations show that the model has indeed converged and found an existing local log-likelihood maximum, successfully narrowing down the possible system configurations and effectively fitting the transit light curve shape in addition to the transit depth.

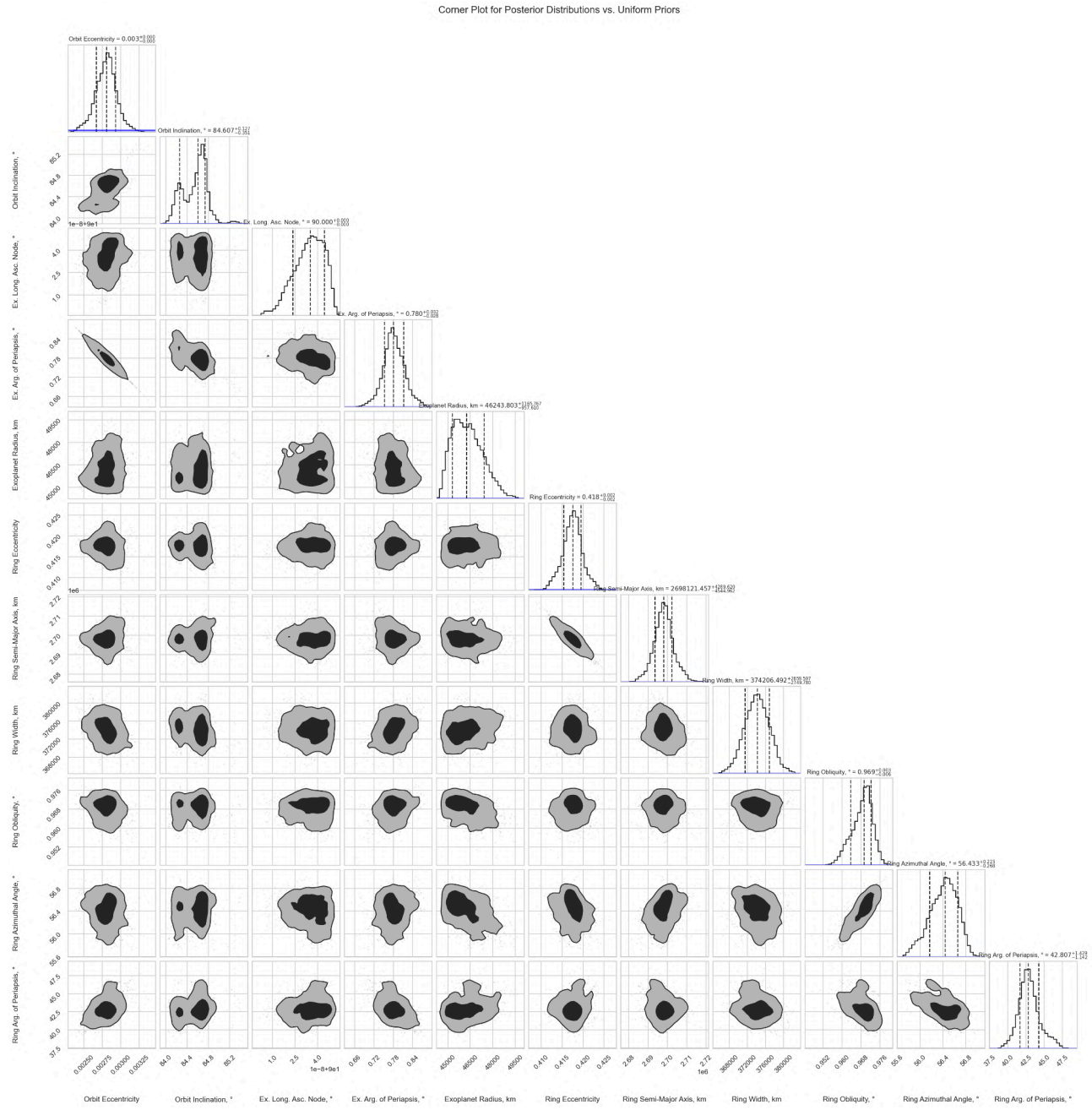

Figure 10. The corner plot generated by our 11-parameter nested sampling analysis with $N_{\text{dim}} = 11$ dimensions and $N_{\text{live}} = 500$ live points that has converged after $N_{\text{call}} = 39{,}597$ function calls. The diagonal panels display the

one-dimensional posterior distributions (black histograms) compared against the uniform prior distributions (horizontal blue lines), illustrating the parameter shrinkage and information gain. The best-fit parameter values and 1σ uncertainties are quoted above each histogram. The off-diagonal panels illustrate the two-dimensional joint probability distributions with contours representing the 1σ, 2σ, and 3σ confidence levels. The prior boundaries are recorded in Table 3. The diagonal panels demonstrate significant parameter shrinkage, which is also numerically evaluated in Table 5, indicating significant information gain constrained by the data regardless of initial broad priors. Although not every posterior distribution is normal (with some even being bimodal), the clearly identified peaks support the hypothesis that HIP 41378f possesses a ring system. Abbreviations: Ex. (Exoplanet), L.A.N. (Longitude of Ascending Node), Arg. Periapsis (Argument of Periapsis), S.-M.A. (Semi-Major Axis), and Az. Ang. (Azimuthal Angle).

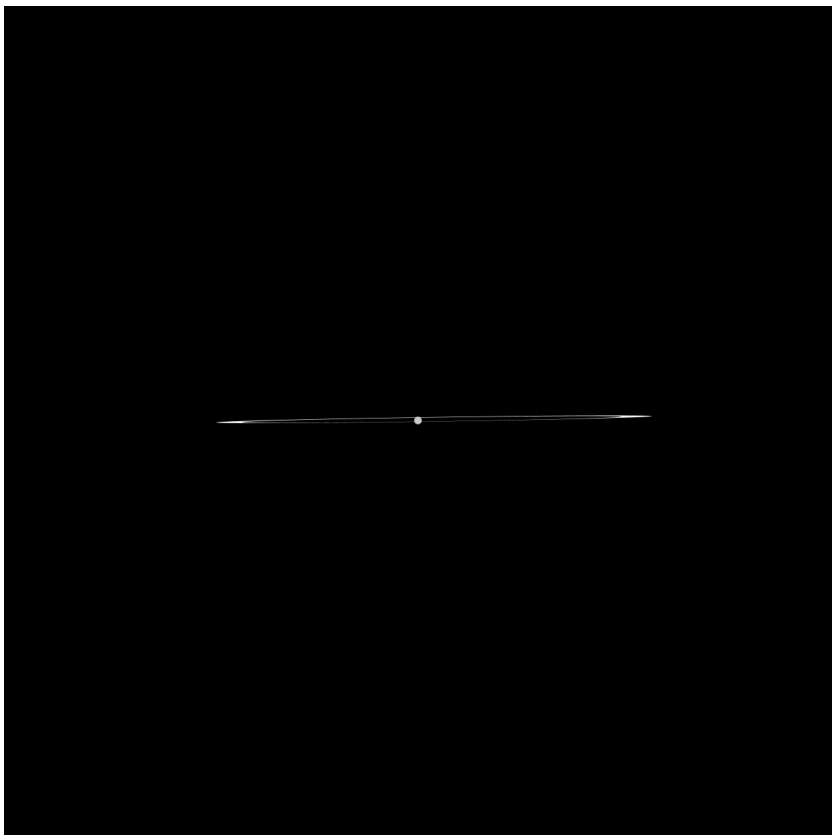

Figure 11. The map of the 2D masking matrix of HIP 41378f and its rings and the projection of the 3D configuration of the ring to the viewed plane produced using the best-fit parameter values identified via nested sampling with $N_{\mathrm{dim}} = 11$, $N_{\mathrm{live}} = 500$ and $N_{\mathrm{call}} = 39{,}597$. Black areas represent pixels with optical depth $\tau = 0$, and the white spots represent pixels with $\tau \to \infty$, with gray color depicting the optical depth of the ring. The results are consistent with a large ring model that has an almost edge-on orientation, which physically resolves the “super-puff” paradox, suggesting that

the density of HIP 41378f was previously overestimated. The figure also confirms that the masking algorithm can accurately represent the rings even in extreme configurations (close to edge-on).

Thus, our results are consistent with an exoring system around HIP 41378f (as greater log-likelihood values represent more accurate fits), also providing the predictions for the properties of this ring system and the new modeling algorithm to use for comparative analysis. It can become a foundational work, leading to further and more in-depth analysis of the HIP 41378f's ring system.

Although the estimated value of the ring semi-major axis ($a = 2{,}698{,}000\ \mathrm{km} \approx 0.018\ \mathrm{AU}$) may seem irrelevantly overestimated if compared to ice and gas giants within the solar system, its value is physically acceptable and even rather conservative in comparison with J1407b, the other popular candidate for exoplanetary rings, with $a = 0.6\ \mathrm{AU}$ (Kenworthy & Mamajek, 2015).

Furthermore, the ring is kept fully inside the exoplanet's Roche limit by the dynamic boundaries of the nested sampling algorithm. This constraint ensures that the resulting ring parameters align with a stable structure that can survive tidal forces, which supports the physical plausibility of our super-puff explanation. The tidal forces from HIP 41378f prevent the ring particles from clumping together to form moons. For the ring to exist inside the Roche limit at such a significant distance from the host planet, it has to sustain low volume-averaged (bulk) density - not exceeding the Roche critical density (Tiscareno et al., 2013), see equation 2.3.3. Thus, it would probably exist as a diffuse cloud of independent dust particles, which is supported by its low inferred face-on optical depth ($\tau = 0.006$) that suggests that the concentration of particles is tenuous. In this configuration, if dust grains are pulled together to form a proto-satellite, they would be torn apart before they can bond due to HIP 41378f tidal forces.

Moreover, the ring system remains dynamically bound to the planet as its aposapsis is well within the planet's **Hill radius** (the distance at which the gravity of HIP 41378f can hold on to the particles despite the pull from the host star). This ensures that the ring particles are gravitationally bound to HIP 41378f rather than being stripped away due to the tidal influence of the host star (Tiscareno, 2013).

As the ring is inferred to be tenuous, it would most probably be almost collisionless due to significant distances between particles. Therefore, **collisional spreading** (expansion of the rings or formation of moons due to particle collisions) would be almost non-existent.

If the estimated ring eccentricity (0.418) is not an artefact of the degeneracy between the ring eccentricity and its semi-major axis (Section 4.4.4), the ring is either newly formed and is going to circularize in thousands or millions of years due to **differential precession** (different precession periods of the inner and the outer parts of the ring that can occur if the planet is even slightly oblate; Schlichting & Chang, 2011) or the **Poynting-Robertson drag** (loss of angular momentum by ring particles due to absorption and re-emission of stellar radiation, Goldreich & Tremaine, 1978; Schlichting & Chang, 2011), or the ring's eccentricity is maintained by undiscovered shepherd moons or gravitational influence of other nearby planets in the HIP 41378 system.

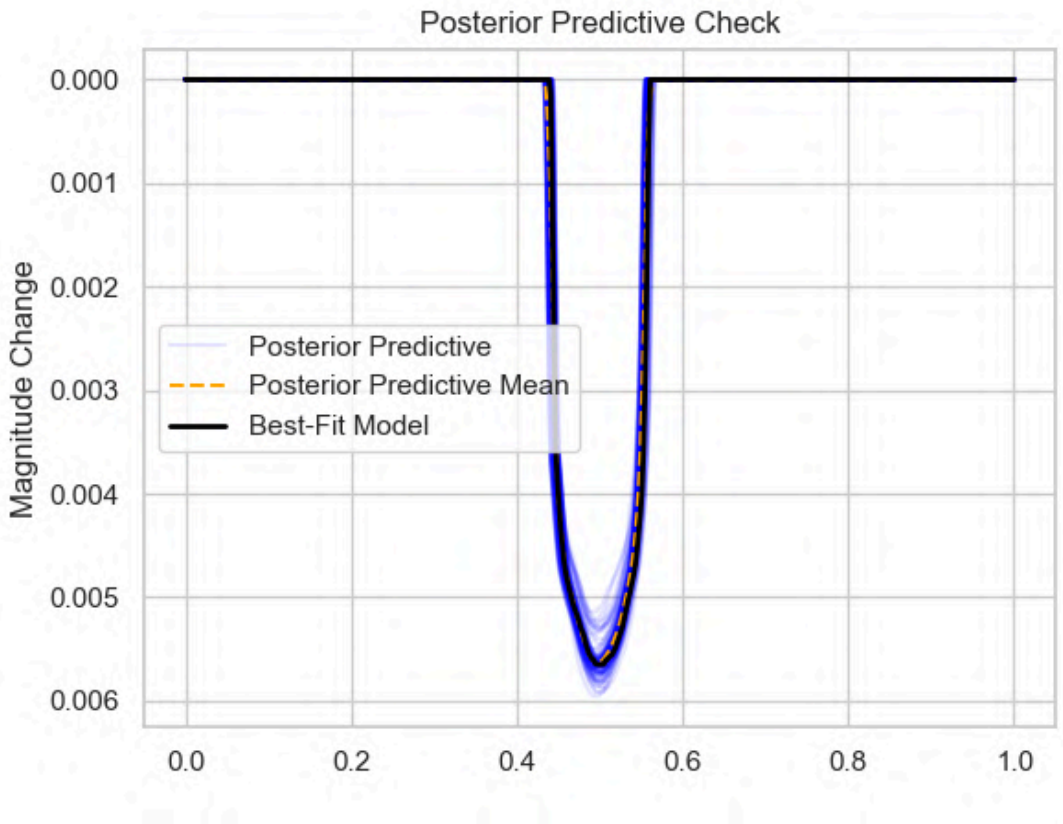

Figure 12. Posterior Predictive Check (PPC) showing the reliability of the ringed exoplanet model. The solid black line represents the best-fit model identified by the nested sampling analysis. The light blue lines represent 100 separate simulations created using random samples within the 2σ confidence interval for each parameter; their narrow spread indicates high confidence in the model. The dashed orange line shows the average of these simulations. The fact that the blue spread of lines tightly follows the black line and the black line almost corresponds with the dashed orange line demonstrates that the nested sampling has converged on a physically consistent solution that accurately reproduces the observed light curve features.

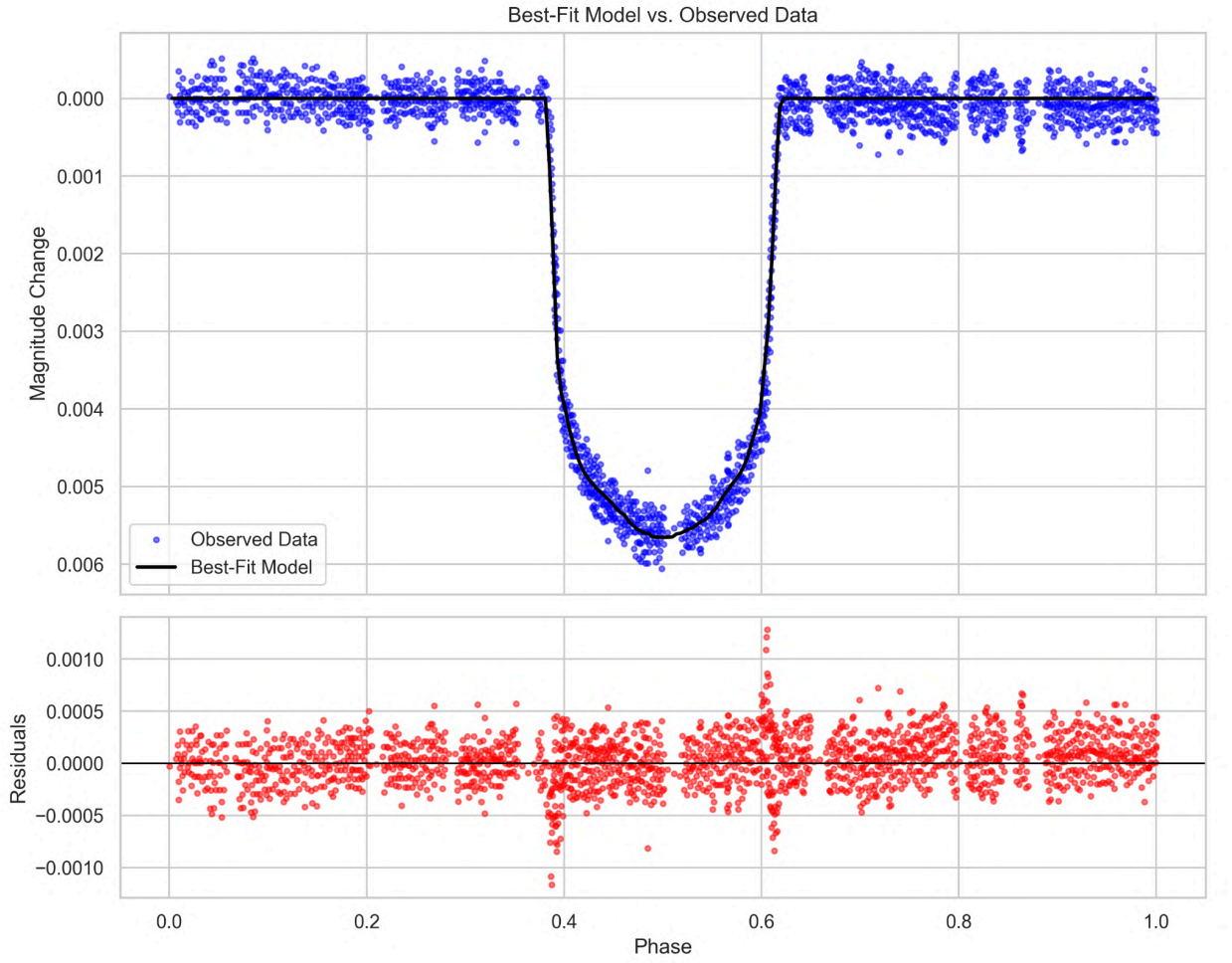

Figure 13. The phase-folded observed light curve from Berardo et al., 2019 (blue data points), fit using our model of the transit by a ringed exoplanet (black line, see Section 2 for the model) according to the best-fit parameter values yielded by the 11-parameter nested sampling algorithm with $N_{\text{live}} = 500$ and $N_{\text{call}} = 39{,}597$. The red data points represent the residuals (the difference between actual and predicted magnitude change values). The fit shows excellent agreement with data, effectively capturing the ingress and egress features and modeling the midtransit as an asymmetric curve that lies perfectly in the middle of the noisy data (see the residuals). The resulting features are unique to the ringed model, which is well-demonstrated by the asymmetrical nature of the fit. The fit suggests that the "super-puff" nature of HIP 41378f can be explained with a ringed exoplanet model, decreasing its inferred bulk density thanks to the additional transit depth generated by the rings. The slightly twisted behavior of the best-fit curve also demonstrates an advantage of the pixel-based modeling algorithm, as analytical models usually create less complicated fits.

As we assume that the rings are made out of silicate grain dust (Table 2), the rings are predicted to be much more resilient to **radiation pressure**, **sputtering** (erosion by stellar wind) and **sublimation** (evaporation due to stellar heat) than ice particles (Juhász & Horányi, 2002). This makes the ring much more durable in high-temperature environments, which suits the location of HIP 41378f ($A = 1.377$ AU, close to its host star) well.

Furthermore, the best-fit simulation with the rings allows us to alleviate the problem of HIP 31478f's inflated radius, giving the bulk density value of:

$$D = \frac{M}{\frac{4}{3}\pi R^3} = 174^{+15}_{-10}\frac{\text{kg}}{\text{m}^3} \tag{4.4}$$

This density value is still much smaller than those in our solar system (about 3.96 times smaller than Saturn's density), suggesting that its bloated atmosphere may be mostly made out of light elements, such as hydrogen and helium. This estimate is much more physically realistic than the previously suggested value of $90\ \text{kg m}^{-3}$ (Santerne et al., 2019).

The inferred $R = 46{,}200$ km places HIP 41378f between Uranus and Saturn in terms of its radius. Due to its low density value, HIP 41378f can be classified as a puffy gas giant, smaller and more lightweight than Saturn. The inferred density value does not allow the exoplanet to be an ice giant, as they are typically composed of heavier materials (e.g., water, ammonia and methane).

Because of the possible degeneracy in the ring's semi-major axis, the resulting value of radius may be approximate. Nevertheless, our results suggest that the "super-puff" phenomenon can be fully or partially explained by the presence of rings for some exoplanets, which supports the hypothesis from Piro & Vissapragada, 2020.

4.3. Alternative explanations for transit asymmetry

To provide statistical confirmation of our ringed exoplanet model, we evaluate the necessity and the complexity of the exoplanetary ring hypothesis by comparing our model to the alternative explanations of the asymmetrical transit shape. While our 11-parameter ring model provides a visually and mathematically suitable fit, it must be weighed against simpler alternative explanations using the **Bayesian evidence** (the likelihood of observed data being represented by a specific model). By calculating the difference in the natural logarithm of the evidence ($\Delta \ln Z$) between our primary model and several competing scenarios, we can quantify the **Bayes factor** (a quantity representing the evidence of one hypothesis over another) to determine if the additional complexity is supported by the data.

The following subsections will detail how alternative models are constructed and fit (Sections 4.3.1-4.3.4), the effects can be modeled for other systems but are irrelevant to HIP 41378f (Sections 4.3.6-4.3.6), and the model comparison results (4.3.7).

4.3.1. Ringless model

Although the HIP 41378f transit data have been already fit multiple times using models that do not include the assumption of it having a ring system (e.g., Vanderburg et al., 2016; Berardo et al., 2019; Grouffal et al., 2022; Grouffal et al., 2025), it is needed

to construct our own fit of the transit light curve to get a value of $\ln Z$ describing the model evidence for the specific sampler and used data.

The transit model is handled similarly to the ringed exoplanet transit model (Section 2) but without creating and applying the ring mask. Thus, it incorporates only 5 parameters to be fit: orbital eccentricity (e_p), inclination (i), longitude of ascending node (Ω), argument of periapsis (ω) and exoplanet radius (R).

Also, the priors are different for the ringless model, as the exoplanet radius can now be greater than one in the ringed exoplanet fit because, without rings, it becomes the only factor affecting the transit depth (Table 6). All model parameters have static boundaries, as the evaluation against the Roche limit for the rings is not needed.

Table 6. Prior distribution boundaries for the parameters of the ringless exoplanetary transit model that are to be fit using the nested sampling algorithm. The boundaries for each ringless model parameter are static. All prior distributions are uniform.

Prior	Boundaries	Rationale
Exoplanet orbit eccentricity (e_p)	0.0 to 0.9	Must not be too close to $e_p = 1$ to avoid huge matrix sizes that can slow down calculations
Exoplanet orbit inclination (i)	0 to 90°	Other values of i and ω would result in configurations that are symmetrical to those already existing and, thus, return similar light curve results. The selected range for Ω ensures geometric transit for a large semi-major axis ($A = 1.377$ AU)
Exoplanet longitude of ascending node (Ω)	$90 - 5 \times 10^{-8^\circ}$ to $90 + 5 \times 10^{-8^\circ}$	
Exoplanet argument of periapsis (ω)	0 to 180°	
Exoplanet radius (R)	$46{,}170$ km to $20R_\oplus$	Must be close to the result from Santerne et al., 2019 and greater than for the ringed exoplanet fit (Section 2)

For this model, the nested sampling algorithm was run with the parameters of $N_{\text{dim}} = 5$ and $N_{\text{live}} = 500$. All other nested sampling settings were set similarly to our run in Section 3.

4.3.2. Oblate planet model

The **oblate planet** (a planet that is not perfectly spherical but is instead flattened at the poles and bulged at the equator due to its rapid rotation) model is handled similarly to the ringless model (Section 4.3.1). However, the masking exoplanet matrix is created differently.

The main quantity describing how oblate a planet is its flattening factor, or **oblateness** (f). It is defined as:

$$f = \frac{R_e - R_p}{R_e}, \tag{4.5}$$

where R_e and R_p are the planet's equatorial and polar radii, respectively.

After the pixel grid of the planet is initialized similarly to Section 2.4 and every matrix is filled with optical depth $\tau(x, y) = 0$, the parameter of the planet's **projection rotation angle** (β) is introduced. It describes the rotation of the oblate planets in the projection plane. When $\beta = 0^\circ$, the projected equator of the planet is parallel to the stellar equator, and when $\beta = 90^\circ$, the projected axis of the planet is parallel to the stellar equator. Hence, the projection rotation is the angle between the stellar equator and the planetary equator projection measured in the projection plane.

Using the projection rotation angle, the centered coordinates are transformed to represent the rotated mask:

$$x_{\text{rot}} = x\cos\beta + y\sin\beta; \; y_{\text{rot}} = y\cos\beta - x\sin\beta, \tag{4.6}$$

where (x, y) are centered coordinates and $(x_{\text{rot}}, y_{\text{rot}})$ are the coordinates in the rotated mask.

Then, the polar radius is calculated from the equatorial radius as:

$$R_p = R_e(1 - f) \tag{4.7}$$

After that, the boundaries of the planet are evaluated, and the optical depth is set to $\tau(x, y) \to \infty$ inside the planet's border using the ellipse equation:

$$\frac{x_{\text{rot}}^2}{R_p^2} + \frac{y_{\text{rot}}^2}{R_e^2} \leq 1, \tag{4.8}$$

The prior distribution bounds are set similarly to those for a ringless fit (Section 4.3.1) with the addition of two new parameters: exoplanet obliquity and projection rotation angle (see Table 7).

Table 7. Prior distribution boundaries for the parameters of the oblate exoplanet transit model that are to be fit using the nested sampling algorithm. The boundaries for each oblate planet model parameter are static. All prior distributions are uniform.

Prior	Boundaries	Rationale
Exoplanet orbit eccentricity (e_p)	0.0 to 0.9	Must not be too close to $e_p = 1$ to avoid huge matrix sizes that can slow down calculations
Exoplanet orbit inclination (i)	0 to $90°$	Other values of i and ω would result in configurations that are symmetrical to those already existing and, thus, return similar light curve results. The selected range for Ω ensures geometric transit for a large semi-major axis ($A = 1.377$ AU)
Exoplanet longitude of ascending node (Ω)	$90 - 5 \times 10^{-8}$ to $90 + 5 \times 10^{-8}$	
Exoplanet argument of periapsis (ω)	0 to $180°$	
Exoplanet equatorial radius (R_e)	$46{,}170$ km to $20R_\oplus$	Must be close to the result from Santerne et al., 2019 and greater than for the ringed exoplanet fit (Section 2)
Exoplanet oblateness (f)	0.0 to 0.9	Must not be too close to $f = 1$ to avoid huge matrix sizes that can slow down calculations
Exoplanet projection rotation angle (β)	0 to $180°$	Other values would result in symmetrical cases, thus, return similar light curve results.

For this model, the nested sampling algorithm was run with the parameters of $N_{\mathrm{dim}} = 5$ and $N_{\mathrm{live}} = 500$. All other nested sampling settings were set similarly to our run in Section 3.

4.3.3. Observational noise model

The model of the instrumental systematics takes the transit light curve directly from the ringless transit model (Section 4.3.1) and applies random noise to it.

For that, the light curve is first converted from magnitude change (Δm) to relative flux (F):

$$F(\Phi) = 10^{-0.4\Delta m(\Phi)} \tag{4.9}$$

To represent noise, the model uses two parameters: **noise scale** (σ_n) and **noise magnitude** (υ). For simplicity, we assume that noise values follow a Gaussian distribution centered on zero with a standard deviation of σ_n. The random noise relative flux values F_n are taken from the normal distribution $N(0, \sigma_n^2)$ are then multiplied by υ, which sets the final noise amplitude:

$$F_n \sim \upsilon N(0, \sigma_n^2) \tag{4.10}$$

Finally, the random noise is added to the relative flux at each data point and the light curve is converted back to magnitude, resulting in the noisy light curve ($\Delta m_n(\Phi)$):

$$\Delta m_n(\Phi) = -2.5 \log(F(\Phi) + F_n(\Phi)) \tag{4.11}$$

To ensure that the model returns identical light curves for the same sets of parameter values, **random seeds** (numbers that initialize the sequence of pseudorandom numbers) are stored for each unique combination of parameters.

Then, for the nested sampling, the boundaries of noise scale and noise magnitude priors are estimated from transit data. For the estimation, the global standard deviation (σ_{global}) in $F(\Phi)$ is first calculated across the full time series for each observational light curve (C5, short cadence C18 and long cadence C18; see the data from specific Campaigns in Figure 5). After that, localized standard deviations are computed for centered windows with 10 samples each. The maximum of the localized standard deviations (σ_{max}) is then found. See the results of this analysis in Table 8. The other prior distribution bounds are set similarly to those for a ringless fit (Section 4.3.1) with the addition of υ and σ_n (see Table 9).

Also, it is important to mention that this model accounts only for random (white) noise. It does not represent any deterministic instrumental effects, such as **cadence smearing** (an effect that arises from integration of received flux over a finite exposure time). However, following the findings from Berardo et al., 2019, modeling cadence smearing is unnecessary, as for short cadence data (1-minute exposure), the effect of smearing was well below the intrinsic scatter of data. While cadence smearing can affect the long cadence (30-minute) data, our model stacks short and long cadence data (Figure 5), the high resolution of the former ensures that the estimated ring properties are not biased by this effect.

Table 8. Summary of photometric noise statistics for the HIP 41378f observation sets. The data in the columns of the table represents the analysis results for K2 Campaign 5, K2 Campaign 18 short cadence observations and K2 Campaign 18 long cadence observations (Vanderburg et al., 2016), respectively. The first data row contains the global standard deviation values for each observed light curve, and the second row contains maximum localized standard deviations for each light curve. This data is used to determine the prior boundaries for nested sampling analysis of the observational noise model in Table 9.

Campaign	C5	C18 short cadence	C18 long cadence
σ_{global}	0.002085	0.002162	0.002298
$\sigma_{\max}$	0.002250	0.002281	0.002363

Table 9. Prior distribution boundaries for the parameters of the observational noise transit model that are to be fit using the nested sampling algorithm. The boundaries for each observational noise model parameter are static. All prior distributions are uniform.

Prior	Boundaries	Rationale
Exoplanet orbit eccentricity (e_p)	0.0 to 0.9	Must not be too close to $e_p = 1$ to avoid huge matrix sizes that can slow down calculations
Exoplanet orbit inclination (i)	0 to 90°	Other values of i and ω would result in configurations that are symmetrical to those already existing and, thus, return similar light curve results. The selected range for Ω ensures geometric transit for a large semi-major axis ($A = 1.377$ AU)
Exoplanet longitude of ascending node (Ω)	$90 - 5 \times 10^{-8}$ to $90 + 5 \times 10^{-8}$	

Exoplanet argument of periapsis (ω)	0 to $180°$	
Exoplanet radius (R)	$46{,}170$ km to $20R_{\oplus}$	Must be close to the result from Santerne et al., 2019 and greater than for the ringed exoplanet fit (Section 2)
Noise scale (σ_n)	0.000000 to 0.007088	The upper boundaries are $3\sigma_{\max}$ and $2\sigma_{\text{global}}$, respectively, where both $\sigma_{\max}$ and σ_{global} are taken from C18 long cadence data, because it has stronger noise overall (see Table 8). This allows noise three times as strong as the noise in the observed data with twice its amplitude.
Noise magnitude (υ)	0.000000 to 0.004595	

4.3.4. Starspot/facula model

To investigate whether the light curve asymmetries could be caused by stellar activity rather than a ring system, we create a dynamic stellar feature model.

The **starspots** (cooler regions of a star with lower brightness than its surface) **/ faculae** (hotter regions of a star with greater brightness than its surface) model is handled similarly to the ringless model (Section 4.3.1). However, the host star matrix is created differently and changes its state over time.

For simplicity, it is assumed that only one starspot/facula is present on the stellar equator so that its axis is perpendicular to the line of sight. Although the rotational period of the star can be orders of magnitude greater than the exoplanetary transit duration, it is necessary to account for the spot dynamics due to limb-darkening effects, as the effect on the light curve shape is minor for both the ring and the starspot/facula hypotheses.

For that reason, the longitude λ_{spot} of the spot/facula on the stellar matrix gets recalculated on every iteration of the starspot/facula as:

$$\lambda_{\text{spot}}(t) = \lambda_0 + \omega_S t, \tag{4.12}$$

where λ_0 is the **initial spot/facula longitude** (the angle from the zero meridian on the star and the spot/facula calculated counter-clockwise, where $90°$ means that the spot/facula is exactly in the center of the stellar disk), ω_S is the stellar angular velocity (that can be positive or negative depending on the rotation direction) and t is the time from the transit start.

The coordinates (x_c, y_c) of the spot/facula center are later computed as:

$$x_c = n + n\cos\lambda;$$
$$y_c = n, \tag{4.13}$$

where n is the matrix size (stellar radius in pixels).

To account for the horizontal compression of the spot/facula projection near stellar limb due to perspective distortion, we use the factor of $|\sin\lambda|$, and the spot/facula is, thus, applied to all pixels matching the following condition, derived from the equation of a circle compressed to an ellipse:

$$\left(\frac{|x - x_c|}{\max(|\sin\lambda_{\text{spot}}|, 0.1)}\right)^2 + (y - y_c)^2 \leq \left(\frac{r_{\text{spot}}}{R_S}\right)^2, \tag{4.14}$$

where r_{spot} is the spot radius and $\max(|\sin\lambda|, 0.1)$ is used to prevent division by zero and ensure that the spot is always visible while it is on the closest hemisphere of the host star.

For the pixels that satisfy this condition, the brightness map $I(x, y)$ is recalculated, using the **spot/facula brightness parameter** B (spot/facula intensity in stellar intensities; 0 stands for completely dark spots, and 2 is used as the maximum for bright faculae):

$$I(x, y) = I(\mu)B, \tag{4.15}$$

where $I(\mu)$ is the normalized intensity profile given by the quadratic limb-darkening model (Section 2.4). The prior stellar grid creation is similar to Section 2.4.

The prior distribution bounds are displayed in Table 10 and set similarly to those for a ringless fit (Section 4.3.1) with the addition of four new parameters: stellar angular velocity (ω_S), initial spot longitude (λ_0), spot radius (r_{spot}) and spot brightness (B).

Table 10. Prior distribution boundaries for the parameters of the observational noise transit model that are to be fit using the nested sampling algorithm. The boundaries for each observational noise model parameter are static. All prior distributions are uniform.

Prior	Boundaries	Rationale
Exoplanet orbit eccentricity (e_p)	0.0 to 0.9	Must not be too close to $e_p = 1$ to avoid huge matrix sizes that can slow down calculations
Exoplanet orbit inclination (i)	0 to 90°	Other values of i and ω would result in configurations that are symmetrical to those already existing and, thus, return similar light curve results. The selected range for Ω ensures geometric transit for a large semi-major axis ($A = 1.377$ AU)
Exoplanet longitude of ascending node (Ω)	$90 - 5 \times 10^{-8^\circ}$ to $90 + 5 \times 10^{-8^\circ}$	
Exoplanet argument of periapsis (ω)	0 to 180°	
Exoplanet radius (R)	$2{,}000$ km to $20R_\oplus$	May vary significantly depending on spot/facula size and brightness
Stellar angular velocity (ω_S)	$-2.5^\circ/\mathrm{h}$ to $2.5^\circ/\mathrm{h}$	Derived from the lower limit of the stellar rotational period (Grouffal et al., 2025), may be in both directions
Initial spot/facula longitude	0° to 360°	Takes all possible values

(λ_0)		
Spot radius (r_{spot})	0 to R_S	Takes all possible values
Spot brightness (B)	0 to 2	The upper boundary is overestimated to guarantee that bright faculae are considered

4.3.5. Third-light dilution inapplicability

Third-light dilution is a photometric effect that occurs when the measured brightness of the host star is contaminated by an additional flux of an unintended light source from the same observational window. This phenomenon can be potentially triggered by background stars, gravitationally bound companions or reflected light from the exoplanets around the observed object.

This effect is important to consider, as it may artificially augment the change in magnitude, as it directly influences the magnitude of the initial flux, thus leading to irrelevant transit depth estimations and possibly hindering ring detection.

However, we do not consider third-light dilution applicable as an alternative explanation to the asymmetries in the transit light curve of HIP 41378f, as there are no light sources that can produce it.

As it is mentioned in Section 4.1 of Grouffal et al., 2025, the host star HIP 41378 is most probably **single** (has no gravitationally bound stars) due to a high value of Renormalised Unit Weight Error in HIP 41378 analysis. This rules out the possibility of third-light dilution due to location in a binary system.

To investigate whether third-light dilution may be present due to a background star, an examination for nearby stars was conducted in the European Space Agency's (ESA) Gaia telescope catalog (Gaia Collaboration et al., 2023) and in the International Variable Star Index (VSX, Watson et al., 2006). The resolution of the K2 data is $3.98”/\text{px}$ (Caldwell et al., 2010). Therefore, when searching for nearby stars that may induce third-light dilution, we looked for stars within $10”$ from HIP 41378f to ensure that HIP 41378f and the detected stars may also be located in the opposite corners of one pixel. Ultimately, no stars brighter than 20.8^m were detected in the selected area. Since the apparent magnitude of HIP 41378f is approximately 8.93^m (Grouffal et al., 2025) and even a 20^m star is $10^{0.4(20-8.93)} \approx 26{,}800$ times less bright than HIP 41378, it is evident that even if third-light dilution from a faint background star exists, its effect on the transit depth and light curve shape is negligible.

To estimate the maximum possible contribution of third-light caused by a planet, the reflected **luminosity** (power of radiation) of the exoplanet must be approximated.

At first, the **illuminance** (total flux per unit of area) of the background exoplanet (E_3) by HIP 41378 is expressed as:

$$E_3 = \frac{L_S}{4\pi d_3^2},$$

where L_S is the stellar luminosity and d_3 is the distance of the exoplanet from HIP 41378.

Then, the total flux covering the exoplanet (F_3) is calculated as:

$$F_3 = E_3 \pi R_3^2,$$

where R_3 is the radius of the exoplanet.

Finally, the reflected luminosity of the exoplanet (L_3) is expressed as:

$$L_3 = F_3 A_3 \Phi_3,$$

where A_3 is the exoplanetary albedo (reflective efficiency) and Φ_3 is the phase of the exoplanet (the fraction expressing the illuminated portion of the planet visible from the Earth).

Therefore, the ratio of the brightnesses of the exoplanet (B_3) and HIP 41378 (B_S) can be expressed as:

$$\frac{B_3}{B_S} = \frac{L_3}{L_S} = \frac{R_3^2 A_3 \Phi_3}{4 d_3^2} \tag{4.16}$$

For the exoplanet to be as bright as possible, the light from the star must be fully ($A_3 = 1$) reflected towards Earth ($\Phi_3 = 1$). To maximize the R_3^2/d_3^2 ratio, the exoplanetary radius was maximized and the distance from HIP 41378 was minimized, with them being empirically set $90{,}000\ \mathrm{km}$ and $0.1\ \mathrm{AU}$, so the brightness ratio results in a minor value of:

$$\frac{B_3}{B_S} = \frac{R_3^2}{4 d_3^2} \sim 10^{-5}$$

Thus, based on knowledge about HIP 41378 being a single star, catalog searches of nearby background stars and effect magnitude estimations for the exoplanet hypothesis, it is safe to assume that the third-light cannot contribute to the overall transit depth and light curve shape. Nevertheless, this effect may be important to consider for other systems.

4.3.6. Gravity darkening inapplicability

Gravity darkening of a star is a phenomenon that occurs due to the star's rapid rotation, which makes the stellar equator cooler and dimmer than its polar regions (e.g., Barnes, 2009; Dholakia et al., 2022). This effect was initially predicted by von Zeipel (von Zeipel, 1924). It occurs when a rapidly rotating star becomes oblate due to centrifugal forces, which, in turn, reduces the effective temperature of the stellar equator. Thus, it significantly alters the intensity distribution of the star, which contributes to the transit light curve shape, especially its ingress and egress stages.

Various estimates show that the rotational period of HIP 41378 lies between 6 and 9 days (Grouffal et al., 2025), which results in its angular velocity of $1.67^\circ/\mathrm{h}$ to $2.50^\circ/\mathrm{h}$.

Combining formulas 3.13 and 3.14 from Costa, 2019, the **critical stellar angular velocity** ω_{crit} (the angular velocity at which the centrifugal force at the stellar equator becomes equal to the gravitational force) can be estimated as:

$$\omega_{\mathrm{crit}} = \sqrt{\frac{8GM_S}{27R_S^3}} = \sqrt{\frac{8g}{27R_S}} \approx 97.59^\circ/\mathrm{h}, \tag{4.17}$$

where M_S, R_S and g are stellar mass, radius and surface gravity, respectively.

From the calculations above, we get the predicted values of $\omega_S/\omega_{\mathrm{crit}}$ from 0.017 to 0.026. At the same time, for stars rotating well below $\omega_S/\omega_{\mathrm{crit}} \sim 0.6$, the photometric impact of gravity darkening is negligible (Costa, 2019). As $\omega_S/\omega_{\mathrm{crit}}$ for HIP 41378 is an order of magnitude less than 0.6, the brightness distribution of the star can be estimated with high accuracy by the standard quadratic limb-darkening model (see Section 2.4).

Moreover, gravity darkening insignificancy is supported by its low estimated value of $v_{\mathrm{eq}} \sin i_S \approx 6.3\ \mathrm{km\ s^{-1}}$ (apparent sky-projected stellar rotation, Grouffal et al., 2025), compared to fast rotators like WASP-33 with $v_{\mathrm{eq}} \sin i_S \approx 86.5\ \mathrm{km\ s^{-1}}$ (Dholakia et al., 2022). The late F type of HIP 41378 (Grouffal et al., 2025) also implies the small effect of the gravity darkening signature compared to hotter and more radiative A-type stars (von Zeipel, 1924).

4.3.7. Model comparison

To evaluate the robustness of the hypothesis of a ring system around HIP 41378f, we performed a comparative analysis against four alternative models, created in Sections 4.3.1-4.3.4: a standard spherical planet, an oblate planet, a model accounting for observational noise and a model incorporating spherical activity (starspots/faculae). The statistical plausibility of the primary model is assessed through visual inspection of residuals (Figure 15), comparison of Bayesian evidence values (Table 11) and the stability of posterior parameter estimates (Table 12).

As it is evident from Figure 15, the ring model exhibits the most precise alignment with the observed data, particularly in the ingress, midtransit and egress stages, with residuals centered closely around zero, where other models result in much more

scattered residuals. Conversely, the ringless model partially captures the ingress and the egress stages but fails to precisely align with the midtransit; the oblate planet model manages to capture the midtransit with better precision but faces strong misalignment with data at both the ingress and the egress stages, and the two other models fail to fit all three of these stages. This suggests that each of the four alternative models fails to capture all light curve features alone.

The statistical superiority of the ring hypothesis is also quantitatively confirmed by the matrix of Bayesian log-evidence differences (Table 11). In every comparison to other models, the ringed model is overwhelmingly preferred ($\Delta \ln Z > 5{,}240$), rejecting other hypotheses. Among ringless alternatives, the oblate planet model is the most successful, outperforming the spherical ringless model by $\Delta \ln Z \approx 2{,}282.54$. This suggests that the spherical ringless alternatives are not complex enough to reproduce the geometric asymmetries in the light curve. Both the noise and the stellar activity models are outperformed by the simple spherical model with $\Delta \ln Z \approx 618.16$ and $\Delta \ln Z \approx 622.55$, respectively, although they create fits with almost similar log-likelihood values. Thus, the favorability of the simple model over the noise and spots/faculae alternatives can be simply explained by their unneeded complexity. Similarly, the noise model is slightly preferred over the spots/facula hypothesis ($\Delta \ln Z \approx 4.39$), as the latter introduces two more parameters that lead to an unneeded increase in complexity, while not leading to better fits (the starspots/faculae can add extra features to the light curve, but they are too local compared to the ringed alternative).

However, it is important to acknowledge the abnormal magnitudes of the inferred $\Delta \ln Z$ values. Differences in log-evidences of this scale are anomalous in exoplanetary analysis, where $\Delta \ln Z > 5$ is already considered strong evidence of one model over another. These extreme values may arise from numerical instabilities in the nested sampling algorithm, its precision limits, high-dimensionality and multimodality. Nevertheless, combined with the clear visual evidence from the residuals in Figure 15, these results do not leave doubt about the statistical preference of the ringed model against other hypotheses.

The primary model's validity is further suggested by the posterior distributions summarized in Table 12. For the ring model, the parameters are tightly constrained and have minute uncertainties (e.g., $a = 2{,}698{,}000^{+4{,}000}_{-4{,}000}$ km and $i = 84.6^{+0.1^\circ}_{-0.3}$). On the contrary, the uncertainties in alternative model estimates allow for much broader intervals (e.g., $i = 50^{+30^\circ}_{-30}$). This indicates the convergence of the main model on a physically plausible and precise solution.

Therefore, of all suggested transit asymmetry hypotheses, the observed data is most consistent with the ringed model.

4.4. Model limitations

Although the proposed model is effective in predicting transit light curves, it has several issues that should be addressed. In this section, the drawbacks of the model are outlined, highlighting the areas for future improvement.

4.4.1. Computational complexity

Although the pixel-based approach simplifies the inclusion of more physical parameters, one of its main issues is its numerical nature. While the pixel-based algorithm allows for calculating the model with high precision, the quality is

dependent on the pixel size of the matrices. Higher precision requires smaller pixel sizes for resolving the details of the exoplanet and its rings better on their grid representations. However, a smaller pixel size requires the matrix representations to have more pixels. Then, with better resolution, the calculations become computationally intensive as they require repeatedly recalculating and summing matrices with thousands of pixels for every time step of the transit.

Also, the model's simulation of orbital motion relies on solving Kepler's equation to determine the position of the exoplanet at every time step. While analytical solutions are not available, numerical methods are used. This significantly increases computational complexity, especially when modeling long-duration transits.

Furthermore, finding the transit window for more precise calculations of the light curve is also a non-trivial task. We must analyze a wide range of data points in order to narrow the transit search window. In this work, the approximate transit window is evaluated analytically. Then, it is narrowed down by iterating through the initial window range. After that, the transit light curve is computed by iterating through a narrowed window. This approach is essential, as the transit is very quick compared to the whole orbital period of the exoplanet. Thus, a total of $s_o + s = 900$ masking iterations is needed to evaluate the transit light curve. This is only deteriorated by the selection of priors that are very broad (Section 3.2), as it leads to an increase in the number of nested sampling iterations required to converge due to prior sensitivity of the model. Thus, for $N_{\text{call}} = 39{,}597$ (see Section 4.2), a total of $35{,}637{,}300$ magnitude change calculations is required. At the same time, each magnitude change calculation is a complex operation itself, which creates, masks and sums matrices with thousands of pixels.

In our work, this issue is partially addressed by selecting an optimal pixel size. We chose the pixel size value that is large enough to sustain fast calculations, but still gives enough precision. As a result, calculation of a light curve for a specific set of parameters may take 2-3 seconds (depending on hardware and specific parameter values), requiring 20 to 40 hours to complete the nested sampling with $N_{\text{call}} = 39{,}597$.

The issue may be further addressed by favoring the impact parameter over the orbit's rotational parameters. This solution would eliminate the need for the search for the transit window, iterate over it for narrowing it and the need to solve Kepler's equation. Instead, the model would make fewer iterations by just moving the masking matrix along the star's grid in a line set by the impact parameter. The improvement would work better for planets distant from their host stars, as their projected orbits during the transit stage would be very similar to straight lines.

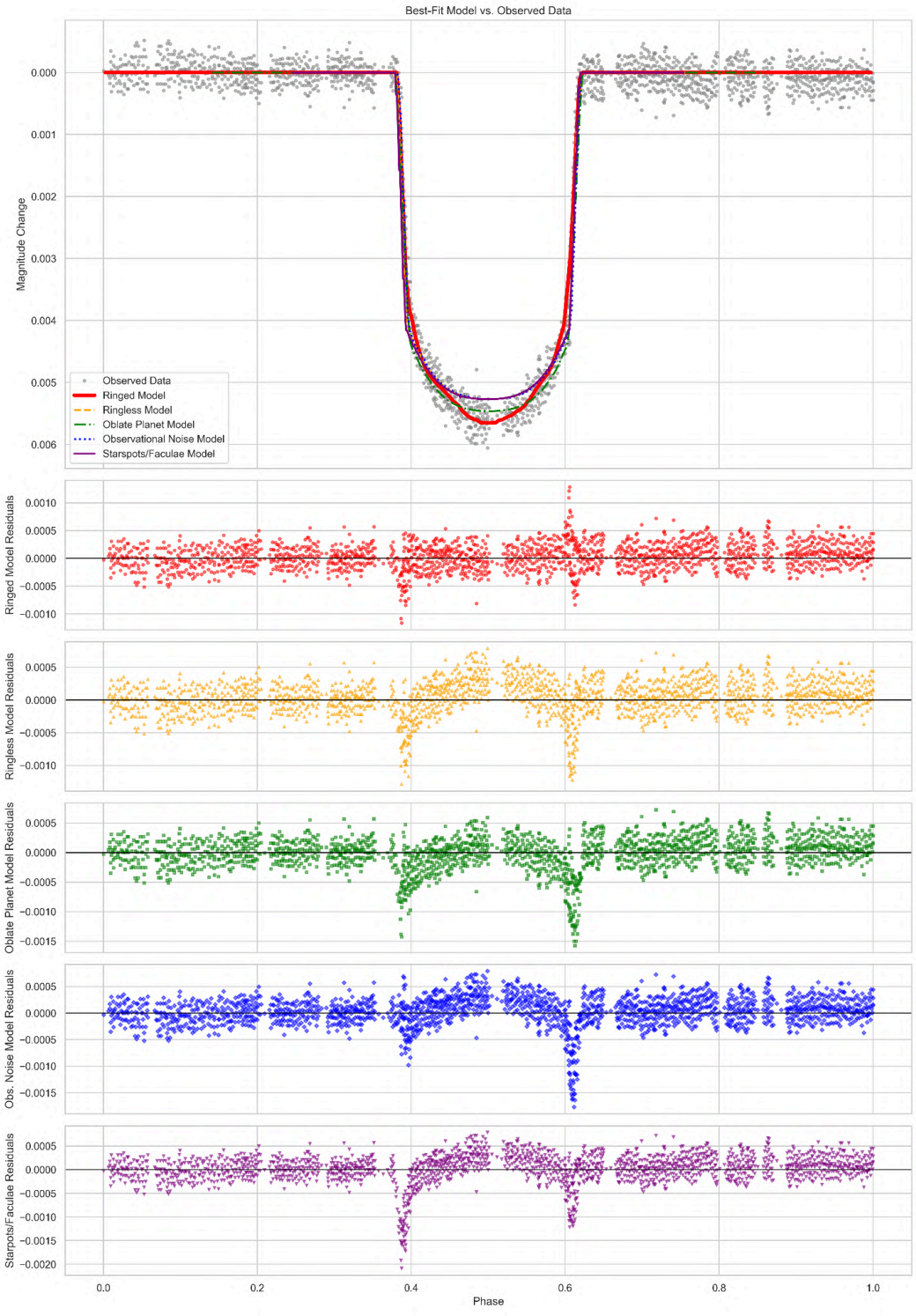
Best-Fit Model vs. Observed Data
Magnitude Change
Observed Data
Ringed Model
Ringless Model
Oblate Planet Model
Observational Noise Model
Starspots/Faculae Model
Ringed Model Residuals
Ringless Model Residuals
Oblate Planet Model Residuals
Obs. Noise Model Residuals
Starspots/Faculae Residuals
Phase

Figure 15. Best-fit light curves and residuals for the primary (ringed model) and four alternative ringless models that take into account various minor effects (ringless, oblate planet, observational noise and starspots/faculae). The upper panel displays the observational data (gray circles) overlaid with the best-fit light curves for each of the alternative models: ringed (main) model (red wide solid line), ringless model (yellow dashed line), oblate planet model (green dash-dot line), observational noise model (blue dotted line) and starspots/faculae model (purple solid line). Their respective residuals are represented by unique markers: red circles (ringed), yellow upward triangles (ringless), green squares (oblate planet), blue diamonds (observational noise) and purple downward triangles (starspots/faculae). According to the residuals, the ringed model fit is the best fit of the observed data, along with the oblate planet model yielding the second-best fits and other models yielding fairly similar fits that are a worse representation of the data.

4.4.2. Challenges with Data-fitting

The model's effectiveness is heavily reliant on the parameter fitting process, specifically on the choice of the data fitting algorithm.

At first, we used MCMC (Markov Chain Monte Carlo, Foreman-Mackey et al., 2013) with 10,000 iterations, which was not enough for high-precision results. This means that some of the model parameters could be effectively determined, reaching a plateau in the MCMC chain, while others could still stay in their **burn-in** stage (the first values used in the MCMC that can be inadequately influenced by initial guess values), resulting in convergence issues. Another issue posed by using the MCMC was the local likelihood maxima traps. The MCMC would stop after finding one local log-likelihood maximum that was closest to the initially guessed values, ignoring the necessity of exploring the full parameter space in order to draw more specific conclusions.

To distinguish these scenarios and draw the most accurate conclusion, the data-fitting algorithm was switched to nested sampling. Unlike MCMC, nested sampling was able to converge fully in $N_{\text{call}} = 39{,}597$ steps within the accuracy of the stopping function. Moreover, it has explored the entire parameter space, yielding several local maxima and bypassing the issues related to burn-in.

The high shrinkage ($\mathcal{S}$) values observed across most model parameters indicate that the final posterior distributions are primarily driven by the observational data, not by the initial prior assumptions (Section 3.2). However, a notably lower shrinkage value for one parameter: the longitude of the ascending node. $\mathcal{S} = 0.4303$ occurred due to its exceptionally narrow prior bounds, which were strictly constrained to ensure a geometric transit occurred given the planet's large semi-major axis. This further indicates that the parameter space was explored fully and resulted in adequate posterior distributions for each parameter.

Nevertheless, the high-dimensionality of our model remains a challenge. In particular, the evidence calculation and the resolution of small likelihood peaks are heavily reliant on the number of live points N_{live} used. While $N_{\text{call}} = 39{,}597$ indicates convergence, a higher density of live points may still be required to fully resolve more local maxima the subtle degeneracies between a large, translucent ring and a smaller, opaque one.

Table 11. The matrix of relative values of Bayesian log-evidences ($\Delta \ln Z$) for the primary (ringed model) and four alternative ringless models that take into account various minor effects (ringless, oblate planet, observational noise and starspots/faculae). The values in the table represent the difference between the log-evidences of models indicated in the row and the column ($\Delta \ln Z = \ln Z_{\text{row}} - \ln Z_{\text{column}}$) calculated via nested sampling based on Bayesian evidence weights of each model. Positive values indicate a statistical preference of the model in the respective row over the model in the selected column. The superiority of the primary (ringed) model over all alternative model fits ($\Delta \ln Z > 5{,}240$) confirms that the ring hypothesis is the most consistent with data. The abnormally large values of $\Delta \ln Z$ indicate that errors in evidence weights calculations might have occurred during the nested sampling algorithm. Nevertheless, combined with residual analysis, this table indicates the statistical favorability of the ringed hypothesis.

$\Delta \ln Z$	**Ringed**	**Ringless**	**Oblate planet**	**Observational noise**	**Starspots/ faculae**
Ringed	0.00	$+7{,}530.53$	$+5{,}247.99$	$+8{,}148.69$	$+8{,}153.08$
Ringless	$-7{,}530.53$	0.00	$-2{,}282.54$	$+618.16$	$+622.55$
Oblate planet	$-5{,}247.99$	$+2{,}282.54$	0.00	$+2{,}900.70$	$+2{,}905.09$
Observational noise	$-8{,}148.69$	-618.16	$-2{,}900.70$	0.00	$+4.39$
Starspots/ faculae	$-8{,}153.08$	-622.55	$-2{,}905.09$	-4.39	0.00

Convergence
A Journal for Young Researchers

Table 12. Values of best-fit model parameters from the nested sampling simulation compared for the primary (ringed) model and four alternative hypotheses (ringless, oblate planet, observational noise, starspots/faculae). The values themselves represent the median points of the posterior distributions for each parameter, and the upper and lower error limits of the parameter values represent 1σ confidence intervals. The priors are uniform and recorded in Table 3 (ringed), Table 6 (ringless), Table 7 (oblate planet), Table 9 (observational noise) and Table 10 (starspots/faculae). The table uses the following parameter notation: e_p - orbit eccentricity, i - orbital inclination, Ω - orbital longitude of ascending node, ω - orbital argument of periapsis, R - exoplanetary radius, e - ring eccentricity, a - ring semi-major axis, w - ring width, θ - ring obliquity, ϕ - ring azimuthal angle, ψ - ring argument of periapsis, R_e - equatorial exoplanetary radius, f - exoplanet oblateness, β - oblate planet projection rotation angle, σ_n - noise scale, υ - noise magnitude, ω_S - stellar angular rotation velocity, λ_0 - initial starspot/facula longitude, r_{spot} - starspot/facula radius, B - ratio of starspot/facula brightness to stellar brightness.

Ringed		**Ringless**		**Oblate planet**		**Observational noise**		**Starspots/faculae**	
Parameter	**Estimate**	**Parameter**	**Estimate**	**Parameter**	**Estimate**	**Parameter**	**Estimate**	**Parameter**	**Estimate**
e_p	0.003	e_p	0	e_p	$0.13^{+0.15}_{-0.09}$	e_p	$0.13^{+0.10}_{-0.09}$	e_p	$0.14^{+0.15}_{-0.09}$
$i, ^\circ$	$84.6^{+0.1}_{-0.3}$	$i, ^\circ$	40^{+30}_{-20}	$i, ^\circ$	50^{+30}_{-30}	$i, ^\circ$	40^{+30}_{-30}	$i, ^\circ$	50^{+30}_{-30}
$\Omega, ^\circ$	90°	$\Omega, ^\circ$	90°	$\Omega, ^\circ$	90°	$\Omega, ^\circ$	90°	$\Omega, ^\circ$	90°
$\omega, ^\circ$	$0.78^{+0.03}_{-0.03}$	$\omega, ^\circ$	$1.6^{+1.2}_{-1.2}$	$\omega, ^\circ$	40^{+30}_{-30}	$\omega, ^\circ$	40^{+30}_{-30}	$\omega, ^\circ$	40^{+30}_{-30}
R, km	$46{,}200^{+1{,}300}_{-900}$	R, km	$59{,}500^{+400}_{-700}$	R_e, km	$82{,}000^{+29{,}000}_{-21{,}000}$	R, km	$61{,}000^{+11{,}000}_{-10{,}000}$	R, km	$52{,}000^{+15{,}000}_{-16{,}00}$

e	$0.418^{+0.002}_{-0.002}$		f	$0.6^{+0.2}_{-0.4}$	σ_n	$0.004^{+0.002}_{-0.002}$	ω_S	$0.001^{+0.000}_{-0.001}$
a, km	$2{,}698{,}000^{+4{,}000}_{-4{,}000}$		β, °	90^{+60}_{-60}	υ	$0.002^{+0.001}_{-0.002}$	λ_0	190^{+120}_{-120}
w, km	$374{,}200^{+2{,}800}_{-3{,}000}$						r_{spot}, R_S	$0.5^{+0.4}_{-0.3}$
θ, °	$0.969^{+0.003}_{-0.006}$						B	$1.0^{+0.7}_{-0.6}$
ϕ, °	$56.45^{+0.21}_{-0.27}$							
ψ, °	$42.7^{+1.3}_{-1.4}$							

The high dimensionality of the model and the insufficient amount of live points may also be the main causes of the challenge in the calculation of log-evidence, which exhibits an unexpectedly high difference between fits of different models. The extreme $\ln Z$ differences highlighted in Table 11 may suggest that the nested sampling algorithm has encountered numerical divergence. This may occur due to the mathematical inability of alternative models to provide near-perfect geometric fits similar to that of the ringed model, making both log-likelihoods and log-evidences significantly diverge between different scenarios. Therefore, although the ringed model is statistically preferred over the alternatives, the $\Delta \ln Z$ magnitudes may be overestimated due to precision limits.

Another issue with data-fitting is related to the difficulty of defining whether the transit is central or not for distant exoplanets. Transits of distant exoplanets mainly occur when the orbits of these planets lie in almost edge-on orientations. This means that a negligible change of inclination ($i \approx 0^\circ$) or longitude of ascending node ($\Omega \approx 90^\circ$) can result in making a central transit non-central or even invisible. Thus, it is highly possible that the nested sampling would not be able to distinguish the small difference, favoring fully edge-on orientations and central transits as a result. Similar to computational complexity, this problem must be tackled by replacing the orbit's rotational properties with the impact parameter.

4.4.3. Observational Limitations

Added to the model's internal issues, external factors also pose limitations.

Even the data from state-of-the-art observational facilities often contains a significant amount of noise due to various factors, including atmospheric interference, instrument noise, and stellar variability. This high noise level can be even more noticeable than the subtle photometric signatures of a ring system, making it challenging for our model to correctly fit the light curve and accurately constrain the parameters. In these conditions, the model may be attempting to fit observational noise instead of the ring features. Thus, much more precise data from next-generation telescopes is required to confidently distinguish between the variation triggered by noise and the true signature of a ring.

As mentioned previously (see Section 3), stacking data combined from different observational epochs introduces the risk of ignoring ring and exoplanet precession, which might lead to significant errors in the determined parameter values.

4.4.4. Parameter correlations and degeneracies

For detecting possible parameter correlations and degeneracies, a correlation heatmap was constructed based on the parameter sets and their corresponding resulting log-likelihood values (see Figure 14).

The values of the **Pearson correlation coefficient (**PCC**)** - the statistical measure that quantifies the linear relationship between two variables, ranging from -1 to +1 - in the correlation heatmap (Figure 14) reveals several critical degeneracies.

One of the main possible causes of the degeneracies in the exoplanet's orbital parameters is that different sets of orbital parameter values can yield similar trajectories of the exoplanet's transit. Thus, for improving the understanding of the parameter correlations, the impact parameter (b) must be derived in terms of the fit orbital parameters, as it is the main quantity representing the transit trajectory for long-period planets (because their trajectories can be approximated as straight lines).

From the geometry of projecting the trajectory on the stellar surface:

$$b = \frac{r_{\mathrm{tra}}}{R_S} \cos i,$$

where r_{tra} is the distance between the star and the planet at the time of transit.

Using the ellipse equation in polar coordinates (formula 2.5.13):

$$r_{\mathrm{tra}} = \frac{A(1 - e_p^2)}{e_p \cos \nu}$$

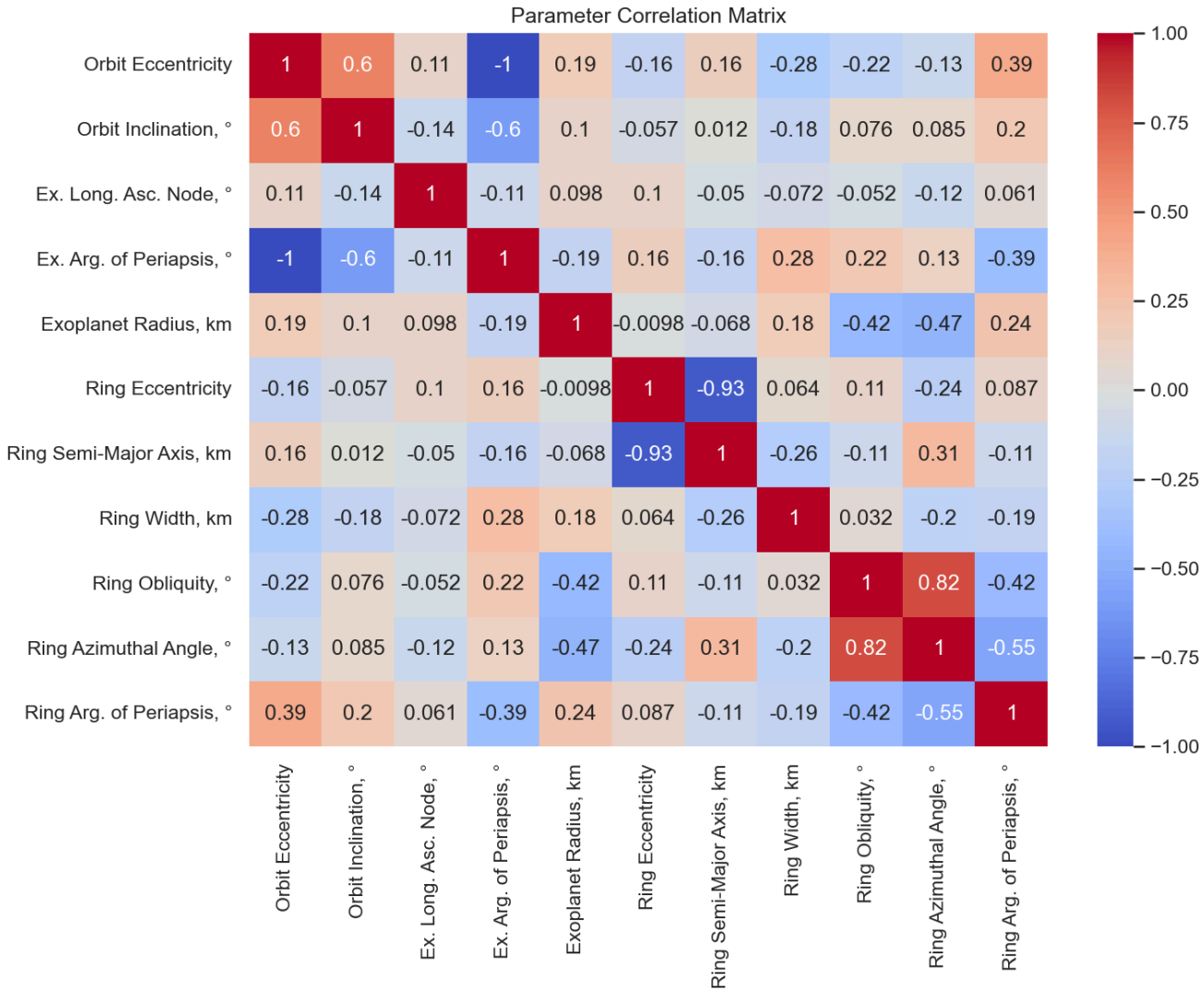

Figure 14. The parameter correlation matrix derived from the posterior samples of the 11-parameter nested sampling analysis. The color scale represents the Pearson correlation coefficient for every pair of 11 parameters used in nested sampling, ranging from -1 (perfect negative correlation, dark blue) to +1 (perfect positive correlation, dark red). The correlation heatmap was produced using the data of every function call in the nested sampling. This matrix highlights the significant degeneracies that occur in the ringed exoplanet model, particularly between orbital dynamics (orbital eccentricity vs. orbital argument of periapsis, and orbital inclination vs. orbital argument of periapsis) and ring geometry (eccentricity vs. semi-major axis, and obliquity vs. azimuthal angle).

When the projection of the planet is the closest to the center of the star, the true anomaly (ν) can be expressed as:

$$\nu = 90^\circ - \omega$$

Therefore:

$$b = \frac{A}{R_S} \cos i \left(\frac{1 - e_p^2}{1 + e_p \sin \omega} \right) \tag{4.5}$$

One of the most striking degeneracies detected is quantified by the near-perfect negative correlation ($\mathrm{PCC} = -1.00$) between the orbit eccentricity (e_p) and the exoplanet's argument of periapsis (ω). This correlation occurs mainly because, for long-period exoplanets, any change in the orbital eccentricity can be compensated by a respective change in the planetary argument of periapsis. It can be further confirmed by equation 4.5, as it has a product of e_p and ω as a term in its denominator. Additionally, the effect of $1 - e_p^2$ in the numerator is minor, resulting in an almost perfect negative correlation.

Another noticeable degeneracy in the orbital parameter of the exoplanet can occur due to a noticeable negative correlation ($PCC = -0.60$) between the orbital inclination (i) and the exoplanet's argument of periapsis (ω). This, again, highlights that different sets of orbital parameters can result in very similar transit trajectories for long-period planets. More importantly, the orbital inclination plays a minor role in determining the exoplanet's transit trajectory, as the orbit has to be close to edge-on to ensure that the transit occurs. This can be also confirmed by equation 4.5, as it has $\cos i$ and $\sin \omega$ in the opposite sides of the fraction, with i and ω both occurring only once in the equation, which results in the identified negative degeneracy. This degeneracy is also supported by the bimodality of the posterior distributions of i and ω (see Section 4.2 and Figure 10).

Thus, similarly to other limitations, the degeneracies between the exoplanet's orbital parameters can be addressed by switching from the parameters of orbital eccentricity, inclination, longitude of ascending node and argument of periapsis to the impact parameter. Although this solution can prove itself physically ineffective for short-period planets (e.g., Hot Jupiters), it would be effective for long-period exoplanets like HIP 41378f

The most powerful degeneracy within the identified ring properties would most probably be related to the high negative correlation ($\mathrm{PCC} = -0.93$) between the ring eccentricity (e) and its semi-major axis (a). This strong correlation clearly demonstrates that the quality of the fit data is insufficient for the model to clearly identify whether the ring is eccentric or circular. Due to that, a more eccentric compact ring may produce a similar log-likelihood to a less eccentric but bigger ring, as they both affect the transit depth, leaving different traces in graph asymmetries only (Section 4.1), which require higher data precision to be resolved. The effect of the eccentricity on the transit depth is minor ($\sqrt{1 - e^2}$, see equation 4.1). Therefore, it is reasonable to remove the eccentricity parameter (and, consequently, the parameter of argument of periapsis, as it has no effect for zero eccentricity), switching to a circular ring model instead in order to avoid the degeneracy in the ring's semi-major axis.

Another significant correlation is between the ring obliquity (θ) and azimuthal angle (ϕ). This correlation is highly predictable for the near edge-on configuration that the rings are hypothesized to exhibit. For small ring obliquity values, the mask of the rings is very similar for various azimuthal angle values, resulting in both similar transit depths and similar light curve shapes. As there is no simple way of distinguishing different azimuthal angle values for near edge-on configurations, the results for θ and ϕ must be treated as an indicator of the almost edge-on case rather than a physically reliable exact orientation of rings.

4.4.5. Model predictivity and handling data with gaps

To validate the **predictive improvement** of the model (the quantified increase in the model's ability to explain the observed data as more initial information is provided to the fit), the **k-fold cross-validation** (a method of repetitive data-fitting that uses different portions of the observations as input data sets).

To implement the k-fold evaluation algorithm, the data set was initially split into $k = 5$ equal temporal portions of data that represent five key transit stages: Fold 0 - ingress, Fold 1 - pre-midtransit, Fold 2 - midtransit, Fold 3 - post-midtransit and Fold 4 - egress (see the folds in Figure 16). Each of the resulting portions of data was then removed one by one in rotation, passing the other four parts as an input for the main nested sampling algorithm, which is described in Section 3. The best-fits generated by every k-fold test are displayed in Figure 16.

The selected approach helps validate if the ring signatures detected by the main run (Section 4.2) are a coherent global feature or a localized anomaly, assisting with confirmation of the model's generalizability and ensuring that the model is not overfitting local noise or instrumental artifacts.

This approach is especially necessary for long-period transits like HIP 41378f, where data gaps might occur due to instrumental specifics or other observational limitations (e.g., an unexpected bright radiation source in the foreground), which must not bias parameter recovery because the model relies too heavily on specific parts of the transit light curve.

The best-fit light curves with stacked residuals for each iteration of k-fold cross-validation are displayed in Figure 16. The comparison of resulting log-evidences and inferred values of system parameters is displayed in Table 13 and Table 14, respectively.

The comparison of fit shapes and $\ln Z$ values for different folds are highly important to evaluate the predictive improvement of the model, but insufficient to draw a definitive conclusion about the model's ability to fit data with gaps. For that reason, we also compare the estimated parameter values and their uncertainty ranges (see Table 14).

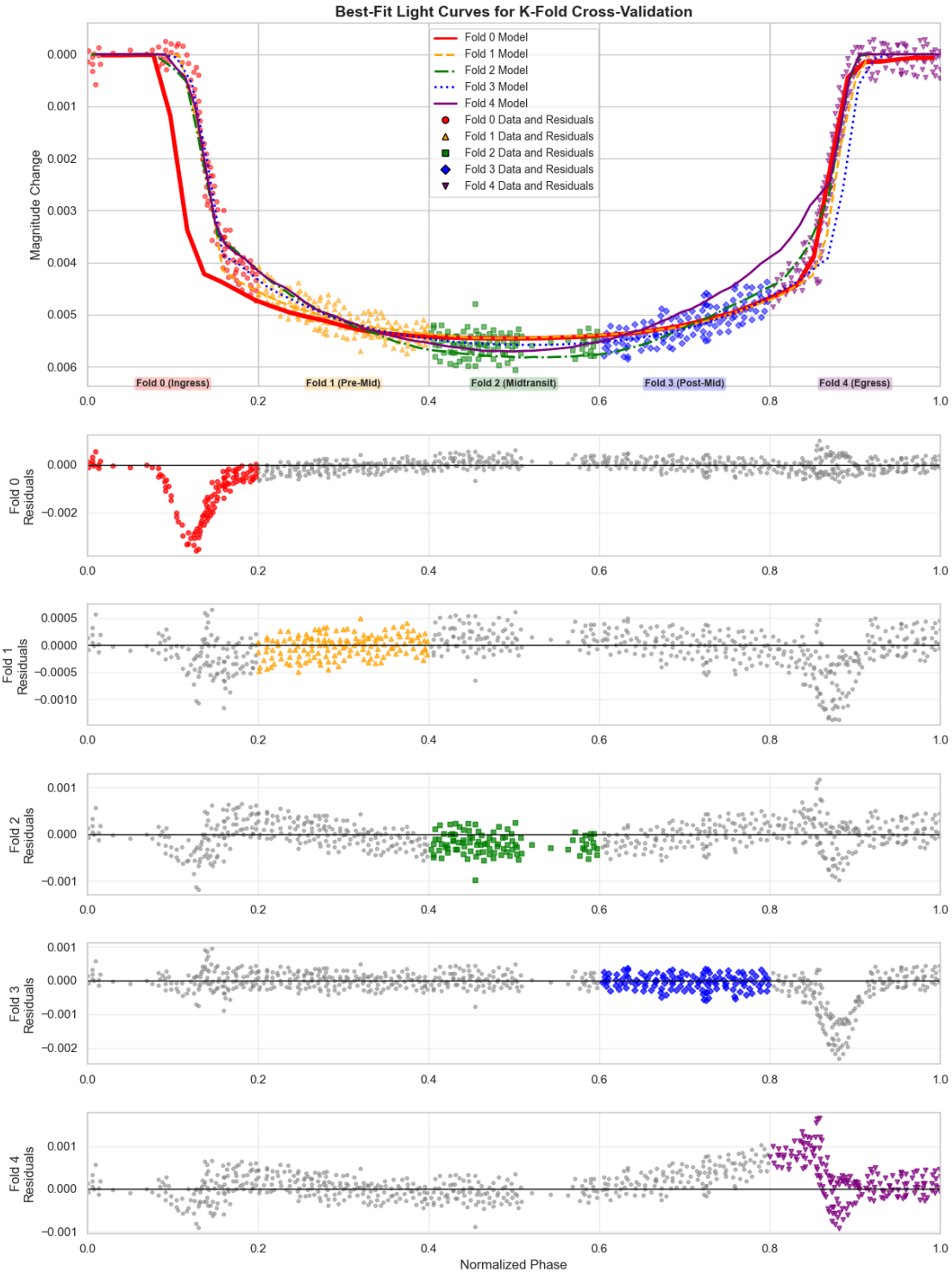
Best-Fit Light Curves for K-Fold Cross-Validation
Fold 0 Model
Fold 1 Model
Fold 2 Model
Fold 3 Model
Fold 4 Model
Fold 0 Data and Residuals
Fold 1 Data and Residuals
Fold 2 Data and Residuals
Fold 3 Data and Residuals
Fold 4 Data and Residuals
Magnitude Change
Fold 0 (Ingress)
Fold 1 (Pre-Mid)
Fold 2 (Midtransit)
Fold 3 (Post-Mid)
Fold 4 (Egress)
Fold 0 Residuals
Fold 1 Residuals
Fold 2 Residuals
Fold 3 Residuals
Fold 4 Residuals
Normalized Phase

Figure 16. Best-fit light curves and residuals for the five k-fold cross-validation iterations (Fold 0 — ingress removed, Fold 1 — pre-midtransit removed, Fold 2 — midtransit removed, Fold 3 — post-midtransit removed, Fold 4 — egress removed). The upper panel displays the observational data separated into five folds (they are highlighted by different colors and marker styles) overlaid with the best-fit light curves for each k-fold iteration: Fold 0 (red wide solid line), Fold 1 (orange dashed line), Fold 2 (green dash-dot line), Fold 3 (blue dotted line), and Fold 4 (purple solid line). Observational data and their respective residuals are represented by unique markers: circles (Fold 0), upward triangles (Fold 1), squares (Fold 2), diamonds (Fold 3), and downward triangles (Fold 4). According to the residuals for the removed parts of the graph for each k-fold, the fit quality deteriorates when less data is input, which indicates the predictive improvement of the model. Despite the exclusion of the critical phases, all five models converge onto a notably similar transit profile, which confirms the stability of ring detection and advocates against overfitting of local noise.

Based on Table 1, it can be confirmed that each phase of the exoplanetary transit (ingress, egress and midtransit) carries critically important information. This is verified by the abnormally large values of relative Bayesian log-evidence ($\Delta \ln Z$) between the main model and each of the k-fold fits (~ 860 to $1{,}060$), with $\Delta \ln Z > 5$ already considered strong evidence of one model over another in Bayesian statistics. This difference is especially strong when comparing the main model with Fold 1 (pre-midtransit removed, $\Delta \ln Z \approx 1{,}066$) and Fold 3 (post-midtransit removed, $\Delta \ln Z \approx 1{,}044$). The positive values of $\Delta \ln Z$ for all comparisons of k-folds against the main model confirm that adding new data improves model predictivity, which is a characteristic of a real signal.

Nevertheless, the k-fold cross-validation results also confirm that the model does not overfit local noise and show stable ring detection across all fits. Table 13 and Figure 16 show that removing data at any of the main transit stages catastrophically deteriorates both the log-evidence result and the residuals, which would not be the case when the model fits noise instead of real light curve features. This is also confirmed by the relatively small difference between $\ln Z$ amongst the k-folds (e.g., $\Delta \ln Z \sim 22$ between Fold 1 and Fold 3) compared to the drastic $\ln Z$ change between the model and the k-folds, which suggests that the signal is distributed fairly uniformly along the light curve and there are no local anomalies that fully determine the statistical plausibility.

The consistency of ring detection and the reproducibility of positive results are also supported by the k-fold best-fit parameters yielded by nested sampling in Table 14. For instance, the k-fold radius estimates are relatively consistent ($47{,}700$ km to $58{,}344$ km) and less than $9.2R_{\oplus}$ (Santerne et al., 2019), which can be classified as a stable partial explanation of the "super-puff" phenomenon through the ring hypothesis when taking into account that 20% of the data are removed for each fit. The ring parameters (semi-major axis, width, eccentricity and obliquity) possess physically plausible values for every fold, always suggesting a large and eccentric ring system in a configuration close to edge-on. Fold 2 suggests the most similar values to the main model compared to other k-folds, showing that the inferred values are mainly determined by the asymmetries in the transit ingress and egress, and not by random error in the observations.

The physical plausibility of the fit can also be confirmed by the high sensitivity of inferred orbital inclination values to the input data (Table 14). This effect is especially evident for Fold 0 (60°, different by approximately 25° from the main fit). It occurs because the ingress transit stage stores the key signatures caused by orbital inclination. This proves that the model

honestly shows the uncertainty when the parts of the data are removed. The model fidelity is also evident from the residuals in Figure 16, where the model fits the incomplete input data well but fails to fit the removed data with high accuracy in Fold 0 and Fold 4.

Therefore, the model passes the k-fold cross-validation: the results disapprove noise overfitting, are resilient to data loss, statistically robust and physically plausible. This confirms that the model is **consistent with rings**. However, for the best results, it is essential to use observations without time gaps.

Table 13. The matrix of relative values of Bayesian log-evidences ($\Delta \ln Z$) for the primary model and five iterations of k-fold cross-validation (Fold 0 - ingress removed, Fold 1 - pre-midtransit removed, Fold 2 - midtransit removed, Fold 3 - post-midtransit removed, Fold 4 - egress removed). The values in the table represent the difference between the log-evidences of models indicated in the row and the column ($\Delta \ln Z = \ln Z_{\text{row}} - \ln Z_{\text{column}}$) calculated via nested sampling based on Bayesian evidence weights of each model. Positive values indicate a statistical preference of the model in the respective row over the model in the selected column. The superiority of the main (full data) model over all iterations of cross-validation ($\Delta \ln Z > 860$) confirms that the information signal is spread over the entire transit light curve and is not caused by local anomalies, so full data is required for best parameter estimation, which confirms the predictive improvement of the model. The high statistical stability of the results for light curves with various excluded transit phases verifies the reliability of ring detection.

$\Delta \ln Z$	**Main model (Full data)**	**Fold 0 (Ingress)**	**Fold 1 (Pre-Mid)**	**Fold 2 (Midtransit)**	**Fold 3 (Post-mid)**	**Fold 4 (Egress)**
Main model	0.00	+973.75	+1,065.68	+1,002.161	+1,043.94	+864.95
Fold 0	−973.75	0.00	+91.93	+28.41	+70.19	−108.8
Fold 1	−1,065.68	−91.93	0.00	−63.52	−21.74	−200.73
Fold 2	−1,002.16	−28.41	+63.52	0.00	+41.78	−137.21

Fold 3	$-1{,}043.94$	-70.19	$+21.74$	-41.78	0.00	-178.99
Fold 4	-864.95	$+108.8$	$+200.73$	$+137.21$	$+178.99$	0.00

Table 14. Values of ring and exoplanet properties from the nested sampling simulation compared for the main model and each of the five k-folds (Fold 0 - ingress removed, Fold 1 - pre-midtransit removed, Fold 2 - midtransit removed, Fold 3 - post-midtransit removed, Fold 4 - egress removed). The values themselves represent the median points of the posterior distributions for each parameter, and the upper and lower error limits of the parameter values represent 1σ confidence intervals. The priors are uniform and recorded in Table 3.

Estimated parameter name	**Main model (Full data)**	**Fold 0 (Ingress)**	**Fold 1 (Pre-Mid)**	**Fold 2 (Midtransit)**	**Fold 3 (Post-mid)**	**Fold 4 (Egress)**
Exoplanet orbit eccentricity (e_p)	0.003	$0.014^{+0.000}_{-0.005}$	0	0.002	0	0.003
Exoplanet orbit inclination (i), °	$84.58^{+0.15}_{-0.33}$	60^{+0}_{-20}	$72.106^{+0.014}_{-0.019}$	$77.32^{+0.02}_{-0.03}$	$88.2^{+0.1}_{-0.4}$	$86.61^{+0.05}_{-0.13}$
Exoplanet longitude of ascending node (Ω), °	90	90	90	90	90	90
Exoplanet argument of periapsis (ω), °	$0.78^{+0.03}_{-0.03}$	18^{+0}_{-5}	Circular orbit	$4.048^{+0.008}_{-0.005}$	Circular orbit	$9.06^{+0.13}_{-0.02}$

Convergence
A Journal for Young Researchers

Estimated parameter name	Main model (Full data)	Fold 0 (Ingress)	Fold 1 (Pre-Mid)	Fold 2 (Midtransit)	Fold 3 (Post-mid)	Fold 4 (Egress)
Exoplanet orbit eccentricity (e_p)	0.003	$0.014^{+0.000}_{-0.005}$	0	0.002	0	0.003
Exoplanet orbit inclination (i), °	$84.58^{+0.15}_{-0.33}$	60^{+0}_{-20}	$72.106^{+0.014}_{-0.019}$	$77.32^{+0.02}_{-0.03}$	$88.2^{+0.1}_{-0.4}$	$86.61^{+0.05}_{-0.13}$
Exoplanet radius (R), km	$46{,}200^{+1{,}300}_{-900}$	$56{,}700^{+1{,}800}_{-0}$	$58{,}344^{+14}_{-11}$	$47{,}700^{+1{,}600}_{-1{,}700}$	$48{,}690^{+40}_{-170}$	$55{,}870^{+60}_{-30}$
Ring eccentricity (e)	$0.418^{+0.002}_{-0.002}$	$0.73^{+0.07}_{-0.00}$	0.544	$0.435^{+0.003}_{-0.002}$	$0.800^{+0.005}_{-0.005}$	$0.619^{+0.001}_{-0.005}$
Ring semi-major axis (a), km	$2{,}698{,}000^{+4{,}000}_{-4{,}000}$	$4{,}000{,}000^{+0}_{-500{,}000}$	$3{,}472{,}200^{+1{,}300}_{-1{,}200}$	$2{,}451{,}000^{+4{,}000}_{-6{,}000}$	$1{,}871{,}000^{+11{,}000}_{-5{,}000}$	$3{,}397{,}000^{+25{,}000}_{-5{,}000}$
Ring width (w), km	$374{,}000^{+3{,}000}_{-3{,}000}$	$600{,}000^{+0}_{-500{,}000}$	$73{,}800^{+300}_{-300}$	$263{,}700^{+1{,}300}_{-1{,}300}$	$184{,}000^{+2{,}000}_{-8{,}000}$	$480{,}000^{+1{,}000}_{-4{,}000}$
Ring obliquity (θ), °	$0.969^{+0.003}_{-0.006}$	$0.56^{+0.14}_{-0.00}$	$1.536^{+0.017}_{-0.007}$	$1.587^{+0.010}_{-0.011}$	$3.8^{+0.1}_{-0.6}$	$4.6^{+0.4}_{-0.9}$
Ring azimuthal angle (ϕ), °	$56.45^{+0.21}_{-0.27}$	118^{+9}_{-0}	$118.06^{+0.11}_{-0.11}$	$150.1^{+0.5}_{-0.5}$	$112.8^{+1.1}_{-1.0}$	$57.0^{+0.4}_{-0.3}$

Estimated parameter name	Main model (Full data)	Fold 0 (Ingress)	Fold 1 (Pre-Mid)	Fold 2 (Midtransit)	Fold 3 (Post-mid)	Fold 4 (Egress)
Exoplanet orbit eccentricity (e_p)	0.003	$0.014^{+0.000}_{-0.005}$	0	0.002	0	0.003
Exoplanet orbit inclination (i), °	$84.58^{+0.15}_{-0.33}$	60^{+0}_{-20}	$72.106^{+0.014}_{-0.019}$	$77.32^{+0.02}_{-0.03}$	$88.2^{+0.1}_{-0.4}$	$86.61^{+0.05}_{-0.13}$
Ring argument of periapsis (ψ), °	$42.8^{+1.3}_{-1.4}$	120^{+0}_{-70}	$73.90^{+0.10}_{-0.11}$	$134.8^{+1.0}_{-1.2}$	$161.1^{+0.1}_{-0.7}$	$133.6^{+1.7}_{-0.5}$

4.4.6. Theoretical boundaries of the ring search

Another notable limitation of the current modeling framework is that the search window for ring systems is strictly constrained to the Roche limit concerning the semi-major axis of the rings. While it narrows the prior distribution, which is important for more effective data fitting, and targets the algorithm on the most stable and common ring configurations, it neglects potential rings that may exist at greater distances. To broaden the possible range of values of the ring's semi-major axis, it would be necessary to incorporate a more complex approach to modeling ring dynamics. Specifically, the model must incorporate the **Hill radius** (Heising et al., 2015) - the region where the planet's gravity dominates over the star's tidal pull - and the orientation of the **Laplace plane** (Heising et al., 2015), which affects the precession and stability of the rings. Without these considerations, extending the search boundary could lead to physically irrelevant ring configurations.

5. Conclusions

In this study, we have described the development, validation and application of a novel model for detecting exoplanetary rings and obtaining their properties through data fitting of transit photometry measurements. Our new pixel-based method allows addressing previous uncertainties and limitations by simulating the exoplanet, its rings and the host star as pixel-gridded matrices, providing a physically accurate characterization of the transit event. Also, the proposed model aims to integrate the parameters that are often overlooked by other studies, such as ring transparency, ring eccentricity and the full 3D orientation of the exoplanet orbit and its ring.

The validity of our model was then tested through the generation of synthetic light curves, which helped systematically explore the effect of each parameter on the light curve. Finally, the model was implemented in practice by analyzing the photometric data for HIP 41378f, which is a super-puff candidate and a high-priority target for searches of exoplanetary

rings. Our data-fitting results show that the best-fit light curve that is produced by our model, which accounts for the exoplanet's rings, fits the observed data with higher precision compared to four alternative models (spherical ringless planet, oblate planet, observational noise and stellar activity). The reliability of the model was also confirmed via a posterior predicted check, k-fold cross-validation and analysis of parameter correlations.

Additionally, the nested sampling analysis has provided the first quantitative measurements of the parameters of the HIP 41378f's hypothetical rings. Best-fit parameters suggest a large ($a = 0.018$ AU), eccentric ($e = 0.418$) and tenuous ($\tau = 0.006$) ring, lying in an almost edge-on orientation, with parameter correlation analysis suggesting only several possible degeneracies: exoplanetary orbit eccentricity vs. exoplanet's argument of periapsis, orbital inclination vs. exoplanet's argument of periapsis, ring eccentricity vs. its semi-major axis, and ring obliquity vs. azimuthal angle. This serves as a potential sign of a ring system around HIP 41378f, yielding a planet bulk density estimate of $173.7\ \mathrm{kg\ m^{-3}}$, suggesting that inflated radii of super-puff exoplanets might be observational artifacts resulting from unseen rings. The results also demonstrate the importance of obtaining higher-precision data for a full characterization. This generally supports our hypothesis that it is possible to extract ring properties from a light curve by fitting modeled light curves to observations.

Thus, in the future, our model can become a valuable tool for discovering and confirming new exoplanetary ring systems, estimating their parameters, and re-evaluating "super-puffs". For any in-depth analysis of an exoplanetary ring system, obtaining its general properties is essential, which can now be done by implementing our tool.

As it is evident, even though the model is precise and takes into account many parameters the effect of which on the transit light curve is minor, our model can be improved by running a nested sampling simulation with more live points and handling ring **precession** (Heising et al., 2015), **light scattering** by rings (Barnes & Fortney, 2004), Laplace plane (Heising et al., 2015) and **effects of exomoons** on ring stability. For decreasing the possible degeneracies and reducing computational intensity, it is favorable to decrease the number of model parameters, switching from the full 3D exoplanetary orbit orientation to impact parameter and potentially favoring circular rings for avoiding the degeneracy between a and e. Other prospects that this work introduces for the nearest future include: injection-recovery analysis for quantifying detection efficiency and sensitivity limits, specifically by injecting synthetic ringed exoplanet transits of various optical depths and geometries into HIP 41378f residual observational data, determining the minimum signal-to-noise ratio required to distinguish between super-puff planets and ring candidates; analyzing more real light curves and detecting more ring systems; exploring irregular ring systems, where the rings exist outside the Roche radius; studying HIP 41378f further, approving the existence of its rings and examining if its inflated radius can be caused by any other effect. Another important prospect is integrating the tool with other software, for instance, TLS, for easier and more frequent analysis of exoplanetary ring systems.

6. GitHub

The link to the project repository can be found through the GitHub link:

https://anonymous.4open.science/r/RingedExoplanetTransits-4F93/README.md.

7. References

Aizawa (逢澤正嵩), M., Uehara (上原翔), S., Masuda (増田賢人), K., Kawahara (河原創), H., & Suto (須藤靖), Y. (2017). Toward Detection of Exoplanetary Rings via Transit Photometry: Methodology and a Possible Candidate. The Astronomical Journal, 153(4), 193. https://doi.org/10.3847/1538-3881/aa6336

Barnes, J. W., & Fortney, J. J. (2004). Transit Detectability of Ring Systems around Extrasolar Giant Planets. The Astrophysical Journal, 616(2), 1193. https://doi.org/10.1086/425067

Barnes, J. W. (2009). Transit Lightcurves of Extrasolar Planets Orbiting Rapidly Rotating Stars. The Astrophysical Journal, 705, 683–692. https://doi.org/10.1088/0004-637X/705/1/683

Berardo, D., Crossfield, I. J. M., Werner, M., Petigura, E., Christiansen, J., Ciardi, D. R., Dressing, C., Fulton, B. J., Gorjian, V., Greene, T. P., Hardegree-Ullman, K., Kane, S. R., Livingston, J., Morales, F., & Schlieder, J. E. (2019). Revisiting the HIP 41378 System with K2 and Spitzer. The Astronomical Journal, 157, 185. https://doi.org/10.3847/1538-3881/ab100c

Boudet, N., Mutschke, H., Nayral, C., Jäger, C., Bernard, J.-P., Henning, T., & Meny, C. (2005). Temperature Dependence of the Submillimeter Absorption Coefficient of Amorphous Silicate Grains. The Astrophysical Journal, 633(1), 272. https://doi.org/10.1086/432966

Caldwell, D. A., Van Cleve, J. E., Jenkins, J. M., Argabright, V. S., Kolodziejczak, J. J., Dunham, E. W., Geary, J. C., Tenenbaum, P., Chandrasekaran, H., Li, J., Wu, H., & Von Wilpert, J. (2010). Kepler instrument performance: An in-flight update (J. M. Oschmann, Jr., M. C. Clampin, & H. A. MacEwen, Eds.; p. 773117). https://doi.org/10.1117/12.856638

Chandrasekhar, S. (1969). Ellipsoidal figures of equilibrium. In The Silliman Foundation Lectures. https://ui.adsabs.harvard.edu/abs/1969efe..book.....C

Claret, A., & Giménez, A. (1990). Limb-darkening coefficients of late-type stars. Astronomy and Astrophysics, 230, 412–418.

Costa, G. (2019). Evolution of rotating stars with PARSEC: implementation and comparison with observations. International School for Advanced Studies. https://www.sissa.it/ap/phdsection/AlumniThesis/Guglielmo%20Costa.pdf

Cuzzi, J. N., Filacchione, G., & Marouf, E. A. (2018). The Rings of Saturn. In M. S. Tiscareno & C. D. Murray (Eds.), Planetary Ring Systems (Section 3.6; 1st ed., pp. 51–92). Cambridge University Press. https://doi.org/10.1017/9781316286791.003

Díaz-Cordoves, J., & Giménez, A. (1992). A new nonlinear approximation to the limb-darkening of hot stars. Astronomy and Astrophysics, 259, 227–231.

Dholakia, S., Luger, R., & Dholakia, S. (2022). Efficient and Precise Transit Light Curves for Rapidly Rotating, Oblate Stars. The Astrophysical Journal, 925(2), 185. https://doi.org/10.3847/1538-4357/ac33aa

Donchev, V. D., Mladenova, C. D., & Mladenov, I. M. (2015). On the compositions of rotations. 080004. https://doi.org/10.1063/1.4934315

Espinoza, N., & Jordán, A. (2016). Limb darkening and exoplanets—II. Choosing the best law for optimal retrieval of transit parameters. Monthly Notices of the Royal Astronomical Society, 457, 3573–3581. https://doi.org/10.1093/mnras/stw224

Euler, L. (1776). General formulas for the translation of arbitrary rigid bodies. 1776. https://scholarlycommons.pacific.edu/euler-works/478/

Feroz, F., Hobson, M. P., & Bridges, M. (2009). MULTINEST: An efficient and robust Bayesian inference tool for cosmology and particle physics. Monthly Notices of the Royal Astronomical Society, 398, 1601–1614. https://doi.org/10.1111/j.1365-2966.2009.14548.x

Foreman-Mackey, D., Hogg, D. W., Lang, D., & Goodman, J. (2013). emcee: The MCMC Hammer. Publications of the Astronomical Society of the Pacific, 125(925), 306–312. https://doi.org/10.1086/670067

Gaia Collaboration, Vallenari, A., Brown, A. G. A., Prusti, T., Bruijne, J. H. J. de, Arenou, F., Babusiaux, C., Biermann, M., Creevey, O. L., Ducourant, C., Evans, D. W., Eyer, L., Guerra, R., Hutton, A., Jordi, C., Klioner, S. A., Lammers, U. L., Lindegren, L., Luri, X., … Zwitter, T. (2023). Gaia Data Release 3: Summary of the content and survey properties. Astronomy & Astrophysics, 674, A1. https://doi.org/10.1051/0004-6361/202243940

Gilks, W. R., Richardson, S., & Spiegelhalter, D. (1995). Markov Chain Monte Carlo in Practice. CRC Press.

Goldreich, P., & Tremaine, S. (1978). The formation of the Cassini division in Saturn's rings. Icarus, 34(2), 240–253. https://doi.org/10.1016/0019-1035(78)90165-3

Grant, D., & Wakeford, H. R. (2024). ExoTiC-LD: Thirty seconds to stellar limb-darkening coefficients. Journal of Open Source Software, 9(100), 6816. https://doi.org/10.21105/joss.06816

Grouffal, S., Santerne, A., Bourrier, V., Dumusque, X., Triaud, A. H. M. J., Malavolta, L., Kunovac, V., Armstrong, D. J., Attia, M., Barros, S. C. C., Boisse, I., Deleuil, M., Demangeon, O. D. S., Dressing, C. D., Figueira, P., Lillo-Box, J., Mortier, A., Nardiello, D., Santos, N. C., & Sousa, S. G. (2022). Rossiter-McLaughlin detection of the 9-month period transiting exoplanet HIP41378 d. Astronomy & Astrophysics, 668, A172. https://doi.org/10.1051/0004-6361/202244182

Grouffal, S., Santerne, A., Bourrier, V., Kunovac, V., Dressing, C., Akinsanmi, B., Armstrong, C., Baliwal, S., Balsalobre-Ruza, O., Barros, S. C. C., Bayliss, D., Crossfield, I. J. M., Demangeon, O., Dumusque, X., Giacalone, S., Harada, C. K., Isaacson, H., Kellermann, H., Lillo-Box, J., … Wheatley, P. J. (2025). The star HIP 41378 potentially misaligned with its cohort of long-period planets (No. arXiv:2507.01807). arXiv. https://doi.org/10.48550/arXiv.2507.01807

Harris, C. R., Millman, K. J., Van Der Walt, S. J., Gommers, R., Virtanen, P., Cournapeau, D., Wieser, E., Taylor, J., Berg, S., Smith, N. J., Kern, R., Picus, M., Hoyer, S., Van Kerkwijk, M. H., Brett, M., Haldane, A., Del Río, J. F., Wiebe, M., Peterson, P., … Oliphant, T. E. (2020). Array programming with NumPy. Nature, 585(7825), 357–362. https://doi.org/10.1038/s41586-020-2649-2

Hedman, M. M., Burns, J. A., Hamilton, D. P., & Showalter, M. R. (2012). The three-dimensional structure of Saturn's E ring. Icarus, 217(1), 322–338. https://doi.org/10.1016/j.icarus.2011.11.006

Heising, M. Z., Marcy, G. W., & Schlichting, H. E. (2015). A SEARCH FOR RINGED EXOPLANETS USING KEPLER PHOTOMETRY. The Astrophysical Journal, 814(1), 81. https://doi.org/10.1088/0004-637x/814/1/81

Higson, E., Handley, W., Hobson, M., & Lasenby, A. (2019). Dynamic nested sampling: An improved algorithm for parameter

estimation and evidence calculation. Statistics and Computing, 29(5), 891–913. https://doi.org/10.1007/s11222-018-9844-0

Hippke, M., & Heller, R. (2019). Transit Least Squares: Optimized transit detection algorithm to search for periodic transits of small planets. Astronomy & Astrophysics, 623, A39. https://doi.org/10.1051/0004-6361/201834672

Hunter, J. D. (2007). Matplotlib: A 2D Graphics Environment. Computing in Science & Engineering, 9(3), 90–95. https://doi.org/10.1109/MCSE.2007.55

Ichtiaroglou, S., & Voyatzis, G. (1990). On the effect of the eccentricity of a planetary orbit on the stability of satellite orbits. Journal of Astrophysics and Astronomy, 11(1), 11–22. https://doi.org/10.1007/BF02728017

Johnson, H. L., & Morgan, W. W. (1953). Fundamental stellar photometry for standards of spectral type on the revised system of the Yerkes spectral atlas. The Astrophysical Journal, 117, 313. https://doi.org/10.1086/145697

Jones, H. R. A., Butler, R. P., Tinney, C. G., Marcy, G. W., Carter, B. D., Penny, A. J., McCarthy, C., & Bailey, J. (2006). High-eccentricity planets from the Anglo-Australian Planet Search. Monthly Notices of the Royal Astronomical Society, 369(1), 249–256. https://doi.org/10.1111/j.1365-2966.2006.10298.x

Juhász, A., & Horányi, M. (2002). Saturn's E ring: A dynamical approach. Journal of Geophysical Research: Space Physics, 107(A6). https://doi.org/10.1029/2001JA000182

Kenworthy, M. A., & Mamajek, E. E. (2015). MODELING GIANT EXTRASOLAR RING SYSTEMS IN ECLIPSE AND THE CASE OF J1407B: SCULPTING BY EXOMOONS? The Astrophysical Journal, 800(2), 126. https://doi.org/10.1088/0004-637X/800/2/126

Koposov, S., Speagle, J., Barbary, K., Ashton, G., Buchner, J., Scheffler, C., Talbot, C., Cook, B., Guillochon, J., Cubillos, P., Ramos, A. A., Dartiailh, M., Ilya, Tollerud, E., Lang, D., Johnson, B., jtmendel, Higson, E., Vandal, T., … joezuntz. (2025). joshspeagle/dynesty: V3.0.0 (Version v3.0.0) [Computer software]. Zenodo. https://doi.org/10.5281/ZENODO.3348367

Libby-Roberts, J. E., Berta-Thompson, Z. K., Désert, J.-M., Masuda, K., Morley, C. V., Lopez, E. D., Deck, K. M., Fabrycky, D., Fortney, J. J., Line, M. R., Sanchis-Ojeda, R., & Winn, J. N. (2020). The Featureless Transmission Spectra of Two Super-puff Planets. The Astronomical Journal, 159(2), 57. https://doi.org/10.3847/1538-3881/ab5d36

Lu, T., Li, G., Cassese, B., & Lin, D. N. C. (2025). The Dynamical History of HIP-41378 f—Oblique Exorings Masquerading as a Puffy Planet. The Astrophysical Journal, 980(1), 39. https://doi.org/10.3847/1538-4357/ada4b2

Mayor, M., Lovis, C., & Santos, N. C. (2014). Doppler spectroscopy as a path to the detection of Earth-like planets. Nature, 513(7518), 328–335. https://doi.org/10.1038/nature13780

Miller, K. E., Filacchione, G., Cuzzi, J. N., Nicholson, P. D., Hedman, M. M., Baillié, K., Johnson, R. E., Tseng, W.-L., Estrada, P. R., Waite, J. H., Ciarniello, M., Ferrari, C., Zhang, Z., Hendrix, A., Moses, J. I., & Hsu, H.-W. (2024). The Composition of Saturn's Rings. Space Science Reviews, 220(6), 70. https://doi.org/10.1007/s11214-024-01104-y

Morgado, B. E., Sicardy, B., Braga-Ribas, F., Ortiz, J. L., Salo, H., Vachier, F., Desmars, J., Pereira, C. L., Santos-Sanz, P., Sfair, R., de Santana, T., Assafin, M., Vieira-Martins, R., Gomes-Júnior, A. R., Margoti, G., Dhillon, V. S., Fernández-Valenzuela, E.,

Broughton, J., Bradshaw, J., … de Wit, J. (2023). A dense ring of the trans-Neptunian object Quaoar outside its Roche limit. Nature, 614(7947), 239–243. https://doi.org/10.1038/s41586-022-05629-6

Murray, C. D., & Dermott, S. F. (2012). Solar system dynamics. Cambridge Univ. Press. https://doi.org/10.1017/CBO9781139174817

Ohta, Y., Taruya, A., & Suto, Y. (2009). PREDICTING PHOTOMETRIC AND SPECTROSCOPIC SIGNATURES OF RINGS AROUND TRANSITING EXTRASOLAR PLANETS. The Astrophysical Journal, 690(1), 1–12. https://doi.org/10.1088/0004-637x/690/1/1

Piro, A. L., & Vissapragada, S. (2020). Exploring Whether Super-puffs can be Explained as Ringed Exoplanets. The Astronomical Journal, 159(4), 131. https://doi.org/10.3847/1538-3881/ab7192

Porco, C. C., Thomas, P. C., Weiss, J. W., & Richardson, D. C. (2007). Saturn's Small Inner Satellites: Clues to Their Origins. Science, 318(5856), 1602–1607. https://doi.org/10.1126/science.1143977

Quanz, S. P., Amara, A., Meyer, M. R., Girard, J. H., Kenworthy, M. A., & Kasper, M. (2015). CONFIRMATION AND CHARACTERIZATION OF THE PROTOPLANET HD 100546 b—DIRECT EVIDENCE FOR GAS GIANT PLANET FORMATION AT 50 AU. The Astrophysical Journal, 807(1), 64. https://doi.org/10.1088/0004-637X/807/1/64

Santerne, A., Malavolta, L., Kosiarek, M. R., Dai, F., Dressing, C. D., Dumusque, X., Hara, N. C., Lopez, T. A., Mortier, A., Vanderburg, A., Adibekyan, V., Armstrong, D. J., Barrado, D., Barros, S. C. C., Bayliss, D., Berardo, D., Boisse, I., Bonomo, A. S., Bouchy, F., … Winn, J. N. (2019). An extremely low-density and temperate giant exoplanet (No. arXiv:1911.07355). arXiv. https://doi.org/10.48550/arXiv.1911.07355

Savic, R. M., & Karlsson, M. O. (2009). Importance of Shrinkage in Empirical Bayes Estimates for Diagnostics: Problems and Solutions. The AAPS Journal, 11(3), 558–569. https://doi.org/10.1208/s12248-009-9133-0

Schlichting, H. E., & Chang, P. (2011). WARM SATURNS: ON THE NATURE OF RINGS AROUND EXTRASOLAR PLANETS THAT RESIDE INSIDE THE ICE LINE. The Astrophysical Journal, 734(2), 117. https://doi.org/10.1088/0004-637X/734/2/117

Skilling, J. (2004). Nested Sampling. 735, 395–405. https://doi.org/10.1063/1.1835238

Skilling, J. (2006). Nested sampling for general Bayesian computation. Bayesian Analysis, 1(4). https://doi.org/10.1214/06-BA127

Speagle, J. S. (2020). DYNESTY: A dynamic nested sampling package for estimating Bayesian posteriors and evidences. Monthly Notices of the Royal Astronomical Society, 493(3), 3132–3158. https://doi.org/10.1093/mnras/staa278

Strömgren, B. (1956). Two-dimensional spectral classification of F stars through photoelectric photometry with interference filters. Vistas in Astronomy, 2, 1336–1346. https://doi.org/10.1016/0083-6656(56)90060-5

Tajeddine, R., Nicholson, P. D., Longaretti, P.-Y., Moutamid, M. E., & Burns, J. A. (2017). What Confines the Rings of Saturn? The Astrophysical Journal Supplement Series, 232(2), 28. https://doi.org/10.3847/1538-4365/aa8c09

Team, J. E. (2020). Exoplanet Photometry and False Positives. https://pressbooks.howardcc.edu/jrip3/chapter/exoplanet-photometry-and-false-positives/

Tiscareno, M. S. (2013). Planetary Rings (pp. 309–375). https://doi.org/10.1007/978-94-007-5606-9_7

Tiscareno, M. S., Hedman, M. M., Burns, J. A., & Castillo-Rogez, J. (2013). COMPOSITIONS AND ORIGINS OF OUTER PLANET SYSTEMS: INSIGHTS FROM THE ROCHE CRITICAL DENSITY. The Astrophysical Journal Letters, 765(2), L28. https://doi.org/10.1088/2041-8205/765/2/L28

Tiscareno, M. S., & Murray, C. D. (2018). Planetary Ring Systems: Properties, Structure, and Evolution (Section 5). Cambridge University Press. https://books.google.com/books?hl=en&lr=&id=1i1RDwAAQBAJ&oi=fnd&pg=PA112&dq=neptune+le+verrier+ring&ots=-axyjzN6mL&sig=gXYjLrEYFc_Ts8edzeSvvLdGhfk#v=onepage&q=neptune%20le%20verrier%20ring&f=false

Utry, N., Ajtai, T., Pintér, M., Tombácz, E., Illés, E., Bozóki, Z., & Szabó, G. (2014). Mass specific optical absorption coefficients of mineral dust components measured by a multi wavelength photoacoustic spectrometer. Aerosols/Laboratory Measurement/Data Processing and Information Retrieval. https://doi.org/10.5194/amtd-7-9025-2014

Vanderburg, A., Becker, J. C., Kristiansen, M. H., Bieryla, A., Duev, D. A., Jensen-Clem, R., Morton, T. D., Latham, D. W., Adams, F. C., Baranec, C., Berlind, P., Calkins, M. L., Esquerdo, G. A., Kulkarni, S., Law, N. M., Riddle, R., Salama, M., & Schmitt, A. R. (2016). Five Planets Transiting a Ninth Magnitude Star. The Astrophysical Journal, 827, L10. https://doi.org/10.3847/2041-8205/827/1/L10

Vera, M., Flórez, M., Salazar-Torres, J., Huérfano, Y., Gelvez-Almeida, E., Valbuena, O., Vera, M. I., & Aranguen, M. (2019). Newton-Raphson method initialization for non-analytical equations solution linked to anticipated annuities. Journal of Physics: Conference Series, 1414(1), 012012. https://doi.org/10.1088/1742-6596/1414/1/012012

Virtanen, P., Gommers, R., Oliphant, T. E., Haberland, M., Reddy, T., Cournapeau, D., Burovski, E., Peterson, P., Weckesser, W., Bright, J., Van Der Walt, S. J., Brett, M., Wilson, J., Millman, K. J., Mayorov, N., Nelson, A. R. J., Jones, E., Kern, R., Larson, E., … Vázquez-Baeza, Y. (2020). SciPy 1.0: Fundamental algorithms for scientific computing in Python. Nature Methods, 17(3), 261–272. https://doi.org/10.1038/s41592-019-0686-2

von Zeipel, H. (1924). The radiative equilibrium of a rotating system of gaseous masses. Monthly Notices of the Royal Astronomical Society, 84, 665–683. https://doi.org/10.1093/mnras/84.9.665

Watson, C. L., Henden, A. A., & Price, A. (2006). The International Variable Star Index (VSX). Society for Astronomical Sciences Annual Symposium, 25, 47.

Weisstein, E. W. (n.d.). Rotation Matrix [Text]. Wolfram Research, Inc. Retrieved August 7, 2025, from https://mathworld.wolfram.com/RotationMatrix.html

Acknowledgements

We thank our teachers and research mentors Dr. Chima McGruder, Catherine Petretti and Artemii Vakhonin for constant

support, insightful discussions and valuable feedback on the paper. We also sincerely appreciate the time and expertise of the anonymous reviewers and the editorial team of the Convergence Journal. Their critical feedback and invaluable recommendations greatly enhanced the rigor and quality of this paper. Furthermore, we thank Indigo Research for providing talented students all around the world the opportunity to transform the future through research.

This paper includes data collected by the Kepler mission and obtained from the MAST data archive at the Space Telescope Science Institute (STScI). Funding for the Kepler mission is provided by the NASA Science Mission Directorate. STScI is operated by the Association of Universities for Research in Astronomy, Inc., under NASA contract NAS 5–26555.

Author Biography

Daniil Veliev is a 16-year-old high school student from Russia who is studying in the International Program at Letovo School. Since early childhood, he has been fascinated by astronomy and astrophysics. He is inspired by space research that can practically contribute to science and influence our understanding of the universe.

Recently, he became interested in researching the possibility of detecting and studying rings around exoplanets and minor bodies in the Solar System. And he is happy to have successfully created a specific tool that may help identify more ringed planet candidates, which can help us build the foundation for future research.

In addition to exoplanetary science and the study of minor planets, Daniil is involved in the research of variable stars, models of galaxy evolution, and the implementation of standard candles for measuring distances.

Daniil sincerely believes that education should be accessible for everyone, as the greatest discoveries are always born at the intersection of different cultures and experiences, so he takes part in free educational projects, being a course coordinator and a teacher, helping middle school students on their path to explore the universe.

Mentor Contribution Statements

Catherine Petretti is a teaching assistant for the IRIS Summer Astrophysics program and a Ph.D. candidate at Harvard University. She was the teaching assistant during the course in which Daniel Veliev completed the research presented in his paper "*Exoplanetary Ring Systems: Identification and Parameter Estimation from Transit Photometry Data*." Daniel is an exceptionally bright student, and Catherine can attest that, to the best of her knowledge, all of the work that Daniel presented in his paper is his own.

During the course, the main individual interactions Catherine had with him were during office hours or over email, in which he would ask questions about his research. Occasionally, these questions were about technical problems he was facing, such as how to derive the equations used for his parameter calculations or how to implement MCMC into his work. In these cases, Catherine would do her best to direct him toward a solution and provide guidance for analysis when necessary, without contributing any work of her own. More commonly, his questions concerned the structure of his paper, such as what details about his analysis to include.

Catherine's primary contribution to his work was editorial—she read through and edited his paper in detail three to four

times prior to submission. However, she did not contribute any results or analysis of her own. According to Catherine, Daniel is an extremely independent and intelligent student with a bright future ahead of him as a researcher, and she hopes this statement clarifies the extent of his work.

Dr. Chima McGruder is a Harvard Astrophysics Ph.D., an IRIS research professor, and a data modeling specialist at the University of Arizona. He taught the six-week IRIS Astrophysics research course in which Daniel Veliev was one of his students.

As part of the course, Dr. McGruder delivered lectures on how to conduct an astrophysics research project from start to finish, including foundational astrophysics concepts, methods for sourcing and analyzing peer-reviewed literature, and approaches to structuring and refining a research paper. As Daniel progressed in his project, Dr. McGruder met with him individually for a limited number of hours to provide guidance on improving the topic, structure, content, and analytical methods of his work.

Daniel entered the course with an already well-developed software package for modeling asteroid transits. During an individual session, Dr. McGruder advised him to adapt this code for the purposes of the paper and provided direction on how to do so. Throughout the analysis phase, he also shared relevant research papers and computational tools that could assist with software development. At the final stage, he provided a detailed critique of the completed manuscript, including comments and suggestions for improvement.

Beyond this relatively hands-off advising, Daniel's paper is a product of his own independent study and intellectual effort, and Dr. McGruder supports its publication as independent and original scholarly work.

In addition, Dr. McGruder's academic expertise in astrophysics and exoplanet research was invaluable to Daniel's project. His personal attention and prompt, detailed feedback were instrumental in developing a complex model and refining the paper. He advised Daniel at each stage on emerging challenges and recommended appropriate methods and software, ultimately serving as a true mentor throughout the research process.

Artemii Vakhonin is a programmer at the Caucasus Mountain Observatory, Sternberg Astronomical Institute (SAI MSU), and served as Daniel Veliev's scientific advisor on an earlier research project.

During that project, Daniel developed software to model stellar occultations by asteroids with ring systems. The software generated theoretical light curves and included a graphical interface for comparison with observational data. Artemii's role involved advising on the principles of modeling and the general physics of the phenomena, while all code development was carried out entirely by Daniel. Throughout the work, Daniel independently proposed new ideas and potential improvements, and he also conducted comparisons with existing light curves for ringed asteroids independently.

Building on this foundation, Daniel later pursued the present research project independently. Artemii continued to provide general advice on statistics and physics when needed. However, the implementation of the project in code, the numerical calculations, and the writing of the article were carried out entirely by Daniel.

This statement reflects that Artemii's role was advisory in nature, while the research, execution, and authorship of the work

were Daniel's own.